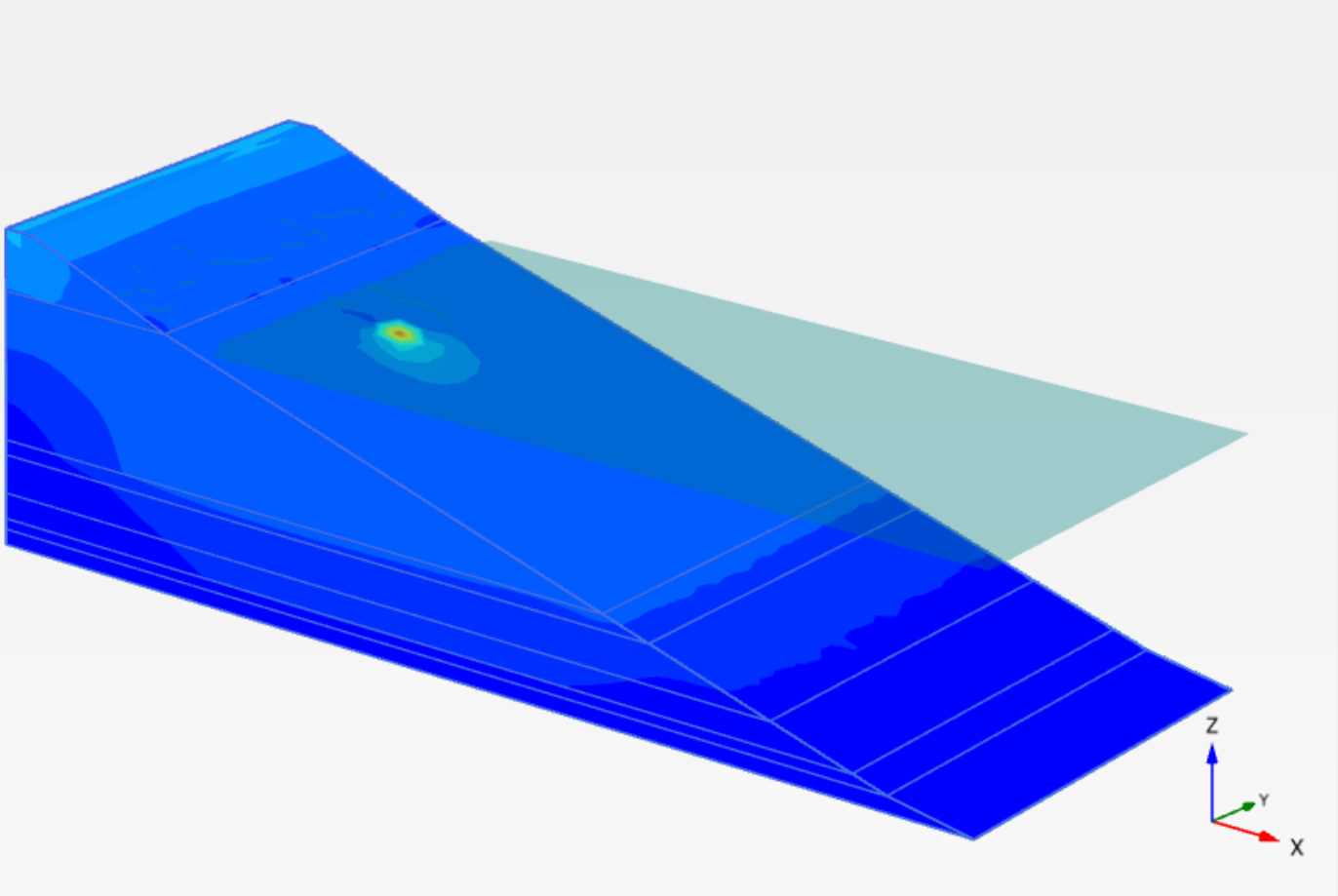

Determination of factor of safety of a slope subjected to vibratory pile driving in 3D

Avinab Mohanty

TU Delft

Determination of factor of safety of a slope subjected to vibratory pile driving in 3D

by

Avinab Mohanty

Student number:	4802535	
Presented on:	30th March 2022	
Thesis committee:	Dr.ir Cor Zwanenburg,	TU Delft, supervisor
	Ir.(drs)R.E.P. (Richard) de Nijs,	TU Delft
	Dr.Apostolos Tsouvalas,	TU Delft

TU Delft

Preface

”The purpose of life is to contribute in some way to making things better”
- Robert F. Kennedy

Avinab Mohanty
Delft, March 2022

Abstract

Vibratory installation of piles and casings can be extremely economical, therefore the contractors prefer pile driving. When compared to impact pile driving, vibratory pile driving generates less noise but this installation method is still fraught with uncertainties (Rausche 2003). Environmental effects (such as ground vibrations) have negative impacts which could lead to damage and failure under special circumstances.
The vibrations from the pile driving generate excess pore pressures and cause settles leading to failure in slopes. As part of the optimisation of mooring places for inland shipping and small coasters in Calandkanaal, the port of Rotterdam authority had a number of mooring places modified in the second half of 2016. A point of attention was the lack of analysis and a testing framework as there were uncertainties in excess pore pressure generation, an exposed area in the slope and the slope stability. Based on these uncertainties, the work presented in this report tries to bridge this gap by answering the following research question:

How can the existing knowledge on pile driving by means of vibratory installation be efficiently integrated into a 3D model which can practically estimate the factor of safety of the slope during vibratory installations ?

To answer the main research question, a few sub questions were formed, which are as follows:

- *How can the vibratory parameters be integrated to model the slope stability?*
- *What is the thickness of highly degraded zone around the pile due to vibratory pile driving?*
- *What are the limitations of the study?*

The proposed work uses the vibratory pile driving data to generate excess pore pressure data using an empirical pore pressure model given by Green & Mitchell (2004) referred here as the GMP pore pressure model. Along with the pore pressures by using an empirical attenuation relation, the extent of the liquefied zone was determined giving an idea about the area of the slope affected by pile driving.

For slope stability PLAXIS 3D is used along with its flow module. PLAXIS 3D gives an idea of the expected displacements in the geometry (slope) and the factor of safety. In a way to incorporate vibration effects, only the pore pressure are used as load inputs because of the difficulty of inducing pile driving vibrations in a static calculation.

To add pore pressures in to the geometry, a well was used with the infiltration function for the amount of time the pile was driven in the actual project. The volume input for the well infiltration is calculated in the same way as it was done in the actual project shown in the work of de Nijs (2019). PLAXIS 2D and D-geo stability software packages are also used in an attempt to make comparisons with the PLAXIS 3D model and validate the whole analysis.

Contents

List of Figures

List of Tables

1

Proposal

Vibratory installation of piles and casings can be extremely economical, therefore the contractors prefer pile driving. When compared to impact pile driving, vibratory pile driving generates less noise but this installation method is still fraught with uncertainties (Rausche 2003). Environmental effects (such as ground vibrations) have negative impacts which could lead to damage and failure under special circumstances.

1.1. Problem Statement:

In vibratory pile driving, vibratory hammer is a commonly used equipment. The vibrations from the pile driving generate excess pore water and can cause settlements which can lead to failure in slopes.

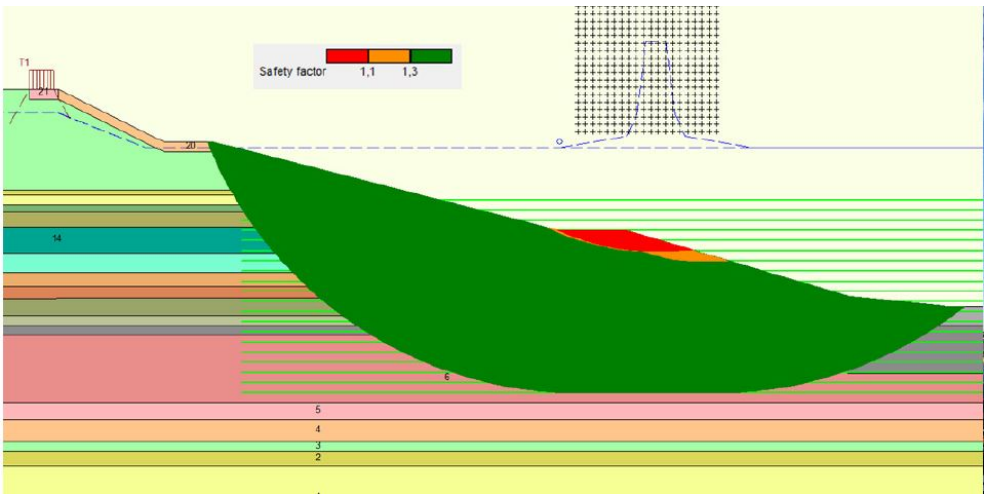

Figure 1.1: Uncertainty in slope stability of the Embankment (de Nijs 2019)

In the vicinity of the embankments during installation of piles in granular soils, there is an uncertainty on slope stability as seen in figure 1.1, since there has been no proper way of anticipating excess pore water generations and vibrations. Even the exposed area in the embankment is uncertain. Due to unavailability of an evaluation method, more empirical methods are used, which most of time are lengthy and also less reliable.

1.2. Aim and Objective

The objective of this research is to come up with an approach to analyse the impacts of ground vibrations on the slope stability, based on the integration of existing knowledge and validation on actual field data.

This proposal first focuses on the literature study to better conceive the available knowledge on physical process of vibrations and the consequences of the vibrations on the embankment. Further, existing models to predict its magnitude and the extent of influence are reviewed. The second part of the literature aims to understand the available evaluation methods for the factor of safety of the slope stability and also the nature of the available field data.

1.3. Extent and Limitation

The study is focused on the slope stability after the installation of circular piles in the dike. Probable causes of failure on the slope due to pile driving is not included in the study. After attaining satisfactory results from the numerical integration of required models, attempts will be made to adapt the model for actual parameters from the Rotterdam port project (de Nijs 2019).

1.4. Research Question

The research question indicated below will act as foundation for this work and also for the report. There are several research works available that focuses on the settlement incurred due to the vibration activity and evaluation of factor of safety for dikes and embankments. However, very little has been done to get an integrated model for vibrations and evaluations of factor of safety. To cover this shortage, the research question is as follows:

1. *How can the existing knowledge on pile driving by means of vibratory installation be efficiently integrated into a 3D model which can practically estimate the factor of safety of the slope during vibratory installations ?*

1.5. Research Approach and Strategy

The initial goal of the thesis will be to understand the vibration data collected from the Calandkanaal, Port of Rotterdam and generate excess pore pressures data alternatively. Furthermore, this computed excess pore pressure will be used as a reference data for the Plaxis-3D model, determining the factor of safety.

1.6. Methodology

1.6.1. Estimation of energy dissipation and excess pore pressures

The base understanding of the physical processes is attained from the work of Dr.Green in his work on the article (Wales et al. 2000) and Piet Mejers in his Phd thesis ”Settlement during vibratory sheet piling” (Meijers 2007).

1.6.2. Factor of safety of the slope stability

The second part of the research would be to use the computed excess pore pressures as a reference data in the 3D Plaxis modelling to determine the factor of safety of the slope subjected to vibratory pile driving. The only limitation in this part would be the absence of vibratory effects in the model which will be explained briefly in chapter 5.

1.7. Presentation of the Research Results

The aim of the project is to provide an approach to determine the factor of safety of a slope subjected to vibratory pile driving in 3D. The expected output of the project will be understanding the collected data set of the Rotterdam Port project and a 3D Plaxis model which predicts the factor of safety for the slope. The research was carried out in four stages, which will be reflected in the coming chapters. The first stage is the literature review which consists the understanding of the suitable physical processes of vibratory pile driving and its consequences. Later it is followed by understanding the collected data set of the Rotterdam port Project, computing excess pore pressure and then performing a 3D slope stability using finite element modelling.t

The outline of the report is as follows:

1. Introduction

2. Vibratory Installation of Circular Piles
3. Slope Stability Analysis
4. Port of Rotterdam: Data Analysis
5. 3D Finite Element Modelling
6. Discussion
7. Conclusion

2

Vibratory Installation of Circular Piles

The literature review was conducted by sections, first understanding of the actual physical process of vibratory pile (circular) driving was obtained. Later, the process was correlated to the complexities of the soil mechanics with help of Physics and Mathematics.

2.1. Physical Processes occurring during Vibratory pile driving

During the installation of vibratory piles the vibration gets dissipated to the soil surrounding the pile as waves and energy. The oscillation of the particle around the equilibrium state is an typical example of vibratory motion and it is characterized by displacement of particle or body in time due to acceleration. In vibratory piles, the pile is rigidly connected to the vibrator resulting in minimal energy loss while the energy is transferred from vibrator to the pile. Because of relatively low vibration frequency the wavelength propagating down the pile is much longer than in the case of impact driving (Holmberg et al. 1984). This action of wave propagation allows transmission of energy through material, without any material transport.

2.1.1. Mechanism of driving by Vibration

As the name implies, vibratory hammers apply a vibratory force, i.e. an alternating and rapidly repetitive force to drive piles. Vibratory hammers impart energy to the pile-soil system continuously rather than incrementally. Vibrators are inherently bidirectional in their force generation, so either during driving or extraction half of the force is going the wrong way. Yet vibrators can be efficient in both of the above mentioned operations. The key to solving this problem lies in the soil response to the vibrations.
This is generally accomplished by rotating eccentric weights about shafts. Each rotating eccentric weight produces a force acting in a single plane and directed toward the center-line of the shaft.

Figure 2.1 shows the basic setup for the rotating eccentric weights used in most current vibratory pile driving equipment. The weights are set off center of the axis of rotation by the eccentric arm.

As the figure2.1 shows, the weights rotate about the centre shaft with an angular velocity w, given by the equation 2.1.

$$\omega = 2\pi\theta \tag{2.1}$$

- ω= angular velocity of rotation, rad/sec
- θ= frequency of vibrations, Hz= (Eccentric RPM)/60

For a rotating body, the force exerted on the center shaft is given by the equation 2.2.

$$F_{dyn} = mr\omega^2/1000 \tag{2.2}$$

- F_{dyn}= dynamic forces of eccentrics, kN
- m= eccentric mass, kg

- r= eccentric moment arm,m

If the eccentric moment (kg-m) K, is defined as K=m*r, it can be substituted in the above equation 2.2 to form equation 2.3.

$$F_{dyn} = K\omega^2/1000 \tag{2.3}$$

If only one eccentric is used, in one revolution a force will be exerted in all directions giving the system a good deal of whip. To avoid this problem, the eccentrics are paired so the lateral forces cancel each other leaving us with only axial force for the pile.

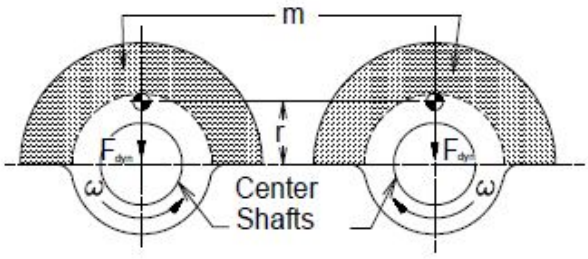

Figure 2.1: Vibratory Eccentric ConfigurationWarrington (1989)

2.2. Waves Generated

From the above it is clear that the propagation of waves in the surrounding soil is of importance for this study. For this study the focus will be on the waves generated by the vibrations of pile driving. Installation of vibratory piles propagates the vibrations in the surrounding soil in the form of the following waves:

- P waves (Primary waves, generated at the toe of the piles)
- S waves (Shear waves, generated at the toe of the piles and along the shaft due to friction)
- R waves (Rayleigh waves)

2.2.1. P-waves

P-waves can lead to the volume change in the medium as they cause compression and rare-fraction. These waves doesn't cause any shearing in the medium that it propagates through. And the oscillation of the particle is parallel to the the direction of the wave propagation. It can propagate both through the solids and fluids (Richart et al. 1970), (L.Kramer 1996).The P-wave involves no shearing or rotation of the material as it passes through. These are the fastest wave present in a solid material. Propagation velocity c_P of p-wave is given by L.Kramer (1996):

$$\sqrt{\frac{M}{\rho}} = \sqrt{\frac{G(2-2\nu)}{\rho(1-2\nu)}} = \sqrt{\frac{E(1-\nu)}{\rho(1-2\nu)(1+\nu)}}(m/s) \tag{2.4}$$

- M = Deformation Modulus or Oedometer modulus
- G = Shear Modulus (Pa)
- E = Elasticity Modulus (Pa)
- ρ = material density (kg/m^3)
- ν = Poisson's ratio(-)

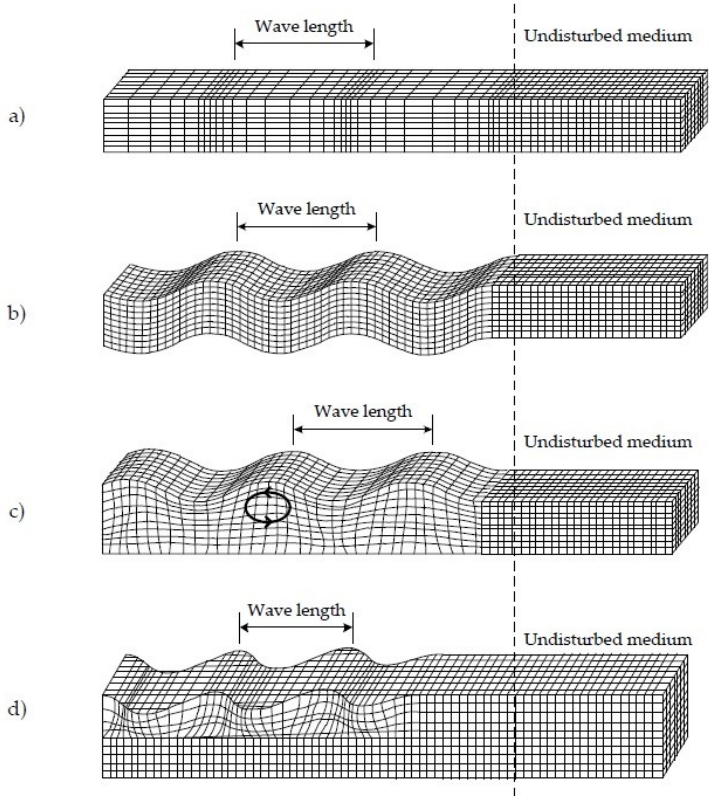

Figure 2.2: Visualization of different waves a) P-wave, b) S-wave, c) R-wave and d) Love-wave, Deckner (2013)

2.2.2. S-waves

The S-waves are transverse waves causing shear deformation in the medium that it propagates. However, it cannot pass through fluids as they don't posses any shearing stiffness. The velocity of the shear wave(c_S) can be computed from L.Kramer (1996).

$$c_S = \sqrt{\frac{G}{\rho}} = \sqrt{\frac{E}{2\rho(1-\nu)}}(m/s) \tag{2.5}$$

- G = Shear Modulus (Pa)
- E = Elasticity Modulus (Pa)
- ρ = material density (kg/m^3)
- ν = Poisson's ratio(-)

The S wave causes oscillation in the particle perpendicular to its propagation. The direction of the oscillation helps to breakdown the S-wave into two components SV(Vertical plane movement) and SH(Horizontal plane movement).

2.2.3. R-waves

The R-waves or Rayleigh waves propagate along the surface of the ground having both horizontal and vertical components of motion. It's a product of interaction of P-wave and S-wave with the surface (L.Kramer 1996).The motion of the wave is in form of retrograde ellipse as represented in 2.2. The depth to which an R-wave causes significant displacement increases with wavelength. The velocity of the R-wave (c_R) can be given by: Holmberg et al. (1984) and Viking & Bodare (1999).

$$c_R \approx \frac{c_s(0.87 + 1.12\nu)}{1+\nu} \tag{2.6}$$

Where

- c_S = Shear wave velocity(m/s)
- ν = Poisson's ratio(-)

The propagation velocity of the R -wave are independent of the vibration frequency that make it non dispersible in the homogeneous half-space. Massarsch, K Rainer; Fellenius (2010) described critical distance as the extent at which P-waves reaches the surface of the ground from the toe of the pile(point of origin). It is represented as

$$\theta_{Critical} = arcsin(\frac{c_S}{c_P}) \tag{2.7}$$

Where

- c_S = S - wave velocity (m/s)
- c_P = P - wave velocity (m/s)

The critical distance $r_{critical}$ from the pile, where refraction will occur on the ground surface:

$$r_{critical} = \tan\theta_{critical} d \tag{2.8}$$

Where d = Pile Penetration depth.

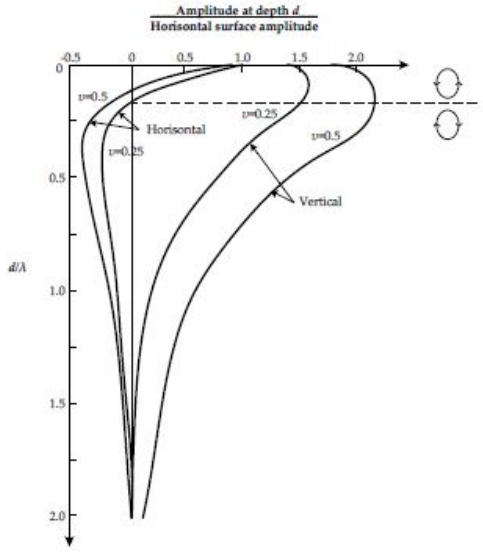

Figure 2.3: Horizontal and vertical vibration amplitude of the Rayleigh wave as a function of depth, Poisson's ratio and wavelength modified after Richart et al.(1970)Deckner (2013)

From the figure 2.3 it is noticed that the vertical amplitude is greater than the horizontal amplitude and also that the vertical amplitude decreases rapidly with depth.

2.3. Cyclic Loading

The vibration due to installation of circular piles, interacts with the soil along the interface of pile leading to energy transmission in form of waves (2.2). The relevant waves act upon the soil media and causes cyclic loading. And the cyclic loading may lead to the densification and settlement in sandy soil. The three major aspect to be considered while installation of a pile by vibratory method includes:

- Time of Vibration
- Number of Load Cycles
- Variation of Load Amplitudes

.

During certain unfavourable ground conditions the loading period to install piles may go up-to 30 minutes instead of usual 2 - 10 minutes depending on the depth. Also during unfavourable conditions because of availability of time the system is neither drained nor undrained, it undergoes partial drainage.

2.3.1. Cyclic Behaviour of Sand

The soil is treated as continuum in geotechnical engineering. The aspect of cyclic loading due to the vibrating piles are usually defined by the time of vibration, number of cycles and load amplitude. Excess pore water generation takes place during the pile driving in saturated ground conditions and there may also certain time when the excess pore water is dissipated.

The cyclic behaviour of the sand can be understood in two distinct way,

- Micro Level Behavior
- Macro Level Behavior

The micro-level particle interaction due to the cyclic shearing has been presented in the work of Youd (1977) which is presented here in figure 2.4. Due to shear loading the sand skeleton takes more denser form and the gap is regained while the sand skeleton is under unloading phase. On reversal of strains the gap collapses back and this repeated cycles lead to a condition where not all the strains are recovered during unloading. In case, if the initial state was denser, then soil matrix achieves virgin relative density which will be less denser. But in case of loosely packed sand, the final state is denser than the initial state. The illustration of interaction of the sand particle at micro level, i.e., two particle in contact is explained by Deresiewicz (1958) using Hertz Theory. The plastic shear occurs when the displacement is greater than the diameter of the particle. Due to soil packing being extremely complex and irregular shapes of grains this doesn't occur in the real world. Further, the description of the total quantitative behavior of sand can be depicted by Discrete Element Models.

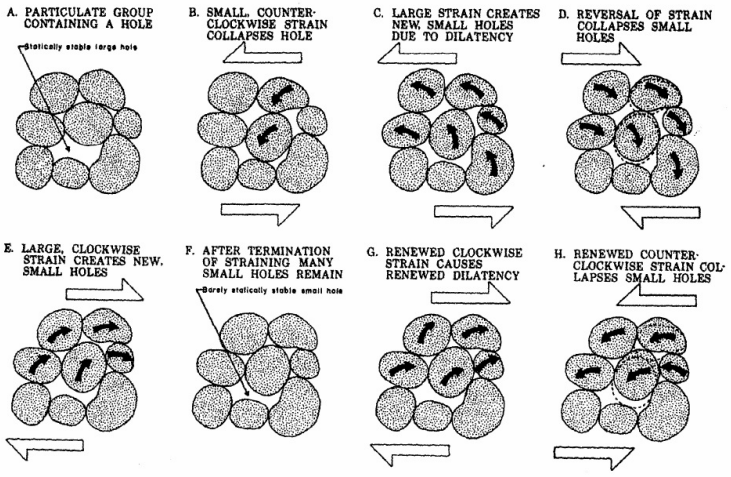

Figure 2.4: The group of soil particle illustrating packing due to cyclic loading Youd (1977)

The cyclic shear loading helps to the building up of excess pore pressure in the porous media. In case of non-cohesive soil in saturated conditions, effects are subdivided as, (a) Near field, (b) Far field. In the near field condition shear strain amplitude is higher and subsequent damping ratio is greater as well but in far field both are greatly reduced due to the impact of the attenuation (Kim & Lee 2000). The magnitude of pore pressure generated is a function of shear strain amplitude.

The amount of cyclic loading applied on the surrounding ground material by the vibration due to circular pile installation can be obtained from various possible models. Most densification model have acceleration as their main loading parameter (Meijers 2007). Cyclic shear loading in the porous media is induced due to the shear waves.

Change in normal stress due to P-Wave can be computed by:

$$\Delta\sigma_n = E\Delta v/C_p \tag{2.9}$$

Where

- $\Delta\sigma_n$ = stress amplitude
- Δv = velocity amplitude

- E = Young's modulus
- C_P = P-wave velocity

The change in the normal stresses due to the P-wave loading (acceleration) is negligible on the surface and increases with depth. When the speed of deformation is low, the system gets enough time to drain but when loading is quicker, there is no sufficient time for dissipation to occur. This restricts any volumetric strain, but due to increasing pore pressure the re-arrangement of grains within the fixed volume is carried out leading to the reduction of inter-particle stress and liquefaction happens in certain cases.

2.3.2. Laboratory simulation of cyclic loading

Various methods can be adopted to understand the effect of cyclic loading in laboratory. But the most fitting ones to easily correlate the work done in Rotterdam port is by cyclic triaxial and simple shear test. Before getting into the effects of cyclic effects, the differences between triaxial and simple shear are presented.

Triaxial Test

The triaxial test is most widely used to understand the mechanical properties of the soil. The optimal height to diameter ratio is provided as 2, as end platens restricts the radial displacement leading to inhomogeneity in the test (Ibsen 1994). Also it is recommended if the sample height to diameter is 1, the platens must be lubricated.

The rotation of stress path is not possible in case of triaxial testing, the major principle stress is either vertical/radial stress. The stress path can either be triaxial compression or triaxial extension and deviatoric loading. In case of triaxial compression or extension the cell pressure is kept constant. But in case of deviatoric loading the cell pressure vary with the axial stress. The maximum shear stress occur at $(45° + \phi)$

Stress Components:

- Shear Stress = $\frac{(\sigma 1 - \sigma 3)}{2}$
- Normal Stress = $\frac{(\sigma 1 + \sigma 3)}{2}$

Simple Shear Test

Simple Shear test is a plain strain test, principle axis of stress and strain rotates. The sample in this test is loaded horizontally with vertical(static) load. Simple shear is more accurate to the practical situations. In this test complementary shear stress (Stress contributed by Poisson's ratio) are prohibited in the vertical boundaries along the plane of deformation and thus the sample is subjected to non- uniform distribution of stresses leading to the difficulties in interpretation of the results. There is also an in-homogeneity on the boundary of vertical ends of the sample and due to this constrained boundary there is near zero shear stress. Further, the elongation of the membrane in axial direction during shearing may also induce some shear stress. The results are assumed to be purely shear that remains highly questionable. The horizontal stress remain unmeasured in this case.

Comparison of cyclic triaxial and simple shear test for pore pressure generation

Several investigation were carried out and relationship of excess pore pressure generated in various tests were equated with a correction factor. The relationship provided by Seed.H (1979), has been reviewed by further works.

The relationship between the field, simple shear and the triaxial test is as follows:

$$(\frac{\tau}{\sigma'_{v0}})_{field} \approx 0.9(\frac{\tau}{\sigma'_{v0}})_{simpleshear} \approx C_R(\frac{\sigma'_d}{2\sigma'_0})_{triaxial} \tag{2.10}$$

Here C_R = 0.57 for K_0=0.4 and C_R = 0.9 for K_0=1

Later, based on the work by Seed.H (1979), the stress controlled relationship was provided by Yoshimi.Y & N (1994).

$$(\frac{\tau}{\sigma'_{v0}})_{field} \approx 0.9(\frac{1 + 2K_0}{3})(\frac{\sigma_d}{2\sigma'_c})_{triaxial} \tag{2.11}$$

where

- τ = Shear stress on the sample
- σ_{v0} = Effective vertical stress
- K_0 = Ratio between horizontal and vertical stress.
- σ_d = Deviatoric stress
- σ_c' = Effective confined stress

2.3.3. Shear Stress Attenuation

The main factor affecting the amplitude is distance,

$$\tau(r) = \tau(r = r_0) * (r/r_0)^n \tag{2.12}$$

Where

- $\tau(r)$ = shear stress amplitude at distance r
- $\tau(r = r0)$ = shear stress amplitude at distance r_0
- r = considered distance
- r_0 = reference distance
- n = attenuation parameter, negative for decreasing shear stress amplitude

The value of n = -0.5 without any material damping and it can increase upto -1.0 to include material damping.

2.3.4. Velocity amplitude attenuation

To understand the velocity amplitude, simple empirical relation from CUR can be used.

$$v(r) = v_0\sqrt{\frac{r_0}{r}} * exp(-\alpha(r - r_0)) \tag{2.13}$$

Where

- v(r) = amplitude of the velocity at the distance r
- v_0 = amplitude of the velocity at the distance r_0
- α = A parameter accounting for material damping.

The centrifugal force also plays a part in determining the velocity amplitude.

2.4. Pore Pressure

Pore water pressures can have a significant impact on the inner slope stability of dikes. Ignoring the uncertainties in pore water pressures can thus lead to a serious over or under estimation of the slope stability.
The total stress is the sum of effective stress and the excess pore pressure.

$$\sigma = \sigma' + u \tag{2.14}$$

where,

- σ = Total stress
- σ' = Effective stress
- u = Pore pressure

Due to dynamic shear loading in dense sand, sand will undergo dilation which leads to rise in porosity of the soil. At this moment, there is insufficient time for water to flow in. This leads to the generation of suction pressure which prevents further dilation and increase in effective stress.

$$\sigma' = \sigma - (u - \Delta u_{suction}) \tag{2.15}$$

In loose sand, dynamic shear loading causes contraction due to the decrease in porosity but water cannot flow out. This leads to excess pore pressure reducing the effective stress.

$$\sigma' = \sigma - (u + \Delta u_{suction}) \tag{2.16}$$

In saturated conditions, due to effects of vibration soil undergoes continued deformation at constant low residual stress or with residual resistance, due to build up and maintenance of high pore pressure. This phenomenon is liquefaction (Rahman et al. 1977). Liquefaction is distinguished into two types (Whenham & Holeyman 2012):

- Flow Liquefaction
- Cyclic mobility

In dry conditions, due to the effects of vibration there will be shear strength reduction in granular material due to high acceleration (Barkan 1962). The shear strength of the cohesion-less soil is dependent on the inter-granular contact which gets impacted due to acceleration (Rodger & Little John 1980).

- elastic state ($a > 0.6g$)
- trans-threshold state ($0.7g < a < 1.5g$)
- fluidized response state ($a > 1.5g$)

2.5. Pore Pressure Generation Models

Cyclic loading of soil can be modelled using different approaches like for example the most commonly used stress based approach of Seed and Rahman (Martin et al. 1975). There are models developed based on strain applied, acceleration and energy dissipation.

2.5.1. Acceleration based model

Barkan's Model

Barkan's model is principally a settlement prediction model based on the changes in void ratio due to the effective acceleration magnitude. In this work, a unique non linear relationship between void ratio and acceleration amplitude is pointed out.

$$e = e_{min} + C.e^{(-\alpha_B \eta)} \tag{2.17}$$

where,

- e: final void ratio
- e_{min}: minimum void ratio
- α_B: coefficient of vibratory compaction
- η: acceleration amplitude
- C: Constant

$$e = e_{min} + (e_{max} - e_{min}).e^{-\alpha_B \eta} \tag{2.18}$$

$$e = e_{min} + (e_{max} - e_{min}).e^{-\alpha_B (\eta + \eta_0)} \tag{2.19}$$

where,

- e_{min}: minimum void ratio [-]

- e_{max}: maximum void ratio [-]
- η_0: acceleration amplitude below which no densification occurs

$$\eta_0 = \frac{\ln(1 - I_D)}{\alpha_B} \tag{2.20}$$

where,

- η_0: threshold acceleration below which no densification occurs
- I_D: Relative Density

In this model for the value of e_{min} and e_{max} laboratory tests are required. Based on the Rotterdam port case study as laboratory test data is not available, for the generation of the excess pore pressure data Barkan's model is not used.

2.5.2. Stress based model

Seed and Rahman

Seed and Rahman's model is best suited to simulate the generation of excess pore pressures under completely saturated condition. The model is dependent on the empirical relationships derived from the stress controlled cyclic testing. The model also accounts for pre-shearing. The development of the pore pressure can be described by the ratio between excess pore pressure and initial effective stress(r_u).

$$r_u = \frac{2}{\pi} arcsin(\frac{N}{N_{liq}})^{\frac{1}{2\theta}} \tag{2.21}$$

where,

- r_u: relative excess pore pressure
- N: applied number of cycles
- θ: empirical parameter, a reasonable estimate is $\theta = 0.7$
- N_{liq}: Number of cycles to liquefaction in an undrained situation [-]

The value of N_{liq} can be adopted in an empirical relationship (Engineering 1987):

$$\frac{\frac{\Delta\tau}{\sigma'_{v0}}}{I_D} = a.N_{liq}^{-b} \tag{2.22}$$

where,

- $\Delta\tau$: shear stress amplitude
- σ'_{v0}: initial effective vertical stress
- a, b: empirical parameters, reasonable estimates are $a = 0.48$, $b = 0.2$ (Meijers 2007)

In order to determine the value of N_{liq}, there is a need for adjustment of the soil skeleton due to continuous generation and dissipation of excess pore pressure which is not possible because it ignores the soil fabric from consideration. However, following empirical relationships may be applied:

$$N_{liq} = N_{liq,0} * 10^{-X\Delta n} \tag{2.23}$$

where,

- N_{liq}: Number of cycles to liquefaction after change in porosity of Δn
- $N_{liq,0}$: Number of cycles to liquefaction without pre-shearing [-]
- X: History parameter
- Δn: Change in porosity (in unity)[-]

2.5.3. Strain based model

A semi-empirical model was developed based on the strain controlled cyclic test performed on dry sand. A relationship was established between volumetric straining and excess pore pressure in both dry and saturated condition (Martin et al. 1975).

$$\Delta u = E_r.\Delta\epsilon_{vd} \tag{2.24}$$

where,

- Δu: Increment of excess pore pressure
- E_r: Tangent modulus of one-dimensional unloading curve corresponding to the initial effective vertical stress
- $\Delta\epsilon_{vd}$: Volumetric straining contributed from the cyclic loading

Martin et al.(1975**)**

$$E_r = \frac{(\sigma_v')^{1-m}}{m.k_2.(\sigma_{v0}')^n - m} \tag{2.25}$$

$$\Delta\epsilon_{vd} = c_1(\gamma - c_2.\epsilon_{vd} + \frac{c_3.\epsilon_{vd}^2}{\gamma + c_4 + .\epsilon_{vd}}) \tag{2.26}$$

where,

- σ_v', σ_{v0}: vertical and initial vertical effective stresses
- γ: induced cyclic shear strain
- ϵ_{vd}: accumulated volumetric strain
- c_i, m, n, k_2: model coefficients

The recommended values for $c_1, c_2, c_3, c_4 = 0.80, 0.79, 0.45$ and 0.73 respectively and are empirical values. In case of different relative density other than 45%, there is a need to introduce a correction factor:

$$(\Delta\epsilon_{vd})D_{R1} = R.(\Delta\epsilon_{vd})_{RD=45} \tag{2.27}$$

Further, R is a function of RD for crystal silica sands, given by the following Silver & Seed (1971):

$$R = 0.00031.(100 - RD)^2 + 0.062 \tag{2.28}$$

For $45 < RD < 80\%$. In this work the cyclic shear strain (γ) response was formulated:

$$\gamma = \frac{\tau.a}{\sqrt{\sigma_v'} - \tau.b} \tag{2.29}$$

$$a = A_1 - \frac{\epsilon_{vd}}{A_2 + A_3.\epsilon_{vd}} \tag{2.30}$$

$$b = B_1 - \frac{\epsilon_{vd}}{B_2 + B_3.\epsilon_{vd}} \tag{2.31}$$

where,

- τ: Cyclic shear stress
- $A_1, A_2, A_3, B_1, B_2, B_3$: Model coefficients

Finn et al.

The volumetric strain is the summation of elastic and plastic components. The plastic volumetric strain with one complete cycle was given by

$$\Delta\epsilon_{vol} = \Delta\epsilon_{vol}^{el} + \Delta\epsilon_{vol}^{pl} \tag{2.32}$$

$$\Delta\epsilon_{vol}^{pl} = C_1[\Delta\gamma - C_2\epsilon_{vol}^{pl} + \frac{C_3(\epsilon_{vol}^{pl})^2}{\Delta\gamma + C_4\epsilon_{vol}^{pl}}] \tag{2.33}$$

where,

- C_1, C_2, C_3, C_4: Empirical parameters
- $\Delta\gamma$: Shear strain amplitude
- ϵ_{vol}^{el}: Elastic Volumetric Strain
- ϵ_{vol}^{pl}: Plastic Volumetric strain

With combination of strain history and strain amplitude the parameter κ(damage parameter), the magnitude of excess pore pressure can be assessed. This is called damage parameter approach.

Byrne et al.

The work of Martin et al. was further simplified by the introduction of incremental volumetric strain by Byrne (1991).

$$\Delta\epsilon_{vd}/\gamma = c_1.\exp -c_2.\frac{\epsilon_v d}{\gamma} \tag{2.34}$$

where c_1 and c_2 are derived using the following equation:

$$c_1 = 7600.(RD)^2.5 \tag{2.35}$$

$$c_2 = \frac{0.4}{c_1} \tag{2.36}$$

2.5.4. Energy based model

In the recent years there have been a lot of efforts made to correlate the generation of excess pore pressures to the dissipated energy during cyclic loading. In the case of cohesionless soil like the sand, predominant mechanisms of energy dissipation are the frictional sliding at grain-to grain contact and in the case of saturated soils, viscous drag of pore fluid moving relative to the soil skeleton. For large strains the energy dissipation due to viscous drag becomes small compared to the frictional energy dissipation (Green & Mitchell 2004). Therefore in this approach the energy dissipation due to viscous drag will be neglected. This mechanism is further neglected in the interpretation of the cyclic test results, used for the drafting of the empirical relation between energy dissipation and excess pore pressure.
The dissipated energy per unit volume is given by:

$$E_{dis} = \int \sigma d\epsilon^p \tag{2.37}$$

For a simple shear test, the energy dissipation is described by:

$$E_{dis} = \int \tau d\gamma = \int \tau(t) * \gamma(t) dt \tag{2.38}$$

where:

- ΔE_{dis}: Dissipated energy
- σ: Stress [kPa]
- ϵ_p: Plastic strain [-]
- τ: Shear stress [kPa]
- γ: Shear strain [-]

In the past there have been a few empirical equations developed for the relation between dissipated energy and excess pore pressure. Here is an overview of few equations from different authors from the work of Green & Mitchell (2004).

$$r_u = \alpha(\frac{\Delta E_{dis}}{\sigma'_{v0}})^\beta \tag{2.39}$$

or:

$$r_u = 1 - \exp(-\alpha\frac{\Delta E_{dis}}{\sigma'_{v0}}) \tag{2.40}$$

with:

- α: Empirical parameter
- σ'_{v0}: Initial vertical effective stress

A version of the eq 2.38 is in the notation of the GMP (Green Mitchell Polito) model.

$$r_u = \sqrt{\frac{\Delta E_{dis}}{PEC}} \tag{2.41}$$

with:

- PEC: Pseudo energy capacity, a calibration parameter

Before using the energy dissipation model some guidance is needed for selecting the value of PEC. A wide variety of cyclic triaxial and cyclic simple shear tests with different types of sand were used to come up with the following summary:

- PEC value increases with increasing relative density
- PEC is not only a function of relative density but also shear strain amplitude
- All the different tests conducted show a large variation or scatter of PEC values

So, in order to derive an expression that can be used as a first estimate for the dissipated energy at liquefaction (PEC), representative values from different sources are selected and plotted in figure 2.5 (Meijers 2007).

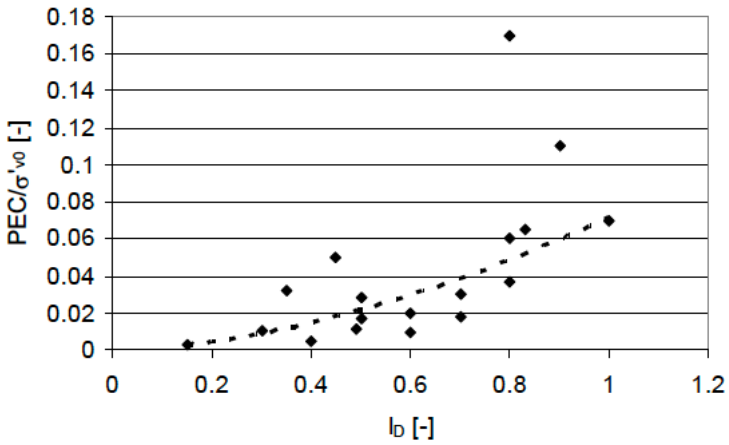

Figure 2.5: Relation between PEC and relative density, summary of all data

From figure 2.5 the following empirical relation is derived as the estimate for the value of PEC as a function of relative density.

$$\frac{PEC}{\sigma'_{v0}} = 0.07 * I_D^{1.7} \tag{2.42}$$

It is to be realised that this value is derived neglecting the possible influence of the cyclic stress ratio on the value of PEC, it is therefore to be used as a first estimate for the value of PEC (Meijers 2007).

With this approach it requires that for determining energy dissipation, the stress-strain behaviour of each soil element be assessed for each and every cycle, which is not very practical in the view of large number of cycles. Therefore in this work, another approach will be used for the determination of energy dissipation:

$$E_{dis,1} = 2\pi * \tau_{max} * \gamma_{max} * D(\gamma) \tag{2.43}$$

where,

- E_{dis}: Dissipated energy per cycle
- τ_{max}: maximum shear stress
- γ_{max}: maximum shear strain
- $D(\gamma)$: Damping ratio (function of shear strain)

With equation 2.42 the energy dissipation per cycle is determined first and then it is integrated over the number of cycles to get the energy dissipation at the end of the cyclic loading. Only unknown in this equation is the damping ratio, which is a function of shear strain. The damping ratio is defined as (Meijers 2007):

$$D = \frac{1}{4\pi} \frac{E_{dis}}{0.5\Delta\gamma\Delta\tau} \tag{2.44}$$

with:

- D = Damping ratio
- $\Delta\gamma$ = Shear strain amplitude
- $\Delta\tau$ = Shear stress amplitude

In the literature there have been wide range of test results, where the damping ratio have been measured and plotted as shown in the figure 2.6. From these tests we can follow that damping ratio is a function of shear strain amplitude.

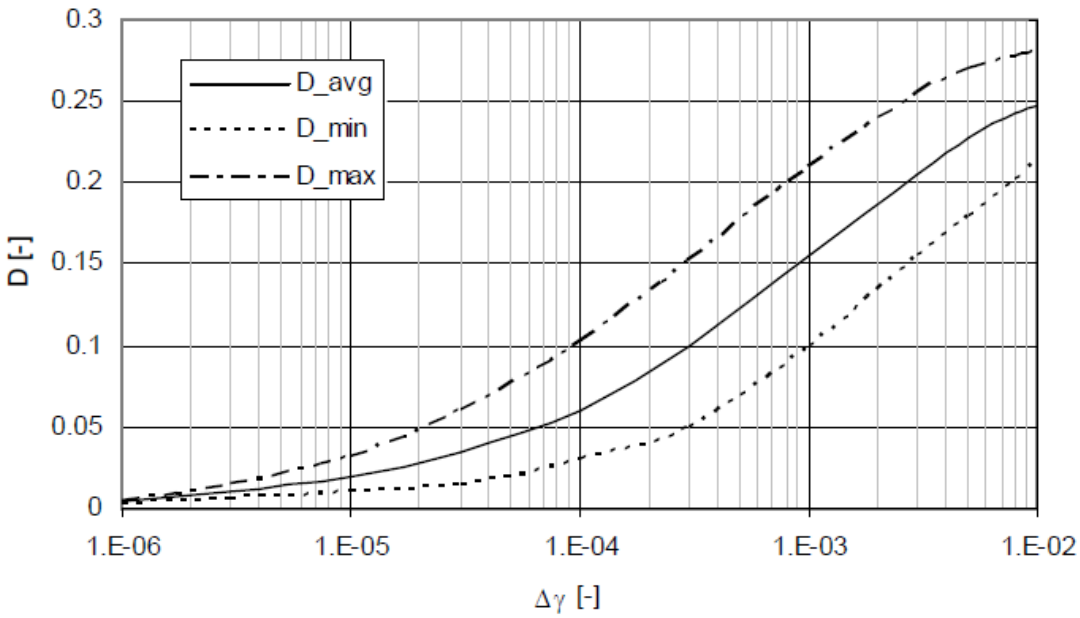

Figure 2.6: Damping ratio as a function of shear strain amplitude (Seed et al. 1986)

In TRILDENS3 the damping ratio as a function of the shear strain amplitude is described with the following relation, being a fit of the curve in the figure:

$$D = (0.75 + 0.125\log(\Delta\gamma))^2 \tag{2.45}$$

This gives for $\Delta\gamma = 10^{-6} : D = 0$ and for $\Delta\gamma = 10^{-2} : D = 0.25$.

2.6. Derivation of Energy dissipation model parameters

The energy dissipation method (Green & Mitchell 2004) assumes a relation between the dissipated energy during cyclic loading and the excess pore pressure. In this interpretation a power function is used.

$$r_u = \frac{\Delta u}{\sigma'_{v0}} = [\frac{E_{dis}}{PEC}]^n \tag{2.46}$$

with:

- r_u : excess pore pressure ratio
- Δu : excess pore pressure
- σ'_{v0} : initial effective pore pressure
- PEC : Pseudo energy capacity
- n : empirical parameter

For the purpose of illustration, a number of tests were conducted in the past:

- (13) Cyclic drained triaxial tests with about 15000 cycles
- (16) Cyclic undrained test: continued until liquefaction
- (7) Cyclic undrained with interim drainage and static drained loading

In the cyclic tests, the following parameters are varied:

- Grain size and angularity (two types of sand were used)
- Relative density, relative densities of 0.2, 0.4, 0.6 and 0.8 were used
- Vertical stress amplitude, values of 10 kPa, 20 kPa, 30 kPa, 40 kPa, 60 kPa and 80 kPa were used

In the brackets, the number indicates the total number of tests conducted. The method is illustrated with the test results of test 12.12 (Undraiined cyclic triaxial test). Figure 2.7 shows the relation between the dissipated energy and the relative excess pore pressure. The curve fits with a power function.

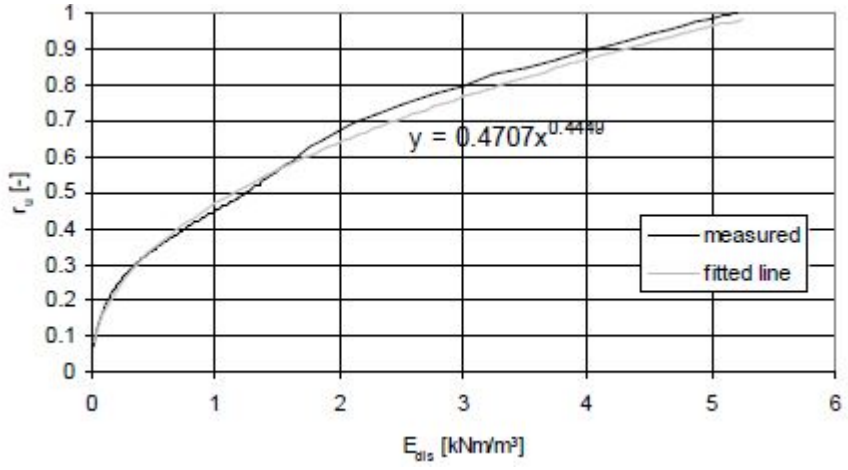

Figure 2.7: Development of excess pore pressure as a function of dissipated energy

From this the following empirical parameters are derived:

- $n = 0.4449 (1/n = 2.248)$
- $PEC^{-n} = 0.4707$, this gives $PEC = 0.4707^{-1/n} = 5.44$

In other versions of the mentioned relation $n = 0.5$ is used. Using this n value an estimate of PEC is made. Rewriting the expression for the excess pore pressure gives:

$$PEC = [\frac{E_{dis}}{r_u^{1/n}}] \tag{2.47}$$

Using the above mentioned relation the value of PEC can be determined for each data point. Figure2.8 shows the value as a function of the applied number of cycles. In the model however the value of PEC is assumed to be a constant, so one single value is to be selected. In this case a value of $PEC = 4.5$ is selected.

Figure2.9 shows the measured development of the excess pore pressure compared with the fitted

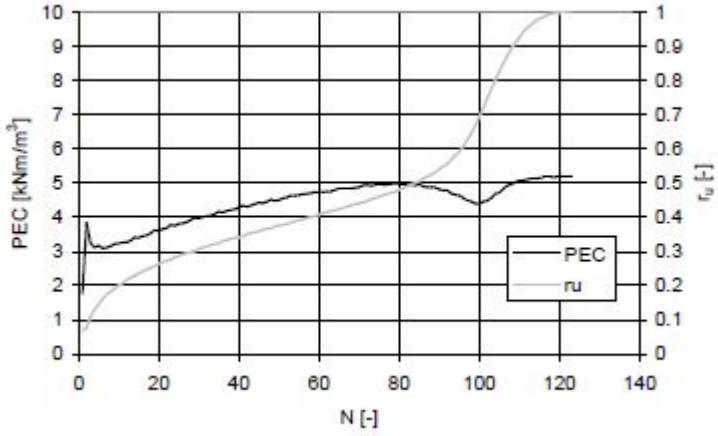

Figure 2.8: Estimated PEC from test data, using $n = 0.5$ (Meijers 2007)

line.

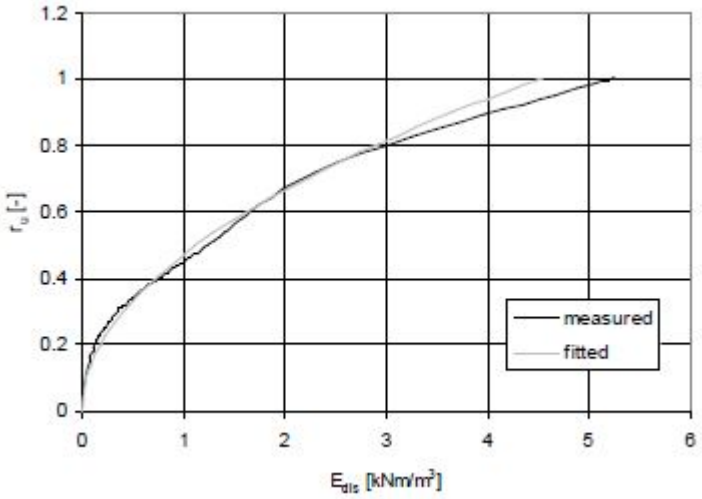

Figure 2.9: Comparison measured and fitted development of the excess pore pressure, using the energy dissipation model (Meijers 2007)

2.7. Empirical parameters for energy dissipation model

The obtained empirical parameters for the above mentioned undrained triaxial tests from the literature review, are given in table 2.1.

For example, from table 2.1 the test 12.10a is performed with a small stress amplitude and resulting strain is amplitude is ($\delta\gamma = 0.8 * 10^{-4}$). After 13,000 cycles the relative excess pore pressure is

Table 2.1: Summary of undrained triaxial tests results for determination of empirical parameters (Meijers 2007)

$Test[I_D]$	$\Delta\sigma_z$	$\Delta\tau\ [kPa]$	$[kPa]$	PEC	n	$PEC(n=2)$
8.21	0.18	36.3	18.1	0.887	1.70	1
8.22	0.38	37.2	18.3	2.01	2.33	1.4
8.23	0.58	37.2	19.0	2.19	1.92	2.3
8.24	0.58	27.5	14.0	1.98	2.02	2
8.25	0.58	18.9	9.6	107.64	3.40	30
8.26	0.38	28.55	14.3	1.40	1.86	1.5
8.27	0.38	19	9.6	3.34	1.94	3.75
8.28	0.18	27.5	14.0	0.67	1.56	0.8
8.29	0.18	19	9.6	1.72	1.68	2.5
8.30 UDU	0.18	18.9	9.6	1.39	1.79	1.8
12.10a	0.61	9.4	4.7			
12.11	0.61	18.9	9.6	100.63	2.79	55
12.11h	0.61	18.9	9.6	165.76	3.39	60
12.12	0.61	38	19.0	5.44	2.247	4.5
12.12h	0.61	37.8	19.1	3.12	2.37	2
12.13	0.61	55	27	5.01	2.37	4
12.13h	0.61	47	23.5	2.71	2.55	2
12.14 UDU	0.61	37.2	18.8	1.50	1.98	1.2
12.15 UDU	0.61	38.35	18.9	3.04	2.21	2.5
12.16 UDU	0.61	37.7	19.1	5.95	2.55	4
12.17 UDU	0.61	37	19.1	2.10	1.92	2.2
12.18a UDU	0.61		14.9	4.39	2.80	2.0
12.18b UDU	0.61	37	18.5	0.89	2.05	0.8

$r_u = 0.04$. Given this small excess pore pressure, this test result was omitted as no reliable empirical parameter can be determined from this result (Meijers 2007).

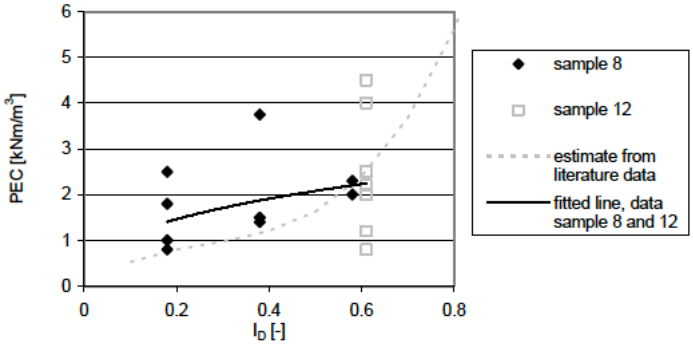

Figure 2.10: Obtained empirical parameter PEC for the energy dissipation model, n=2

Figure 2.10 shows the value of PEC as a function of relative density. In this plot, the results of test 8.25, 12.11 and 12.11h are omitted as they are far outside the range of other values. It can also be seen in the figure 2.10, the scatter of obtained values is large. As the best estimate from all the data, the following relation is obtained:

$$PEC = 3.18 I_D^{0.5} \tag{2.48}$$

Based on the published test results the following relation was derived:

$$\frac{PEC}{\sigma'_{v0}} = 0.7 * I_D^{1.7} \tag{2.49}$$

For purposes of comparison, this relation is also depicted in figure 2.10. For low relative density ($I_D <$

0.6), the values produced by equation 2.48 are in the lower bound of the values produced from the equation 2.47.

2.8. Pore Pressure Dissipation

In loose saturated sandy deposits, when the soil is subjected to shear during a vibratory ground motion, the loose soil grains tend to compact into a denser state leading to the collapse of pore voids within the soil-water matrix. However, given the rapid cyclic shear loading the water in these collapsing pore voids is unable to escape fast enough leading to an undrained condition. Rather than a volumetric contraction, the consequence is an increase in pore water pressure which reduces the frictional contact surface between the soil grams, hence a reduction in effective stress. At this stage the shear strength of the soil is dramatically reduced while the soil grains initially held together are separated and suspended in water. After the ground vibrations have ceased, the soil particles settle in a sedimentation process where particles regain contact and begin taking load (Chian 2015). The excess pore pressure dissipates as commonly expressed as the classic 1-D consolidation equation shown below:

$$\frac{d\bar{u}}{dt} = C_v.\frac{d^2\bar{u}}{dz^2} \tag{2.50}$$

where $\bar{u}$ refers to the excess pore pressure, t is time, z is the depth of the soil and C_v is the coefficient of consolidation in the vertical direction. C_v is directly proportional to the soil's permeability k, and inversely proportional to the compressibility index m_v and the fluid unit weight γ_w as shown below:

$$C_v = \frac{k}{m_v.\gamma_w} \tag{2.51}$$

The hydraulic conductivity of the soil K is dependent on the permeability of the soil k and the density of pore fluid ρ_w. μ and g are the dynamic viscosity of fluid and acceleration due to gravity respectively.

$$K = k\frac{\rho_w g}{\mu} \tag{2.52}$$

2.8.1. Excess Pore Pressure Dissipation Models

In the past there have been several excess pore pressure dissipation models developed based on the results of shaking table and centrifuge tests. Florin and Ivanov (Florin & Ivanov 1961) observed that the curves representing maximum excess hydraulic pressure versus soil depth resembled a trapezoidal profile. After shaking, consolidation took place and excess pore pressure decreased with the boundary of the consolidated soil moving upwards to the surface. Dissipation of excess pore pressure was more rapid in more permeable coarse-grained soils as compared to fine-grained ones. In the work done by Scott (1986) it was suggested that the trapezoidal profile from Florin & Ivanov (1961) is applicable for only rigid soil grains which do not compress significantly with overburden stress as solidification layer increases.

Previous research conducted at the University of Cambridge by Brennan & Madabhushi (2011) proposed a Fourier series to fit the curvature of dissipating excess pore pressure following a full liquefaction event in centrifuge tests as shown in the equation below:

$$\bar{u}(z,t) = \sum \frac{8.\gamma'.H}{n^2.\pi^2}.\sin(\frac{n.\pi.z}{2.H}).\sin(\frac{n.\pi}{2}).\exp -C_v.(\frac{n.\pi}{2.H})^2.t \tag{2.53}$$

where H and z are the height of the entire soil stratum and the specific soil depth used in the study respectively. The parameter C_v can also be obtained, provided there is some experimental data present. The above Fourier series can be readily fitted to experimental data and automatically satisfies the boundary conditions of $\bar{u} = 0$ at $z = 0$ and $d\bar{u}/dz = 0$ at $z = H$. However the model involves a number of terms which may over-fit curves onto noisy data points.

Kim et al. (2009) also developed am empirical dissipation model as shown below. The model was developed by combining the non-linear model of the solidification velocity with Scott's theory (Scott 1986).

$$H = \frac{t}{a + b.t} + c.t \tag{2.54}$$

$$u_G(z,t+dt) = u_G(z,t) + \beta(u_G(z+dz,t) + u_G(z-dz,t) - 2u_G(z,t)) + \gamma'.dH \quad (2.55)$$

where u_G is the excess pore pressure, H is the thickness of the solidified layer, a and b are parameters used to simulate initial solidification velocity near the bottom, and c is the parameter used to simulate final solidification velocity near the surface of the soil deposit. β is a consolidation dependent parameter $(= c_v.dt/dz^2)$. This method has the advantage that it corrects Scott's assumption that the solidification velocity is constant. However. the model introduces 3 additional model parameters $(a, b \ \& \ c)$ which are dependent on the D_{30} grain size and relative density (D_r) of the soil.

2.9. Summary

In this chapter the physical processes occurring during the vibratory pile driving is introduced along with the different types of waves generated during the process. This explains the degradation of sand due to cyclic loading. Further it is dependent on the attenuation factor and the distance from the source. The further the vibration attenuates from the source, smaller the degree of degradation. The magnitude of degradation is also linked to the generation of excess pore pressure, crushing of grains at interface and decrease in friction angle (Meijers 2007). But for the case of this study, emphasis has only been put on excess pore pressure generation which is explained with the help of different pore pressure models out of which one will be used for computation in chapter 4. Along with pore pressure generation, pore pressure dissipation is also discussed in this chapter.

3

Slope stability analysis

3.1. Introduction

Slope stability analysis is a static or dynamic, analytical or empirical method to evaluate the stability of earth and rock filled dams and embankments, excavated and natural slopes in soil and rocks. This chapter revisits the different types of slope stability analysis available.

Slopes can be distinguished in two types: natural slopes and man made slopes. Natural slopes are those that exist in nature and are formed by natural causes, such slopes exist in hilly areas. The sides of cuttings, the slopes of embankments constructed for roads, railway lines, canals and the slopes of earth dams constructed for storing water are examples of man made slopes (V.N.S. 2002). The slopes whether natural or artificial may be:

- Infinite slopes
- Finite slopes

Infinite slope ”term is used to designate a constant slope of infinite extent”. The slope of a mountain’s face would be an example of infinite slopes. For the case of finite slopes, the slope lengths are limited in extent (V.N.S. 2002). For example, the slopes of embankments and earth dams would be termed as finite slopes.

3.2. Slope Stability

Slope stability refers to the condition of inclined soil or rock slopes to withstand movement and slope stability analysis is a way to evaluate the stability of the rock slopes or inclined soil against this movement. Ignoring slope stability analysis could often lead to devastating results, causing damage to infrastructure and possible loss of life. Factors leading to instability in a slope and furthermore failure of a slope are:

- Gravitational force
- Water Seepage
- Earthquakes
- Erosion of surfaces due to flowing water
- Sudden drawdown of water levels

The effect of all the forces listed above is to cause movement of soil from high points to low points. The most important of such forces is the component of gravity that acts in the direction of probable motion. The various effects of flowing or seeping water are generally recognized as very important in stability problems, but often these effects have not been properly identified. It is a fact that the seepage occurring within a soil mass causes seepage forces, which has a dominant effect on slope stability.

A far as mass movement is concerned, erosion may lead to increase in stability as it erosion on surface would remove a certain weight of the soil. On the other hand, erosion in the form of undercutting at the toe may increase the height of the slope, or decrease in length of the impeding failure surface, thus decreasing the stability.

Considering lowering of the ground water or of a free water surface adjacent to the slope, for example in a sudden drawdown of the water surface in a reservoir there is a decrease in the buoyancy of the soil which is in effect an increase in the weight. This increase in weight lead to increase in the shearing stresses that may or may not be in part counteracted by the increase in shear strength, depending upon whether or not the soil is able to undergo compression. If a large mass of soil is saturated and is of low permeability, practically no volume changes will be able to occur except at a slow rate, and in spite of the increase of load the strength increase may be insignificant to counteract the load increase.

Shear at constant volume may be accompanied by a decrease in the intergranular pressure and an increase in the neutral pressure. A failure may be caused by such a condition in which the entire soil mass passes into a state of liquefaction and flows like a liquid. A condition of this type may be developed if the mass of soil is subject to vibration, for example, due to earthquake forces or a slope subjected to vibratory pile driving or impact pile driving.

3.3. General considerations and assumptions

There are three distinct steps for a slope stability analysis (V.N.S. 2002):

- **Testing of samples to determine the cohesion and angle of internal friction:** For analysis a natural slope, it is imperative that the sample be undisturbed. When considering the state of initial consolidation and rate of shear application, the condition of testing should represent as closely as possible to unfavourable conditions which are likely to occur in the slope.

- **The study of known parameters but which cannot be accounted for in computations:** The most important of such items is progressive cracking which will start at the top of the slope where the soil is in tension, and aided by water pressure, may progress to considerable depth. In addition, there are the effects of the non-homogeneous nature of the typical soil and other variations from the ideal conditions which must be assumed.

- **Computations:** If a slope is to fail along a surface, all the shear strength must be overcome along that surface which then becomes a surface of rupture.
  If it is assumed that the problem is two dimensional, which theoretically requires a long length of slope normal to the section. However, if the cross section investigated holds for a running length of roughly two or more times the trace of the rupture, it is probable that the two dimensional case holds within the required accuracy. The shear strength of soil is assumed to follow Coulomb's law

$$s = c' + \sigma' \tan \phi' \tag{3.1}$$

  where, c', σ' and ϕ' are effective unit cohesion, effective normal stress in the surface of rupture and effective angle of internal friction respectively.

3.4. Factor of Safety

In stability analysis, two types of factors of safety are normally used. They are:

- Factor of safety with respect to shear strength

- Factor of safety with respect to cohesion

The factor of safety with respect to shear strength, F_S may be written as:

$$F_S = \frac{s}{\tau} = \frac{c' + \sigma' \tan \phi'}{\tau} \tag{3.2}$$

where, τ is the average value of mobilized shear strength. The shear strength mobilized at each point on a failure surface may be written as:

$$\tau = \frac{c'}{F_S} + \sigma' \frac{\tan \phi'}{F_S} \tag{3.3}$$

or

$$\tau = c'_m + \sigma' \tan \phi'_m \tag{3.4}$$

where,

- $$c'_m = \frac{c'}{F_S} \tag{3.5}$$
- $$\tan \phi'_m = \frac{\tan \phi'}{F_S} \tag{3.6}$$

and F_s, c'_m, ϕ'_m and s are factor of safety with respect to strength, mobilized cohesion, mobilized angle of friction and maximum shear strength respectively.

3.5. Method of stability analysis for finite slope

Failure on finite slopes are common issue and in this section different failure surface and types of stability analysis are discussed. The most widely used method of analysis of homogeneous, isotropic, finite slopes is the Swedish method based on circular failure surfaces. This method was used by Petterson (1955) for the analysis of a soil failure in connection with the quarry wall failure in Goeteberg, Sweden. After sstudying a large number of failures, a report was published by a swedish national commission showing ”the lines of failure of most such slides roughly approached the circumference of a circle and the failure circle might pass over, below or through the toe of the slope”. This method has been widely accepted for offering an approximately correct solution for the determination of factor of safety of the slope of an embankment and its foundation. Developments in the method of analysis have been made by Fellenius (1947), Terzaghi (1943), Gilboy (1934), Taylor (1937), Reinius (1955), and others, with the result that a satisfactory analysis of the stability of slopes, embankments and foundations by means of the circle method is no longer an unduly tedious procedure.
Other methods of historic interest such as the Culmann method (1875) and the logarithmic spiral method (Rao et al. 2019) and (Pan et al. 2017). The Culmann method assumes that rupture will occur along a plane. It is of interest only as a classical solution, since actual failure surfaces are invariably curved. This method is approximately correct for steep slopes. The logarithmic spiral method was recommended by Rendulic (1935) (Rao et al. 2020) with the rupture surface assuming the shape of logarithmic spiral. Though this method makes the problem statically determinate and gives more accurate results, the greater length of time required for computation overbalances this accuracy.

Circular surface of failure

Investigations carried in Sweden in the beginning of the century confirms that the shape of a failure surface in an earth slope resemble the shape of a circular arc. When soil slips along a circular surface, such a slide is termed as a rotational slide. It involves downward and outward movement of a slice of earth as shown in figure 3.1 and sliding occurs along the entire surface of contact between the slice and its base. The types of failure that normally occur are classified as:

- Slope failure
- Toe failure
- Base failure

In slope failure, the arc of the rupture surface meets the slope above the toe. This happens when the slope angle β is quite high and the soil close to the toe possesses high strength. Toe failure occurs when the soil mass of the dam above the base and below the base is homogeneous. The base failure occurs particularly when the base angle β is low and the soil below the base is softer and more plastic than the soil above the base. The various modes of failure are shown in figure 3.1 which will be used while assessing the failure surface in the Rotterdam port case study, if there is any.

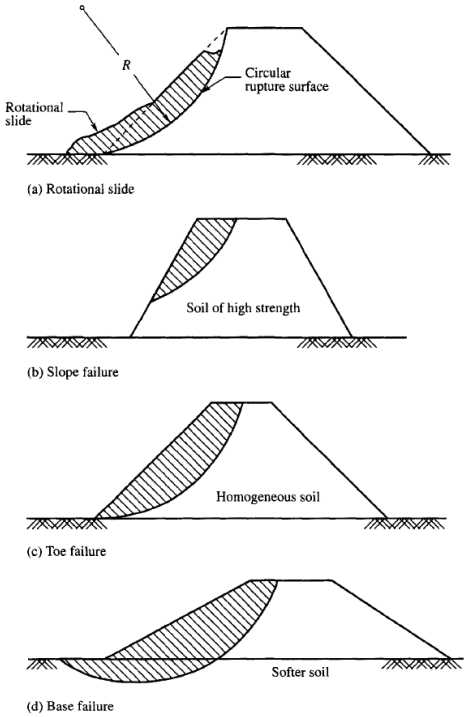

Figure 3.1: Types of failure of earth dams

3.6. Bishop's Simplified Method of slices

When considering a slope with different types of soil and different values of c and ϕ with known pore pressures u in the soil mass, Bishop's method of slices (Reinius 1955) is preferable. For example figure

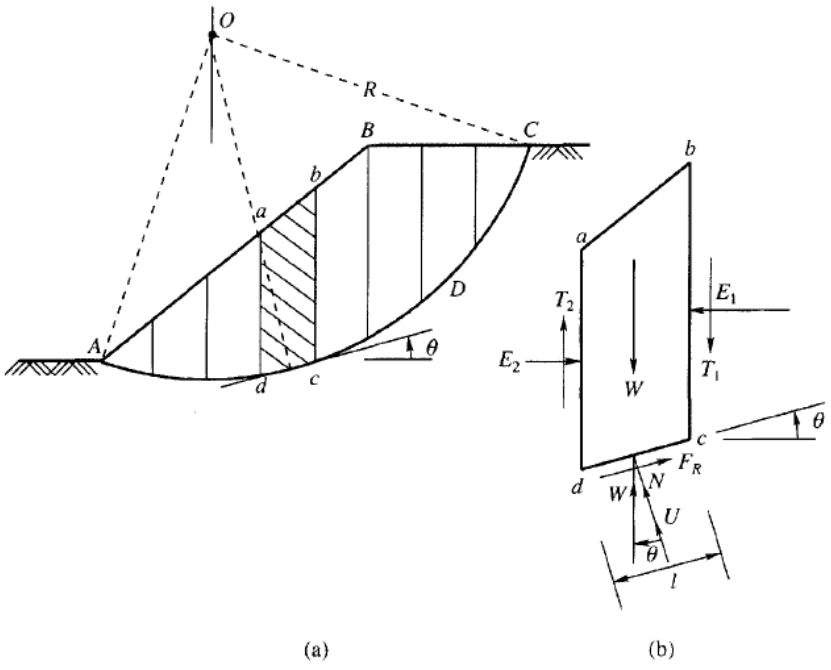

Figure 3.2: Bishop's simplified method of slices (V.N.S. 2002)

3.2 shows a section of an earth dam having a sloping surface AB. ADC is an assumed circular failure surface with its center at O. The soil mass above the failure surface is divided into a number of slices. The forces acting on each slice are evaluated from limit equilibrium of the slices. The equilibrium of the entire mass is determined by summation of the forces on each of the slices.
For analysis a single slice abcd in figure 3.2(a) is considered which is drawn to a larger scale in figure 3.2(b). The forces acting on this slice are:

- W: Weight of the slice
- N: Total Normal force on the failure surface cd
- U: Pore water pressure = ul on the failure surface cd
- F_R: Shear resistance acting on the base of the slice
- E_1, E_2: Normal forces on the vertical faces bc and ad
- T_1, T_2: Shear forces on the vertical faces bc and ad
- θ: The inclination of the failure surface cd to the horizontal

For equilibrium of the system, the following equations hold true.

$$N = W\cos\theta \tag{3.7}$$

$$F_t = W\sin\theta \tag{3.8}$$

where F_t is tangential component of W. The unit stresses on the failure surface of length, l may be expressed as:

$$\text{Normal stress, } \sigma_n = \frac{W\cos\theta}{l} \tag{3.9}$$

$$\text{Shear stress, } \tau_n = \frac{W\sin\theta}{l} \tag{3.10}$$

The equation for shear strength, s is:

$$s = c' + \sigma'\tan\phi' = c' + (\sigma - u)\tan\phi' \tag{3.11}$$

where ϕ' and u are effective angle of friction and unit pore pressure respectively.

- σ': Effective normal stress
- c': Effective cohesion
- ϕ': Effective angle of friction
- u: Unit pore pressure

The shear resistance to sliding on the base of the slice is:

$$sl = c'l + (W\cos\theta - ul)\tan\phi' \tag{3.12}$$

where $ul = U$, the total pore pressure on the base of the slice(figure 3.2(b))

$$sl = F_R \tag{3.13}$$

The total resisting force and the actuating force on the failure surface ADC may be expressed as
Total resisting force F_R is

$$F_R = [c'l + (W\cos\theta - ul)\tan\phi'] \tag{3.14}$$

Total actuating force F_t is

$$F_t = W\sin\theta \tag{3.15}$$

The factor of safety F_S is then given as:

$$F_S = \frac{F_R}{F_t} = \frac{[c'l + (w\cos\theta - ul)\tan\phi']}{W\sin\theta} \tag{3.16}$$

3.7. Spencer Method of analysis

Spencer (1967) developed his analysis based on the method of slices of Fellenius (1927) and Reinius (1955). The analysis is in terms of effective stress and satisfies two equations of equilibrium, the first with respect to forces and the second with respect to moments. The inter-slice forces are assumed to be parallel as in the figure 3.2. This method also assumes that the ratio of the interslice shear force to the interslice normal force is constant throughout the sliding mass. The factor of safety F_S is expressed as:

$F_S : \frac{Shear\ strength\ available}{Shear\ strength\ mobilized}$

The mobilized angle of shear resistance and other factors are expressed as:

$$\tan \phi'_m = \frac{\tan \phi'}{F_S} \tag{3.17}$$

pore pressure ratio,

$$r_u = \frac{u}{\gamma h} \tag{3.18}$$

Stability factor,

$$N_s = \frac{c'}{F_S \gamma H} \tag{3.19}$$

3.8. Phi-c Reduction method

For embankments, for example most of the loading is caused by soil weight and an increase in soil weight would not necessarily lead to collapse. Indeed, a slope of purely frictional soil will not fail in a test in which the self weight of the soil is increased (like in a centrifuge test). A more appropriate definition of the factor of safety is therefore:

$$Factor\ of\ safety = \frac{S_{maximum\ available}}{S_{needed\ for\ equilibrium}} \tag{3.20}$$

Where S represents the shear strength. The ratio of the true strength to the computed minimum strength required for equilibrium (hence, the mobilized strength) is the safety factor that is conventionally used in soil mechanics. For soil models using the standard Coulomb failure condition, the safety factor is obtained as:

$$Factor\ of\ safety = \frac{c - \sigma_n \tan \phi}{c_r - \sigma_n \tan \phi_r} \tag{3.21}$$

The parameters c_r and ϕ_r are reduced strength parameters that are just large enough to maintain equilibrium. The principle described above is the basis of the method of Safety that can be used in PLAXIS to calculate a global safety factor. In this approach the cohesion and the tangent of the friction angle are reduced in the same proportion:

$$\frac{c}{c_r} = \frac{\tan \phi}{\tan \phi_r} = \sum M_{sf} \tag{3.22}$$

The reduction of strength parameters is controlled by a multiplier called $\sum M_{sf}$ that is increased step-by-step until failure occurs. The safety factor is then defined as the value of $\sum M_{sf}$ at failure, provided that at failure a more or less constant value is obtained for a number of successive load steps with ongoing deformations. in order to check if there is stable value of $\sum M_{sf}$, a few points are selected as control points which are likely to be in the failure zone prior to the calculation and then afterwards, its is checked if the control point is in the failure zone and a plot is developed between displacements of this point and $\sum M_{sf}$. From this plot, a stable value of $\sum M_{sf}$ is checked and if not the case, more additional steps are required for the stable calculations.

3.9. Two-dimensional vs Three-dimensional analysis

Generally, the plane strain idealisation adopted in two-dimensional (2D) slope stability computations, assumes three-dimensional (3D) effects are inconsequential. In the case of pile driving, however, due to the presence of a localised zone of vibrations and EPPs (excess pore pressures) extending radially around the pile, these effects may not be negligible. 3D analyses generally provide a less conservative view on slope stability, when compared to 2D calculation (Gitirana, Jr. et al. 2008). 3D analysis is only deemed viable if (1) detailed information on the slope geometry and distribution and properties of soil is available (2) the shape of the failure surface and the direction of failure may be assumed relatively easily, and (3) a 2D analysis yields over-conservative and unrealistic results.

3.10. Summary

With evaluation of factor of safety being the key objective, this chapter focuses on different stability analysis on finite slopes with different types of soil strata. A brief explanation of different stability calculation methods is also introduced along with the difference between a 2-Dimensional and 3-Dimensional approach. With the end of this chapter, the literature review of this project is concluded before moving on to the data analysis on the vibrations data acquired regarding the Calandkanaal project.

4

Port of Rotterdam: Data Analysis

The analysis of the field data from the Calandkanaal, Rotterdam Port plays an important role in the understanding of methodology presented in this thesis. This chapter introduces the two very important aspect of the collected data, understanding of the data and the analysis and processing done on the data. Furthermore, this chapter explains the steps and the calculations made for the generation and the dissipation of the excess pore pressures in the vicinity of the driven pile.

4.1. Calandkanaal

The data was obtained from the project site of Calankanaal which is directly east of the Maeslantkering, near the southern embankment of the Noordzeewegdijk (de Nijs 2019). The piles were driven as a part of the optimisation of mooring places for inland shipping and small coasters in the Calandkanaal.

4.1.1. Soil Information

In the figure 4.1 it can be seen that the various CPTs were conducted for the project, but only CPT S-40 and borehole log B-40 was used for this thesis as those were close to the pile driving site and the only set of data available. The details of the soil profile are derived from the above mentioned borehole log and mentioned in table 4.1 below.

Figure 4.1: Location of all CPTs

The borehole log contains the information of soil profile from the depth of $-13.81mNAP$ to $-33.81mNAP$. The ground water level is at $-0.81mNAP$. As per the borehole log, in the embankment there are mainly two soil types, sand and clay with different particle size and mineralogy. The crest of the embankment is at $+5.70mNAP$. Due to unavailability of the soil information in the collected CPT and the borehole

log, another CPT data was obtained from DINOLOKET. This new CPT data shed new light in the type of the soil in the top part of the embankment. From $+5.70mNAP$ to 0.0, the soil strata is a mixture of sand and clay. Below 0.0 the soil is mostly clean sand till $-13.81mNAP$.

Table 4.1: Soil profile as per borehole log B-40

Depth (mNAP)	Layer thickness (m)	Soil Description
-13.81 to -14.81	1.00	Silt, weakly clayey
-14.81 to -15.01	0.20	Clay, moderately sandy
-15.01 to -15.21	0.20	Silt, weakly clayey
-15.21 to -16.61	1.40	Very fine sand, moderately silty
-16.61 to -18.21	1.60	Moderately coarse sand, weakly silty
-18.21 to -18.81	0.60	Moderately fine sand, slightly silty
-18.81 to -19.01	0.20	Clay, slightly silty
-19.01 to -20.21	1.20	Moderately fine sand, slightly silty
-20.21 to -21.21	1.00	Moderately fine sand, slightly silty
-21.21 to -22.01	0.80	Clay, extremely sandy
-22.01 to -22.21	0.20	Clay, moderately silty
-22.21 to -22.61	0.40	Extremely coarse sand, weakly silty
-22.61 to -23.41	0.80	Moderately fine sand, moderately silty
-23.41 to -33.81	10.40	Extremely coarse sand, slight to moderately silty

4.1.2. Specification of the Vibratory Driver

In this project a PVE 2350 VM vibro-hammer was used. The vibro-hammer has a maximum driving capacity of 2300 rpm or 38Hz with maximum displacement amplitude of 15mm. The maximum centrifugal force is 2900 kN and the eccentric moment is 0-50kgm (Hammer & Moment 2013).

4.1.3. Geometry of the pile

Pile used in the project was an open ended steel tubular pile. This pile was earlier used as truss pole at a different location which was 75m west of the site location before being vibrated out. The diameter of the pile is 1620mm with a wall thickness of 20mm and a length of 21.5 meters. The vibro-driving of this pile has been shown in the figure 4.2.

Figure 4.2: Vibratory Driving of Mooring post 78-T1

4.1.4. Monitoring and Instrumentation

For monitoring the project while pile driving on the slope, four accelerometers were used at different depths at an approximate distance of 3 meters from the location of the pile. The depths of the sensors were -11mNAP, -14mNAP and -17mNAP, with two sensors at the depth of -14mNAP.

Monitoring Sensors

As discussed earlier accelerometer data was available to demonstrate the response of the soil due to the vibratory installation of the circular piles. The data collected were recorded in terms of velocity and frequency throughout the driving of the pile starting from 09:47:41 AM (hrs:mins:sec) to 10:23:06 AM on 26th August 2016 for all the four sensors.

Data Logger

The data collected by the accelerometers were run through the smart box measurement system used in the engineering office of Municipality of Rotterdam. The smart box consists of two parts, the electronics with the data acquisition and the laptop with the processing software. The measuring system measures at 1kHz with Geophones which is obtained in mm/s. This is carried out in the system and is thus processed in all output. Velocities per direction per sensor is also stored.

4.2. Monitoring Data of Calandkanaal

4.2.1. Data acquisition

In Calandkanaal the accelerometer data is collected to understand the effect of the vibrations caused by the vibro-driver on the slope and also see the changes in pore water pressure. The recorded excess pore pressure data was proved to be unreliable and was not made available for this research.
As part of the research was to understand the impact of the driving on the stability of the slope it was imperative to know the right timings of the driving of the pile. The vibro-driver was kept on for the whole duration of 35 minutes, but hammer activity was only executed in three different time intervals summing up to 10 minutes and 49 seconds. Only in these 10 minutes and 49 seconds the pile tip was moving downwards due to the hammer activity but apart from this there was no downward movement of the pile.

4.2.2. Data Processing

The analysis carried out in this research is only on the processed data to reduce inconsistencies, noise and redundant values. The processing of data includes getting rid of inconsistent values which were in the case of velocities and frequencies at some time stamps. The values were deemed irrelevant values because the energy levels outside the hammer activity time period were extremely low and insignificant, therefore the focus is only set to hammer activity data. By the assumption the data involved harmonic vibrations, it was processed using the relation between amplitude, velocity and acceleration using frequency.
And as discussed earlier that in the given data set water pressures were not included because the sensors S2 and S3 gave a very large variation in the measured values which also included negative pore pressures leading to a conclusion that the sensors might have not worked properly.

4.2.3. Understanding Data

Before carrying out any kind of data analysis, it is imperative to understand the observations made from the collected field data. The field data recorded in an excel sheet are in terms of frequency, velocity and acceleration during the duration of pile driving which are discussed separately in the coming pages.

Frequency

The maximum driving frequency of the vibro-hammer used is 38Hz, so it was not surprising to see values of frequency closer to 38Hz, but there were large variation in frequency values outside the hammer activity time interval. In the figure 4.3 below the variation of frequency measured (z-direction or vertically) by sensor 1 (placed at depth -11m NAP) can be seen.

In the figure 4.3, it can be seen there are a few time intervals where the frequency is higher than 100Hz and a similar variation was observed in the data set of other sensors (2, 3 and 4). These higher

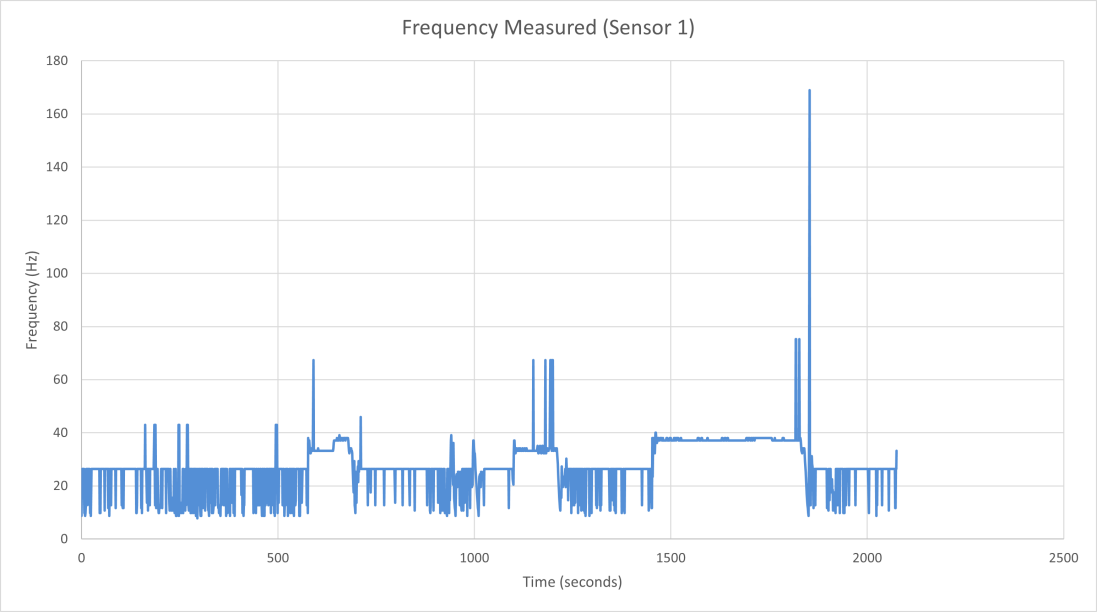

Figure 4.3: Variation of Frequency measured by sensor 1 at -11mNAP

frequency values were considered irrelevant as the constant value of 38Hz was recorded during the hammer activity (de Nijs 2019). Another visualisation was the low frequency readings in the range of 10-20Hz. This could be attributed to the fact that during pile driving, the pile tries to overcome the mobilized friction between soil and pile shaft which causes the mass of soil layer to vibrate at low frequencies (Kim & Lee 2000).

Velocity

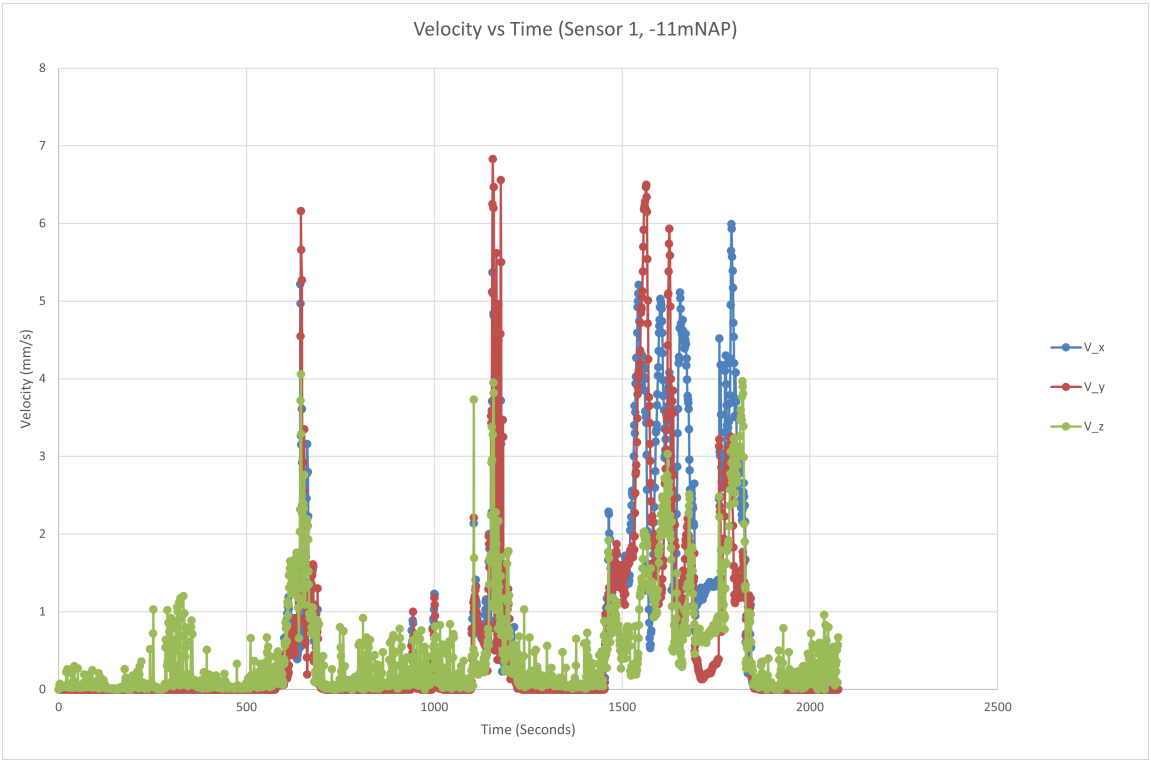

Figure 4.4: Velocity measured by the sensor 1 at -11mNAP, 3m from the skin of the pile

It can be seen from figure 4.4 higher velocities have been registered in the time interval 600-700 seconds, 1100-1200 seconds and 1450-1850 seconds which are the hammer activity time interval. Initially, what was surprising to note in the field data was the higher horizontal particle velocities (V_x, V_y) as compared to the vertical particle velocities(V_z). While in the beginning it could seem that these readings aren't accurate but it is a common phenomenon. These readings happen due to a number of reasons, out of which one could be the lateral movement of the pile during the driving process and other could be the generation of p-waves and s-waves from the pile tip and the pile shaft respectively. Generally, p-waves are responsible for horizontal particle motion and s-waves for vertical particle motion and p-waves travel faster than the s-waves in all soil medium as seen in table 4.2.

Table 4.2: Compression waves and Shear waves for different types of soil (Massarsch 2004)

Soil/Material Type	**P-waves velocity**[m/s]	**S-waves velocity**[m/s]
Ice	3000-3500	1500-1600
Water	1480-1520	0
Granite	4500-5500	3000-3500
Sandstone, Shale	2300-3800	1200-1600
Fractured Rock	2000-2500	800-1400
Moraine	1400-2000	300-600
Saturated Sand/Gravel	1400-1800	100-300
Dry Sand/Gravel	500-800	150-350
Clay below GW level	1480-1520	40-100
Organic Soils	1480-1520	30-50

Another observation from the velocity data is the difference in readings from the sensor 2 and sensor 3 even if they were placed at the same depth($-14mNAP$) and same radial distance ($3\ meters$) from the pile. This can be seen in figure 4.5 and 4.6. During the project it was found that the sensor 3 was showing higher values than expected (de Nijs 2019).

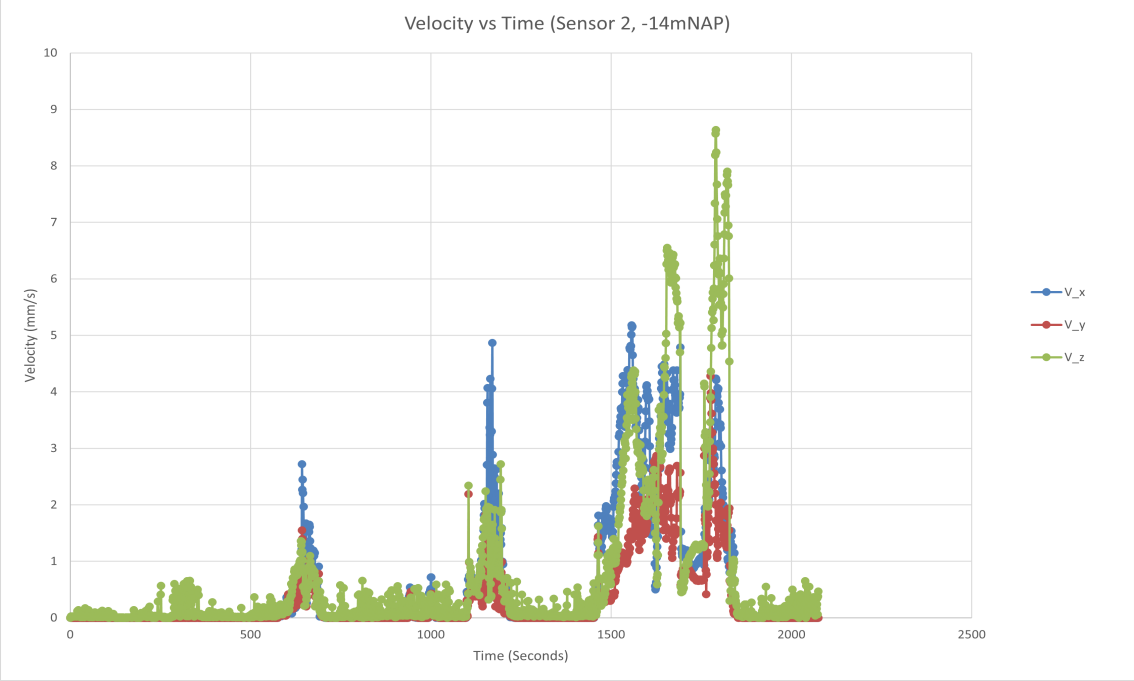

Figure 4.5: Velocity vs Time by sensor 2 at -14 mNAP, at 3m from the skin of the pile

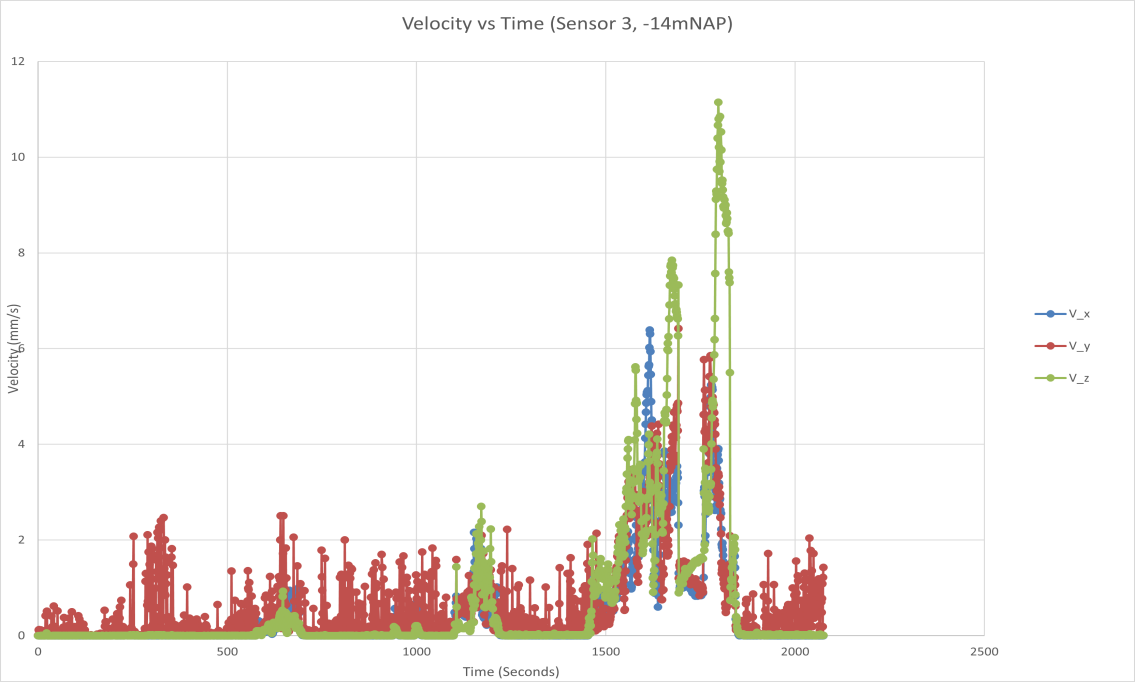

Figure 4.6: Velocity vs Time by sensor 3 at -14mNAP, at 3m from the skin of the pile

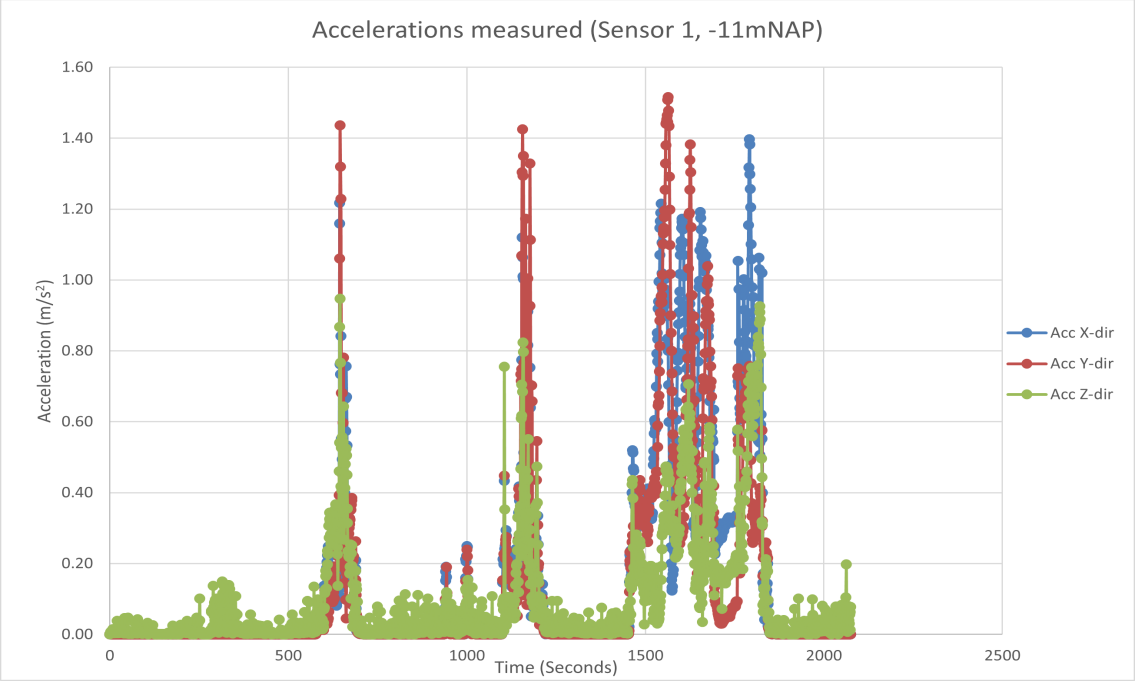

Figure 4.7: Acceleration vs Time by sensor 1 at -11mNAP, at 3m from the skin of the pile

Acceleration

The acceleration values from the data set show a similar trend to what have been seen in the velocity data. This is because of the direct relationship between velocity and acceleration assuming it is a harmonic vibration:

$$a = \frac{2\pi f v}{1000}[m/s^2] \tag{4.1}$$

where, a, f and v are acceleration, frequency and particle velocity respectively measured by the

sensors. Different peak values measured from all the sensors are shown in the table 4.3.

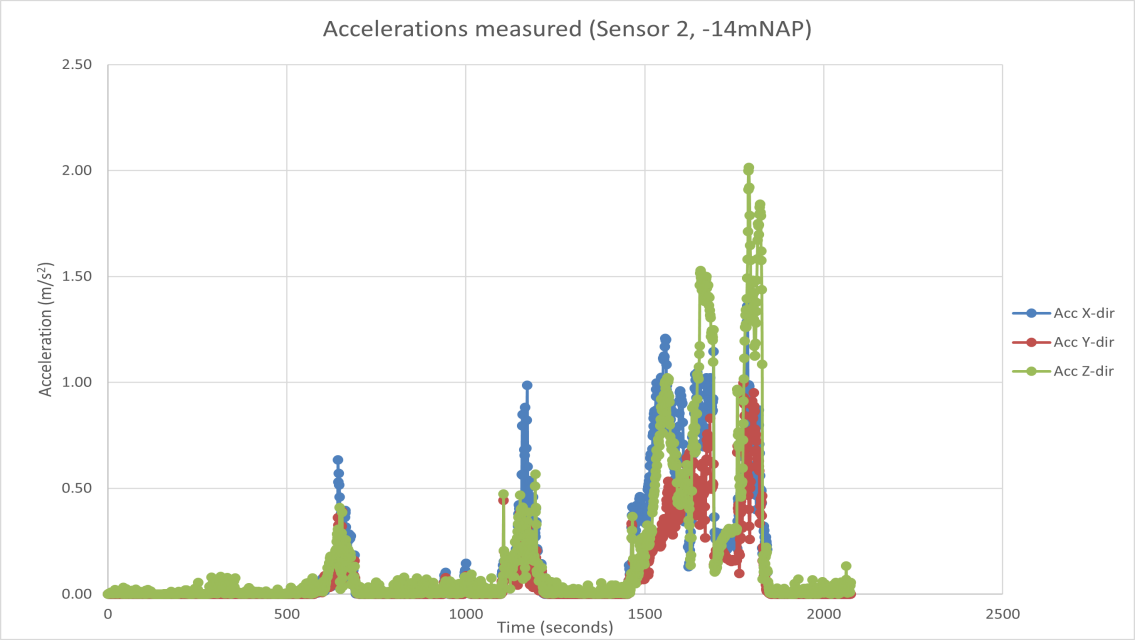

Figure 4.8: Acceleration vs Time by sensor 2 at -14 mNAP, at 3m from the skin of the pile

Sensors	**Peak vertical Acceleration Values (m/s^2)**
1	0.95
2	2.0
3	2.60
4	2.01

Table 4.3: Peak Acceleration values measured

From table 4.3 it was striking to see sensor 3 has the highest recorded acceleration out of the four sensors, even if the sensor 4 was at the maximum depth $(-17mNAP)$ where the soil resistance is higher compared to the location of sensor 3 $(-14mNAP)$. It was also noticed that the sensor 3 recorded different value compared to sensor 2 even if they were at the same depth and radial distance from the skin of the pile (de Nijs 2019).

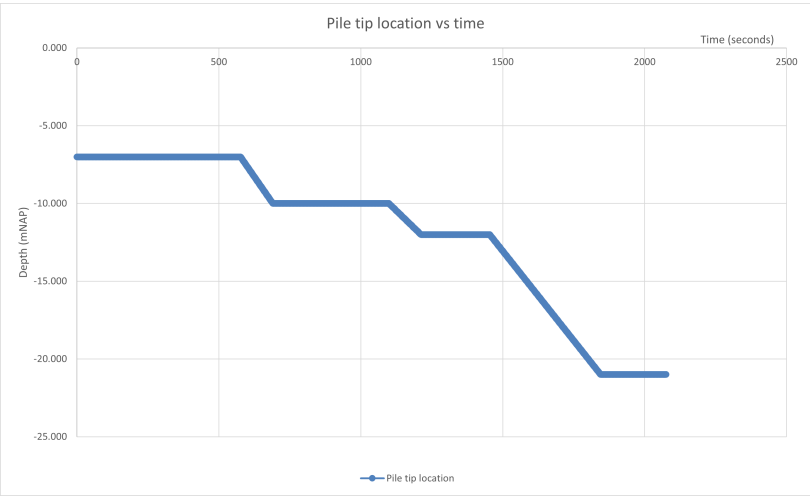

Figure 4.9: Pile tip location with respect to time of driving

4.3. Data Analysis: Vibration attenuation

Many researchers have recorded ground surface vibrations during construction operations. Two categories of empirical models were developed to predict ground motions: (1) attenuation equations with distance from the source and (2) attenuation equations with scaled-distance from the source. It is the horizontal distance from the source to the measuring point that is usually taken as the distance in these relations. However, when a source of vibration other than a point source, like a pile, is generating waves through the soil, the actual distance from the measuring point to the source point may not be the horizontal. So, for the vibration attenuation from the point source such as a driven pile, in this case attenuation equations with distance from the source is used.
The decay of amplitude of vibrations with distance can be attributed to two components, geometric damping and material damping, which are the first and second part of the equation 4.2:

$$w_2 = w_1(\frac{r_1}{r_2})^n e^{-\alpha(r_2-r_1)} \tag{4.2}$$

where, w_1 and w_2 are vibration amplitudes at distance r_1 and r_2 from the source of vibration. n is a geometric damping coefficient, and α is a material damping coefficient (Kim & Lee 2000). The equation 4.2 is one of the earliest empirical correlations which was presented by Bornitz (1931) and is referred to here as the Bornitz equation. The geometric damping occurs due to the decrease of the energy density with distance from the source. Material damping coefficient is dependent on the soil type and frequency of the vibration. It can be represented by:

$$\alpha_m = \frac{2\pi D f}{c_s} \tag{4.3}$$

where, D is the damping ratio of the particular soil, c_s is the shear wave velocity of the propagated wave and f being the frequency of the vibration. For the case of vibratory pile driving, $f = 38$Hz. A commonly used value of the damping ratio D for sand is 5% and the shear wave velocity c_s for the attenuation calculation was considered to be $200m/s$. This results to $\alpha = 0.06m^{-1}$. Data from the sensor 1 along with the equation 4.2 was used to visualise the vibration attenuation over different distances from the source of the vibration.

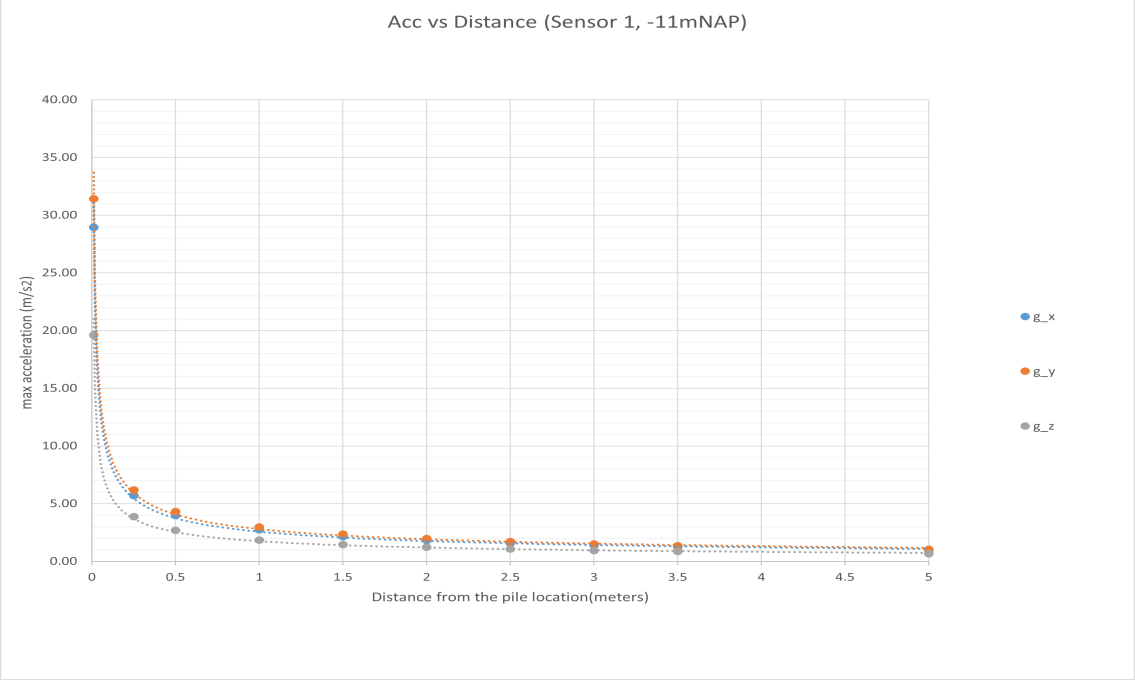

Figure 4.10: Vibration attenuation with respect to distance from the pile

Figure 4.10 shows the vibration attenuation at the depth of -11mNAP. To plot the figure 4.10 the maximum acceleration value at 3 meter from the pile during the whole duration of hammer activity was

used with the equation 4.2. The calculated values for the plot are mentioned below in table 4.4.

Table 4.4: Vibration attenuation values over the corresponding distances from the pile

Distance from the pile (meters)	$g_x(m/s^2)$	$g_y(m/s^2)$	$g_z(m/s^2)$
0.01	28.94	31.41	19.62
0.25	5.71	6.19	3.87
0.5	3.97	4.31	2.69
1.0	2.73	2.96	1.85
1.5	2.16	2.35	1.46
2.0	1.82	1.97	1.23
2.5	1.58	1.71	1.07
3.0	1.40	1.516	0.95
3.5	1.25	1.36	0.85
5.0	0.96	1.04	0.65

4.4. Computed Excess Pore Pressures

As stability analysis and vibratory pile driving are two different types of calculation with the former being static calculation and pile driving being a dynamic calculation, addition of vibratory effects to the stability analysis would have been difficult and time consuming. To be able to add vibratory effects in the stability analysis, only excess pore pressures are modelled as the simultaneous and after effects which will be considered as the loading parameter of the stability analysis. In this section the GMP pore pressure model is used for the computation of the excess pore pressures generated during the vibratory pile driving.

This model is already described in the chapter 2. The model correlates the development of excess pore pressure during undrained cyclic loading to the energy dissipation during cyclic loading. In Green & Mitchell (2004) an overview of the different formulas is given. In TRILDENS3 the expression of Mitchell is used (Meijers 2007):

$$r_u = \sqrt{\frac{E_{dis}}{PEC}} \tag{4.4}$$

$$E_{dis} = (\sigma'_v d\epsilon_v + 2\sigma'_h d\epsilon_h + \tau_{vh} d\gamma_{vh} + \tau_{hv} d\gamma_{hv}) \frac{1}{\sigma'_0} \tag{4.5}$$

with:

- r_u : Ratio of excess pore pressures to initial effective stresses [-]
- E_{dis} : dissipated energy
- PEC : Pseudo Energy Capacity, an empirical calibration parameter which varies from soil to soil

Given the complexity around using the above mentioned equation 4.5, for the computation of dissipated energy equation 2.42 is used which is more simpler when it comes to a large number of loading cycles.

4.4.1. Calculation

Fundamental concepts and published data shows that shear strain is the primary factor causing compaction of granular material and compaction increases with shear strain amplitude (Massarsch 2000). Based on the shear strain level generated by ground vibrations, it is possible to determine a range of critical vibrations levels. The shear strain level γ can be determined if the vibration amplitude (particle velocity) v and the shear wave velocity c_s are known using the equation mentioned below (Massarsch 2004):

$$\gamma = \frac{v}{c_s} \tag{4.6}$$

The threshold strain γ_t is defined as the value of cyclic shear strain such that the cyclic shear strains less than γ_t will not cause any densification of dry granular soils, or any pore pressure build-up in saturated granular soil. It was suggested that for most sands, the threshold strain γ_t is about 0.01% (Ramli Mohamad 1987).The accumulated the strain from the pile driving during the total duration of pile driving does surpass the threshold strain γ_t value i.e there is generation of excess pore pressure. Given, we have velocity data in all the three axes, for equation 4.6 we will use peak particle velocity (PPV) calculated by:

$$PPV = \sqrt{v_x^2 + v_y^2 + v_z^2} \tag{4.7}$$

For the shear wave velocity there are two ways of determining the value, either using a value for a type of soil directly from the work of Massarsch (2004) or calculating it from the known soil parameters:

$$c_s = \sqrt{\frac{G}{\rho}} = \sqrt{\frac{E}{2\rho(1-\nu)}} \tag{4.8}$$

Having calculated the shear strain using the equation 4.8, shear stress was calculated using the relation with shear modulus in that particular soil layer. After determining the parameters used for the energy dissipation equation, energy dissipation for every 38 cycles were calculated throughout the total time duration of pile driving. Even if the equation 2.43 is for energy dissipation per load cycle, the same equation will be used for this case as well. This is because usually energy dissipation equation 2.43 is integrated over the number of cycles and in this case of calandkanaal we have accumulated stress and strain data for every second of driving which means every 38 cycles of loading.

4.4.2. Results

Excess Pore Pressures

In figure 4.11, 4.12, 4.13 and 4.14 the computed excess pore pressures are plotted against the total pile driving time of 2075 seconds. In the figure (4.11, 4.12, 4.13) a similar step wise trend can be seen. The reason a step wise trend was obtained because of certain time intervals when the pile tip was moving. In these time intervals there was rapid excess pore pressure generation compared to other time intervals, where there is low rate of excess pore pressure generation. As expected the r_u values in the range of 580-700 seconds and 1100-1200 seconds are higher for sensor 1 as compared to the sensor 2 as at these moments the pile tip location is at a closer vicinity to sensor 1. The pile tip location information can be seen in the figure 4.9.

r_u values for all the sensors at the end of pile driving (for total duration of pile driving) is shown below:

- $r_{u_1} = 0.541$ [-]
- $r_{u_2} = 0.568$ [-]
- $r_{u_3} = 0.653$ [-]
- $r_{u_4} = 0.000232$ [-]

All the sensors have similar trend of excess pore pressure generation apart from sensor 3 and 4. In the plot, there are two types of data which are excess pore pressure generated during the total duration of pile driving and also during when the pile tip is moving. Two data points are used in order to visualise the difference in rapid generation of excess pore pressures during the movement of the pile and a constant generation of excess pore pressures, when the pile is stationary but still under vibratory loading. As seen earlier on this chapter, sensor 2 and 3 yet again show different values even if they were placed at the same depth and same radial distance from the pile. Sensor 3 seemed to show a bit higher values when figure 4.12 and 4.14 are compared. It was already suspected that the sensor 3 showed slightly higher value but it was not disregarded while conducting the post-processing on the collected sensor data (de Nijs 2019). Due to the higher values of sensor 3 the excess pore pressure generation is more linear compared to sensor 2, that's why we see a linear trend along with

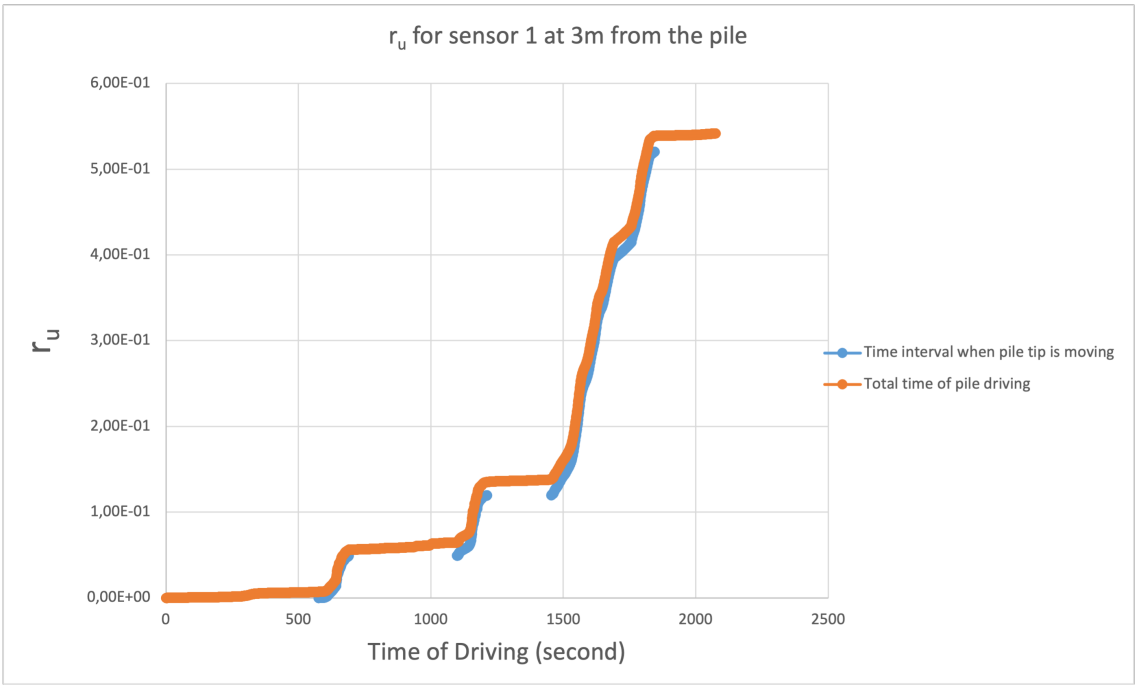

Figure 4.11: Computed excess pore pressure from sensor 1, -11mNAP

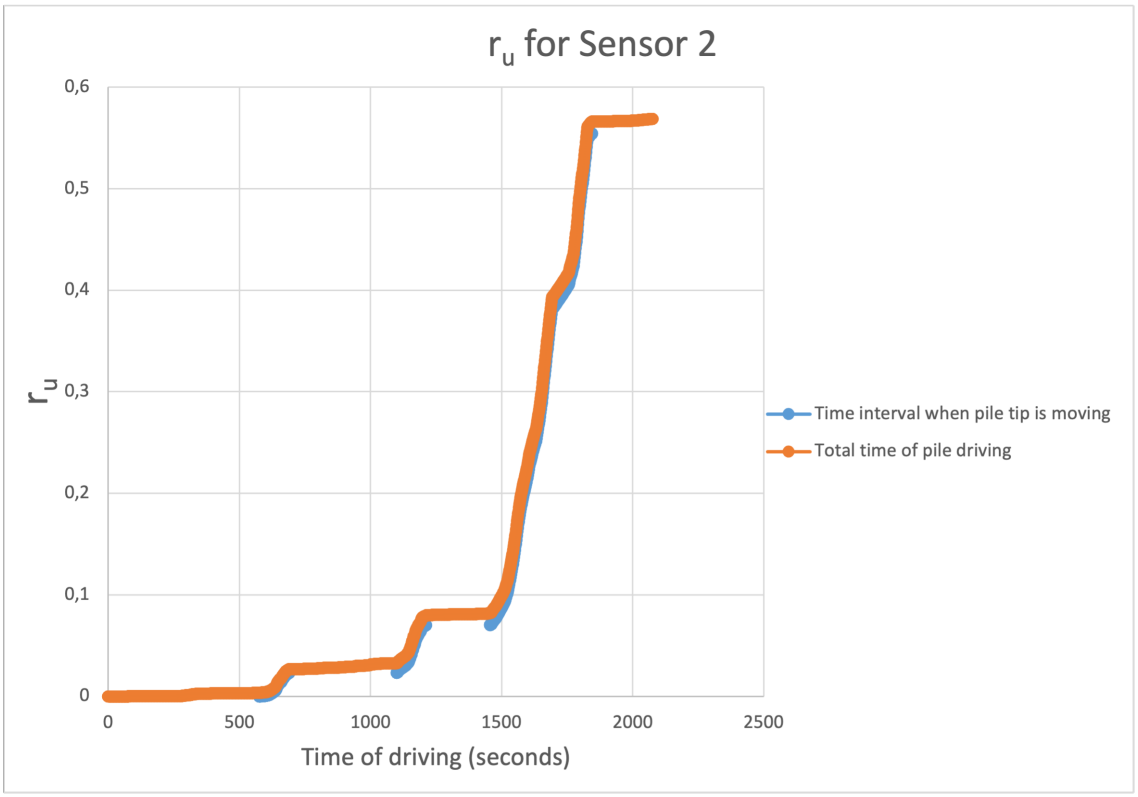

Figure 4.12: Computed excess pore pressure from sensor 2, -14mNAP

the step-wise trend discussed earlier. In the case of sensor 4, the most rapid generation of excess pore pressures is when the pile tip location is closer to the location of the sensor at -17mNAP and during the other hammer activity intervals the sensor shows inconsistent readings and in a low range leading to not considering the r_u values from sensor 4. This could be due to the fact when a pile is at a

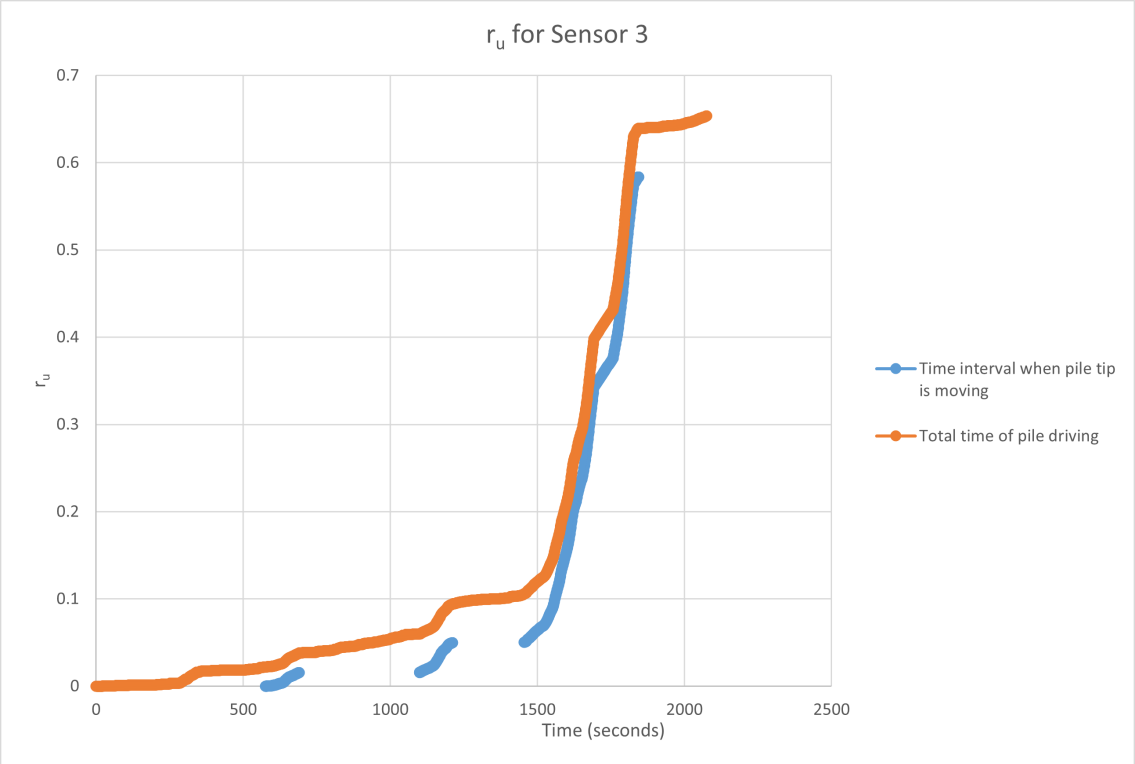

Figure 4.13: Computed excess pore pressure from sensor 3, -14mNAP

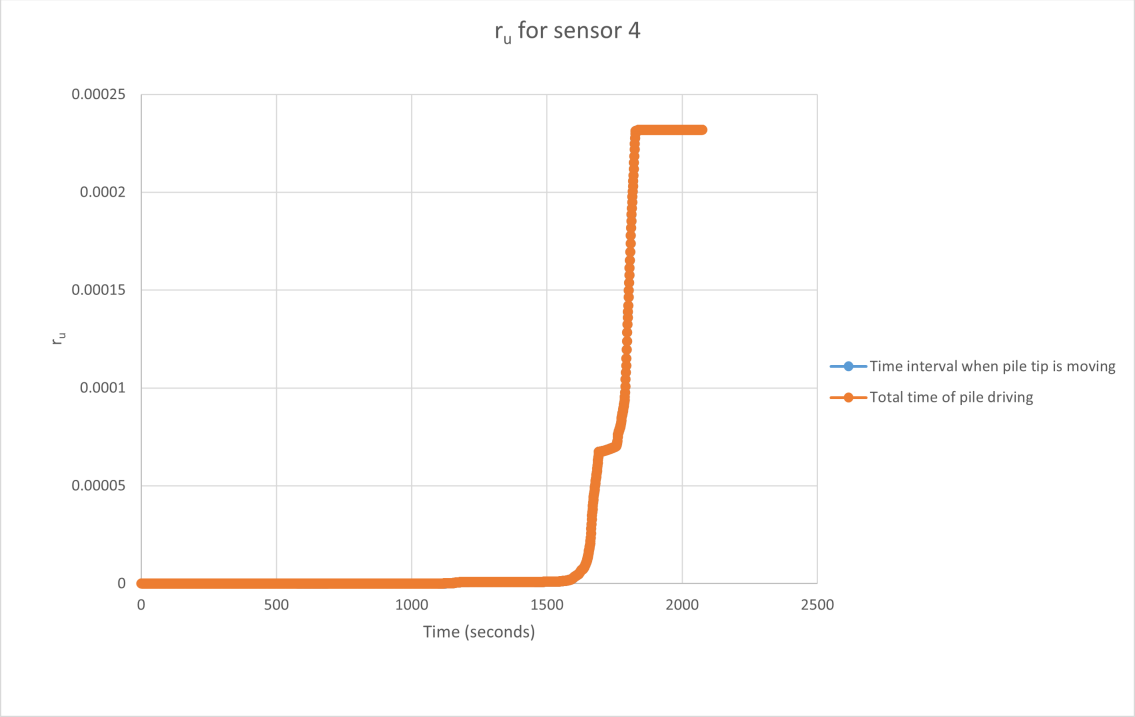

Figure 4.14: Computed excess pore pressure from sensor 4, -17mNAP

location closer to, say -11mNAP or -14mNAP there is not much vibrations or effects of vibrations at -17mNAP. The higher values of excess pore pressure in sensor 2 compared to sensor 1 is due to the fact that sensor 2 and 3 are placed in a thin 1.2m thick layer of clay and due to the permeability of the clay, more excess pore pressure is seemed to be present at this depth.

4.5. Dissipation model

From the figure 4.11, 4.12, 4.13 and 4.14 we can see the generation of pore pressures during the pile driving and from literature (LO & STERMAC 1965), it has been suggested that there is also some pore pressure dissipation involved, most of which occurs radially around the pile as suggested by Randolph & Wroth (1979). This leads to the fact that, the computed excess pore pressures in the previous section could be an over-estimated value when the total duration of pile driving is considered. So, in this section the dissipation model used to tackle this over-estimation is explained. This dissipation model is suggested by Chian (2015) in his paper "Empirical Excess Pore Pressure Dissipation Model for Liquefiable Sands".

The excess pore pressure time history can be expressed as function of depth and time as shown below:

$$\bar{u}(x,t) = (c_1 \sin \alpha x + c_2 \cos \alpha x).e^{(-\alpha^2 C_v t)} \tag{4.9}$$

where c_1, c_2 and α are constants, x is the ratio of a specific soil depth and the height of the entire soil stratum. The equation has to satisfy the following two boundary conditions:

$$\bar{u}(0,t) = 0 \tag{4.10}$$

$$\bar{u}(x,0) = x.u_i \tag{4.11}$$

where u_i is the initial effective overburden stress $(= \gamma' z)$ and the equation 4.9 is simplified to:

$$\bar{u}(t) = e^{-\alpha^2 C_v t} = e^{-At} \tag{4.12}$$

where A is a constant. It can be seen that due to the boundary conditions in the equations 4.10 and 4.11 the simplified equation 4.12 no longer has a depth variable. This implies that the excess pore pressure dissipation time history follows an exponential decay function and is independent of depth. To determine the value of constant A, a fitting analysis was made in the work of Chian (2015). Data from all the centrifuge tests were used to fit the curve shown in the figure below, where the constant A is plotted with respect to hydraulic conductivity of the soil. As shown in the figure it is evident that constant A can be linearly correlated to hydraulic conductivity, as a higher sand permeability would allow rapid pore pressures dissipation and a steeper exponential curve.

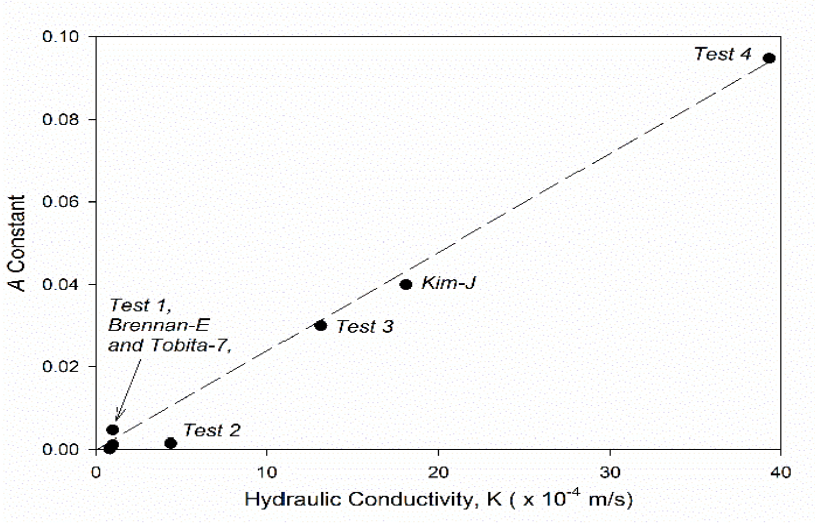

Figure 4.15: Relationship of Constant A with the hydraulic conductivity of sand Chian (2015)

In addition, the constant A has a coefficient of consolidation (C_v) component which is influenced by the hydraulic conductivity of the soil as shown in chapter 2 (equation 2.43 and 2.44). The strong linearity relationship between the constant A and the hydraulic conductivity of the sand is the reason for the choice the model for the prediction of the pore pressure dissipation.

Soil at the sensor 1 layer, it is a clean sand with properties mentioned in the section 6.2. The hydraulic conductivity assumed for this type of sand is "$7 * 10^{-4} m/s$". Using this hydraulic conductivity and using the curve from figure 4.15 the value of constant A is determined to be 0.021. Equation 4.12 shows the rate of dissipation but not the actual pore pressure at a certain time, so a constant is multiplied with the equation 4.12 which gives the pore pressure value.

$$\tilde{u}(t) = P(e^{-At}) \tag{4.13}$$

where, P is the peak pore pressure reached in the given duration of pile driving. In this case for sensor 1, the peak pore pressure that was generated using the GMP pore pressure model is $r_u = 0.0490$ for the first 2 minutes of hammer activity. Using the equation 4.13 the pore pressure dissipation curve was determined at $-11mNAP$ which is shown in the figure below:

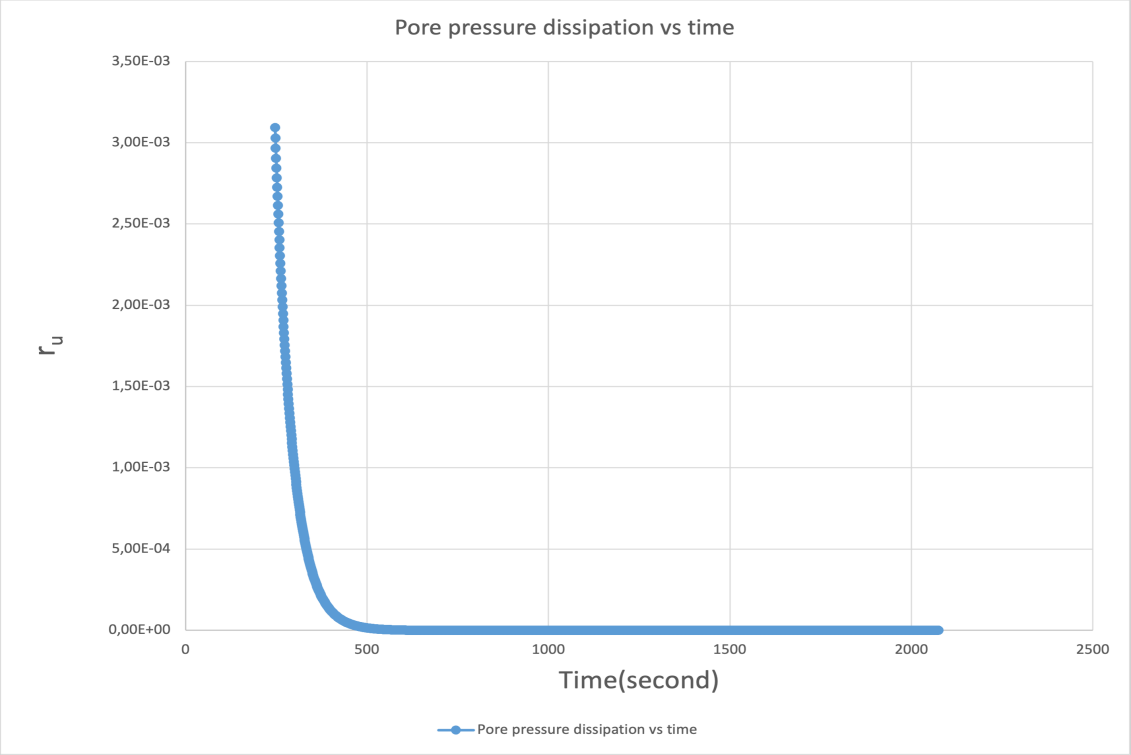

Figure 4.16: Rate of dissipation of pore pressures using the S.C Chian model

Figure 4.16 shows the rate of pore pressure dissipation (in terms of r_u) as a function of time of pile driving. Considering excess pore pressures reduce to zero within a few hundred seconds of dissipation, a new continuous generation and dissipation curve was plotted in figure 4.17 for the whole duration of pile driving. To able to plot that peak excess pore pressures will be used to evaluate the dissipation after each and every hammer activity time interval. This new r_u value will be used as the input parameter for the Bornitz equation attenuation and the D stability 2D analysis.

Figure 4.17 shows generation and dissipation plot from the sensor 1 data, placed at 3 meters from the pile. In figure 4.17, the exponential decrease curve shows the dissipation of pore pressures when there is no hammer activity and the sudden increase in pore pressure values shows the generation of pore pressures during hammer activity. The time period between 700-1100, 1215-1460 and 1845-2075 seconds are the no hammer activity time intervals as the pile tip location was constant. So at these three time intervals the dissipation model was used to plot dissipation curve. And during hammer activity time interval, generation model was used to model the excess pore pressure generation during pile driving. When considering both generation and dissipation of excess pore pressures at the end of total pile driving duration of 2075 seconds of pile driving, excess pore pressures are at an value of $r_u = 0.003$.

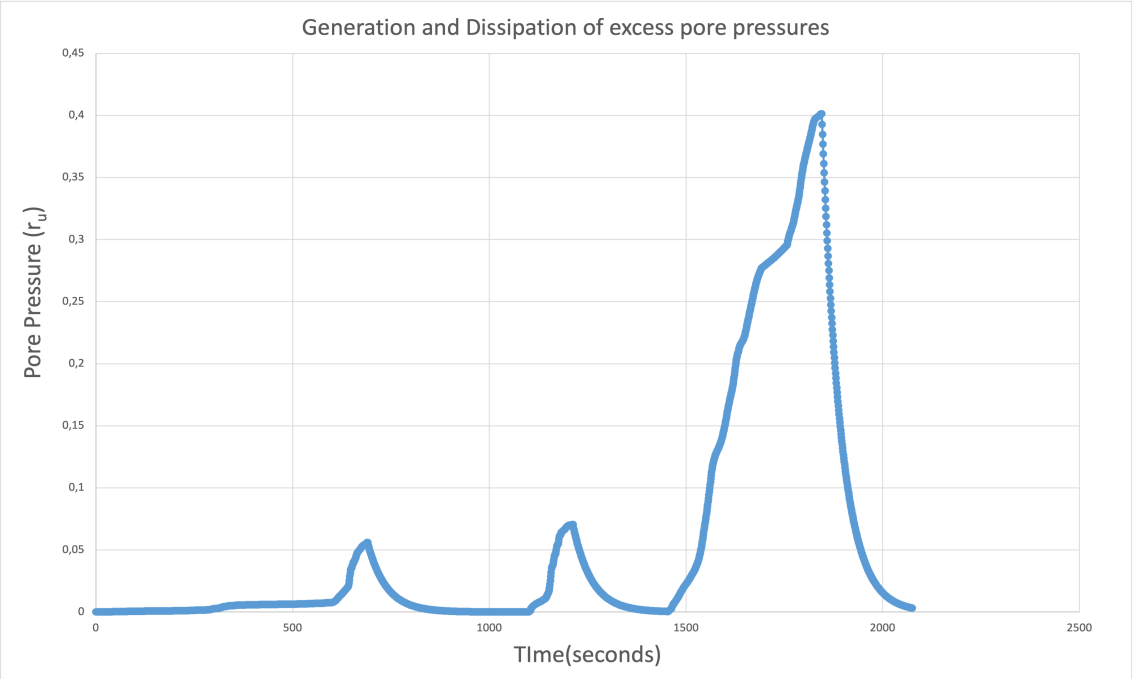

Figure 4.17: Generation and dissipation of pore pressures during whole duration of pile driving

4.6. Excess pore pressure with respect to radial distance

To determine the extent of the pore pressures effects, equation 4.2 was used to plot r_u versus radial distance from the pile location. For reference, $r_u = 0.401$ value at the end of final hammer activity is taken into consideration for the following plot. As $r_u = 0.401$ is the highest attained excess pore pressure in the entire duration of the pile driving, it will provide a brief idea of the liquefied zone around the pile.

Table 4.5: Absolute r_u values for respective radial distances from the pile

Radial distance from the pile(meters)	r_u
0.5	1.141
1.0	0.783
1.5	0.620
2.0	0.521
2.5	0.452
3.0	0.401
3.5	0.360
5.0	0.275

From figure 4.18 an exponential decrease of the accumulated r_u over the radial distance from the pile can be seen, as in the work of Robbin (2020).The exponential curve equation obtained from this analysis:

$$y = 1.0413e^{-0.29x} \tag{4.14}$$

where y is the ratio of excess pore pressures to initial effective stresses and x represents the radial distance from the pile. Looking at the figure 4.18, it can be seen that within 0.85 meters radially from the skin of the pile $r_u > 1$. This means with considering both generation and dissipation of excess pore pressures, the liquefied zone around the pile is about 0.85 meters radially from the pile. Similarly, a liquefied zone of 1 meter was seen in a similar project in Amsterdam concerned with sheet pile walls (A B Arun Kumar 2020).

While the computed excess pore pressures did give a rough idea about the trend of excess pore

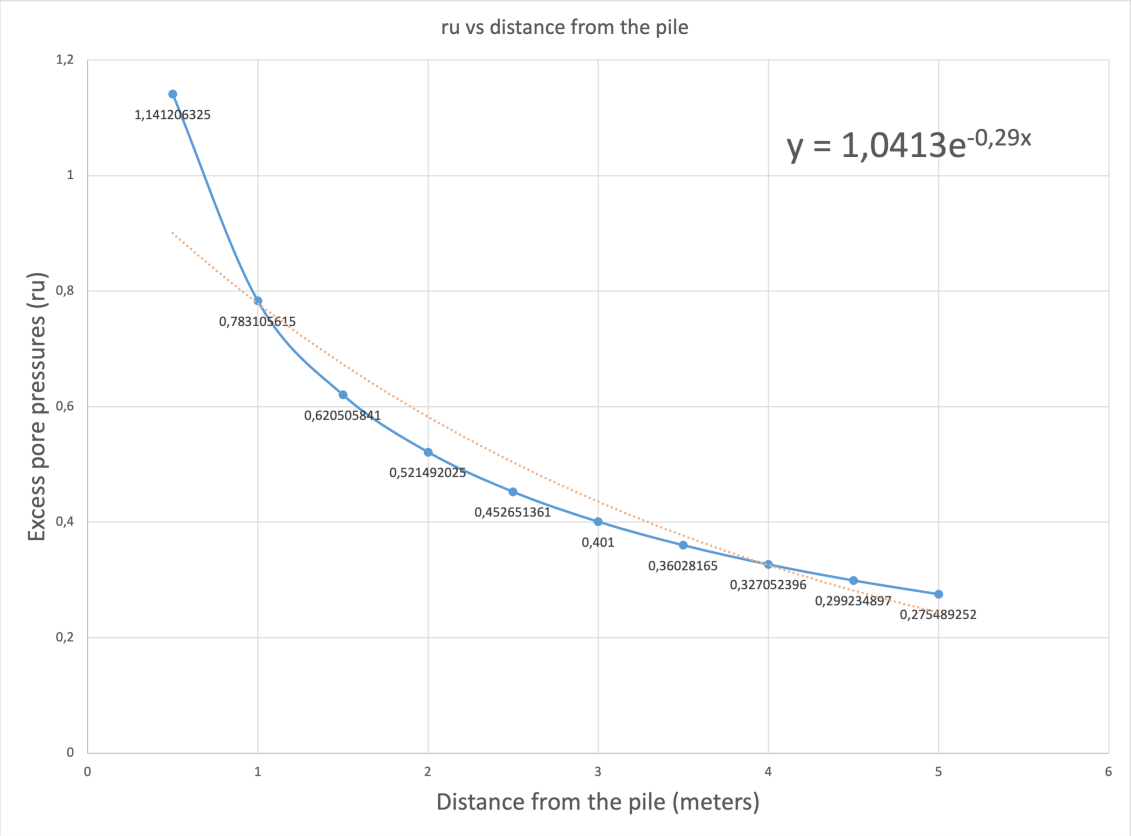

Figure 4.18: Computed excess pore pressure, at the end of pile driving with respect to the radial distance from the pile for sensor 1, -11mNAP

pressure generation and zone of degradation around the pile location, there was no way to validate the computed pore pressure data. Due to non-reliable pore pressure data from the Calandkanaal case study, the only way to validate GMP pore pressure data was to compare it with similar projects with reliable pore pressure data. One such example used for comparison is the work of Lamens (2017) on assessing liquefaction induced instability on submerged slopes. Comparing the general trend of excess pore pressures decay with respect to radial distance from the pile in equation 4.15,a very similar trend was observed from the GMP model data with occasional r_u values higher than 1.

$$r_{u,max} = 2.6e^{-0.22\frac{x}{D}} \tag{4.15}$$

where, x is the radial distance from the pile and D is the diameter of the pile. This average exponential trend of pore pressure decay is very similar to equation 4.14 obtained from figure 4.18, with the obvious difference of normalisation in equation 4.15. Another observation was the higher r_u values in clay when compared with r_u in sand, which explains higher r_u obtained in sensor 2 and 3 when compared to sensor 1. But in some cases there can be similar r_u values reported in both sand and clay like in the work of Hwang et al. (2001) where the sand layer was confined by two thick clay layers, which is not the case in Calandkanaal, Rotterdam.

4.7. Summary

In this chapter the data regarding the vibratory pile driving in the port of Rotterdam is introduced along with the analysis done on the data for the determination of vibration attenuation and computation of excess pore pressure generation during the pile driving. For vibration attenuation, the Bornitz equation was used. Bornitz equation was found to be satisfactory as an preliminary evaluation correlation when pile driving induced vibrations are only considered (Grizi et al. 2018). This chapter also introduces the calculations made with GMP Pore Pressure model and the vibration attenuation model to estimate the liquefied zone around the pile, which is 1 meter radially around the pile. However, if the accumulation of pore pressure is greater than 60% then it has also been equivalently compared to liquefaction as stated by Seed (1988). During the computation of excess pore pressure a few limitations were also observed namely: (a)the dependency of empirical formula of PEC value on the relative density of soil cannot be used for the case of the clay, (b) the simplified GMP model used requires stress-strain data for each and every cycle, which is not the case in this data set, (c) The damping ratio function based on TRILDENS3 gives non-zero value when strain is less than 10^{-6}, which was unexpected. Besides these limitations, a rough idea of the excess pore pressures was obtained from the vibration data which is further used for validation of the pore pressures from the PLAXIS 3D calculation.

5

3D Finite Element Modelling

In this chapter the strategy adopted and the finite element modelling are explained. For FEM calculations Plaxis 3D is adopted for its ability to determine factor of safety in 3D. This is then followed by D-Stability calculations which are performed in an attempt to understand the results obtained by the Dutch engineering firm on the Calandkanaal project.

5.1. Analysis Strategy

After going through the provided data regarding the pile driving, the methodology considered for the thesis is shown in figure 5.1 below.

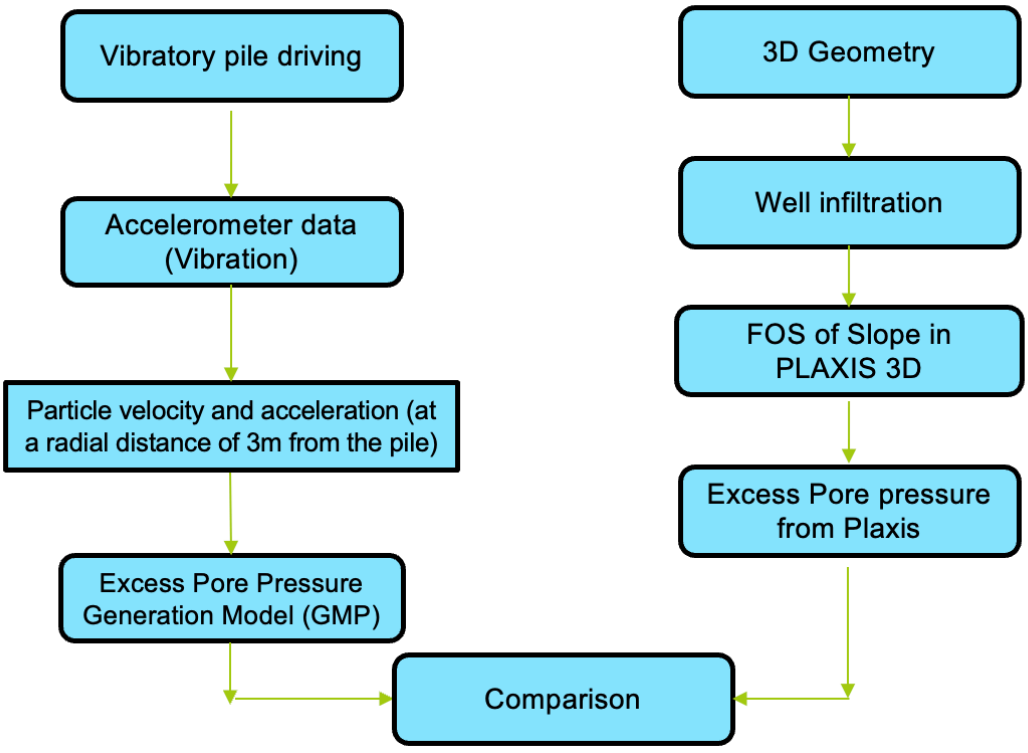

Figure 5.1: Adopted methodology for 3D stability analysis and validation of the model

Shear strain is the primary factor causing compaction of granular material and compaction increases with shear strain amplitude. Based on the provided data from calankanaal it was possible to determine

shear strain amplitude. Then GMP pore pressure model was used to generate the excess pore pressures, which are used to validate the pore pressure generated from the finite element model.

5.2. Properties of the model

The properties used for the model are shown in figure5.2:

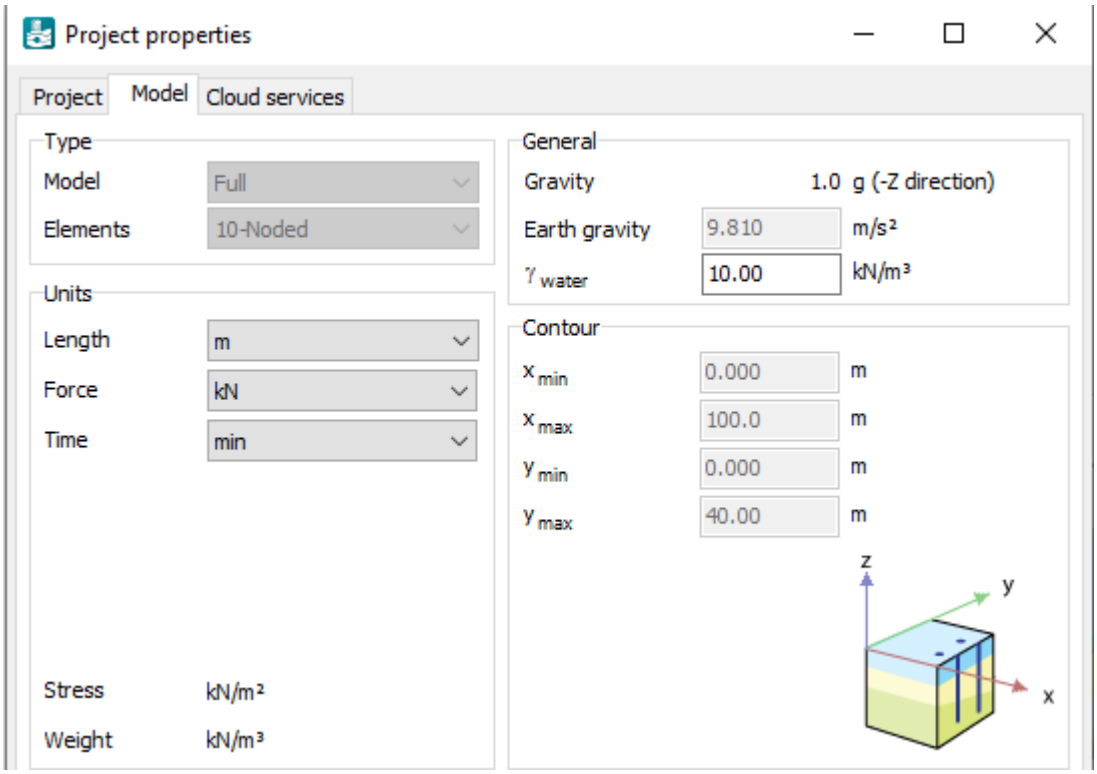

Figure 5.2: Project (Plaxis 3D) properties for the model

The value of x_{max} is chosen as 100m so that it would accommodate the complete geometry of the slope from the Calandkanal case study. The toe of the slope is at about 95m from the crest of the slope. The value of y_{max} is taken to be 40m to keep it comparable with respect to the x_{max} value as it was decided a lower value of y_{max} could lead to mimicking plane strain condition. The dimensions of the model are also governed by the fact that a much bigger geometry could lead higher calculation times. All other properties under the section ”General” and ”Units” (figure 5.2) are set to real world conditions.

5.3. Soil

The soil conditions used for the model with their respective properties.

Table 5.1: Model soil layers with their respective properties and depth

Soil Name with admixture	γ_{dry}	γ_{sat}	E[MPa]	Cohesion	ϕ'	Drainage type	Depth[mNAP]
Sand, very silty/clayey	19	21	30	-	30	Drained	+5.70 to 0.0
Sand	20	22	125	-	35	Drained	0.0 to -13.81
Clay, moderately sandy	18	18	5	-	32.5	Undrained(A)	-13.81 to -15.21
Sand, very silty/clayey	19	21	30	-	30	Drained	-15.21 to -18.81
Sand, fine and slightly silty	18	20	35	-	32.50	Drained	-18.81 to -21.21
Clay, moderately silty	18	18	3	2	27.50	Undrained	-21.21 to -22.21
Sand, coarse, slightly silty	19	21	35	-	32.50	Drained	-22.21 to -23.65

To simulate similar pile driving effects, the above mentioned soil properties were used in the geometry. While the type of soil and friction ratio of the soil was identified from the provided CPT and

borehole data (7), soil properties like unit density, cohesion etc were also required for the modelling. So, the information in table 5.1 was retrieved from the table 2b from NEN9997 (7), which gives low characteristic value of means of the concerned soil type. The groundwater head was placed at $-0.81mNAP$ as mentioned in the borehole log. Using the soil information from table 5.1, the geometry implemented for FEM is shown in figure 5.2.

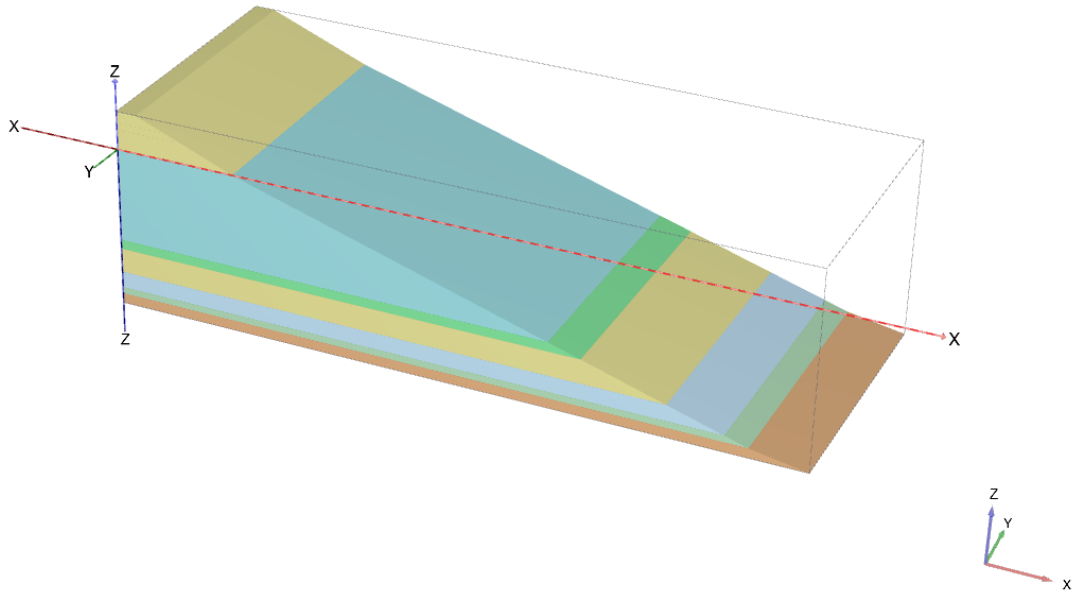

Figure 5.3: 3D visualisation of the geometry

5.4. Structure

The structure in the model is an embankment with its crest at a height of +5.70mNAP. The material set for the structure is sand which is fine and slightly silty mentioned in the soil parameters table 5.1 shown above.

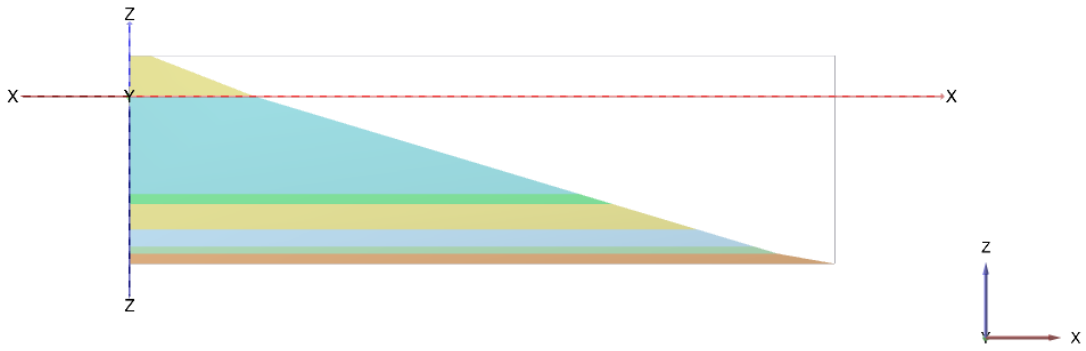

Figure 5.4: Side view of the geometry

The base length of the geometry is 97m with a total height of 29.35m (5.70mNAP to -23.65mNAP), making a slope angle of 16.70 degrees with the horizontal axis (x-axis).

5.5. Phases of construction

The whole analysis is a mixture of different analyses run in different phases of construction namely (a) Initial phase (b) Phase 1[Safety analysis] (c) Phase 2[Pore pressure] and (d) Phase 3[Safety analysis].

The first two phases, Initial and Phase 1 are pre-pile installation phases and phase 2 and 3 are post-pile installation phases. Each and every phase mentioned above are described below.

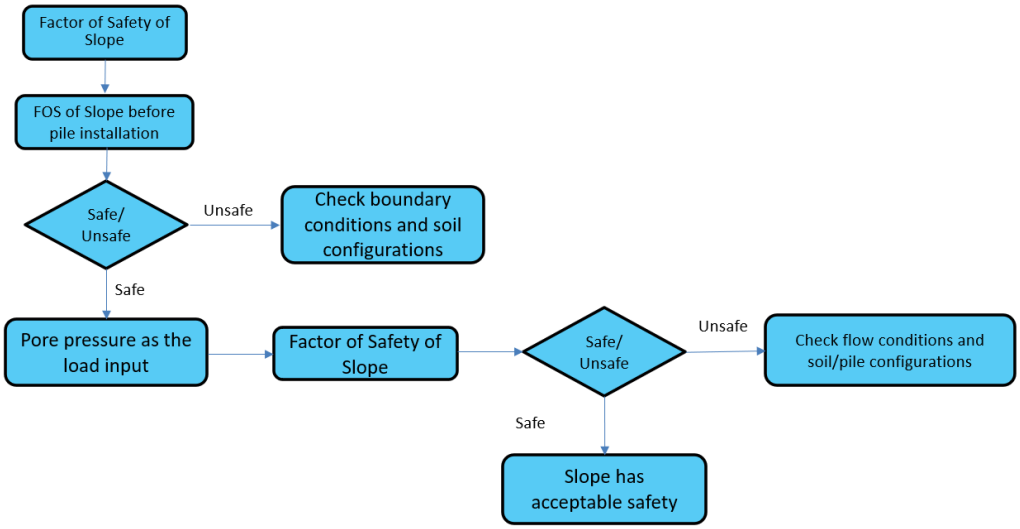

Figure 5.5: Step by step approach of stability analysis

Initial Phase

In the initial phase the calculation type is set to "$K0Procedure$". The initial water pressures are fully hydrostatic and based on a general phreatic level defined by head assigned to the borehole is used in the model. For this phase, the pore pressure calculation type is set to phreatic and the global water level is set to the borehole water level. The groundwater flow boundary conditions used for this phase are as follows:

- X_{min} is kept closed for the ground water flow on the opposite direction of the slope
- For horizontal groundwater flow to be possible X_{max}, Y_{max} and Y_{min} are kept open
- Z_{max} and Z_{min} are also kept open for vertical groundwater flow

Phase 1[Safety analysis]

In this phase the whole geometry undergoes a stability analysis to able to determine the factor of safety of the slope prior to generation of excess pore pressures. For this phase the calculation type is set to safety and the pore pressure calculations are taken from the previous phase which is the Initial phase. The loading type in this case is set to Incremental multipliers of 0.1. The groundwater flow boundary conditions are similar to the previous phase as they cannot be changed anymore in this phase.

Phase 2[Pore Pressure]

For phase 2, it is set to start from the initial phase. This phase concerns with the excess pore pressure calculation which is a direct result of pile driving. The calculation type is set to a fully coupled flow-deformation. This is a time dependent analysis of deformation and (total) pore pressures. In this phase a well is added to the geometry which will infiltrate the volume of water, displaced when a pile is driven into the geometry. The volume displaced calculation is explained down below. The well is set between $-7mNAP$ and $-10mNAP$ to mimic the excess pore pressures generated during pile driving at this depth. For covering this 3m of depth the pile took 2 minutes which is also the time set for this phase. The groundwater level is set to the borehole water level which is similar to all the phases before.

Volume displacement
The volume displaced in the soil strata during the pile driving depends on the driven pile, distance around the pile where compaction can take place, the expected compaction rate of the soil layer and the installation velocity of the pile. Based on the introduced steel volume (no plugging) of the pile and the degree of compaction, the volume of displaced pore water per meter and per minute was determined by the following equation (de Nijs 2019):

$$V_{displaced} = (V_{steel} + (V_{comp} * \%_{comp})) * v \tag{5.1}$$

where $V_{displaced}$ is the volume displaced, V_{steel} is the volume of the steel, V_{comp} is the volume over which compaction can occur, $\%_{comp}$ is the expected compaction rate of the layer and v is the installation velocity of the pile (m/min).
From the center of the open ended pile, the scope of the compaction is assumed to be 1.5 meters long. This distance is crucial for the determination of the volume over which compaction can occur. The installation velocity is assumed to be 1 m/min. Considering the diameter of the pile (1.62 m) and the wall thickness of the pile (0.02 m), the results for volume displaced are shown in the table 5.2 shown below:

Table 5.2: Volume displaced for different rate of compaction values

Rate of compaction(%)	$Vol_{disp}(m^3/min)$
2	0.243
5	0.455
8	0.667

The above mentioned rate of compaction values are chosen based on the settlement vs ground acceleration curve. The values are based on the ground accelerations and the penetration resistance. This method of assessing compaction is suggested by Massarsch (1993) and the curve used, can be seen in figure 5.6. It is an empirical graph, and based on observations during vibratory compaction.

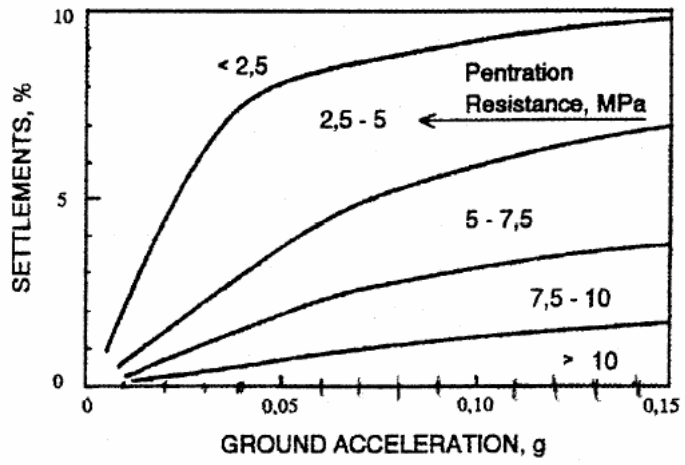

Figure 5.6: Graph for estimating compaction as a function of cone resistance and acceleration amplitude (Massarsch 1993)

For performing the volume of water calculation in Plaxis there are two ways, one performing a plastic calculation with steady state ground water flow and the second is performing a fully coupled flow deformation calculation. The problem with plastic calculation with steady state ground water flow is the model applying the volume of water for an infinite time in which case the model tends to fail. Adding the pore pressures in this case is a time sensitive step, which is not full-filled by the plastic calculation, so instead the fully coupled flow deformation is preferred as it is a time sensitive analysis.

Fully Coupled Flow Deformation
In a fully coupled flow-deformation analysis, PLAXIS will solve the full interaction between deformations, consolidation and groundwater flow simultaneously in the same phase. In this calculation, the calculation uses staged construction and transient groundwater flow combined.

Phase 3[Safety analysis, post pile installation]
Like the phase 1, phase 3 also concerns with safety analysis but safety analysis of the slope post pore pressure calculation. All the boundary conditions are set similar to the previous phases. The pore pressure calculation type is set to use the pore pressures from the previous phase to encounter the excess pore pressures infiltrated by the well in this phase.

5.6. Results

This section is dedicated to discuss the results and outcomes of the FEM. While the FEM determines the factor of safety of the slope subjected to the excess pore pressures, it is imperative to check the displacements and the deformations of the mesh of the geometry to get a brief idea of the failure mechanism in formation. The deformed mesh also gives an idea about how localised is the effects of the excess pore pressures.

Incremental Displacement
When performing a safety analysis using the Phi-C reduction method, there is introduction of out-of-balance forces in the model. This out-of-balance is solved by the calculation kernel, which results in deformations. The additional displacements generated, do not have a physical meaning but the incremental displacements in the final step do give an indication of the likely failure mechanism.

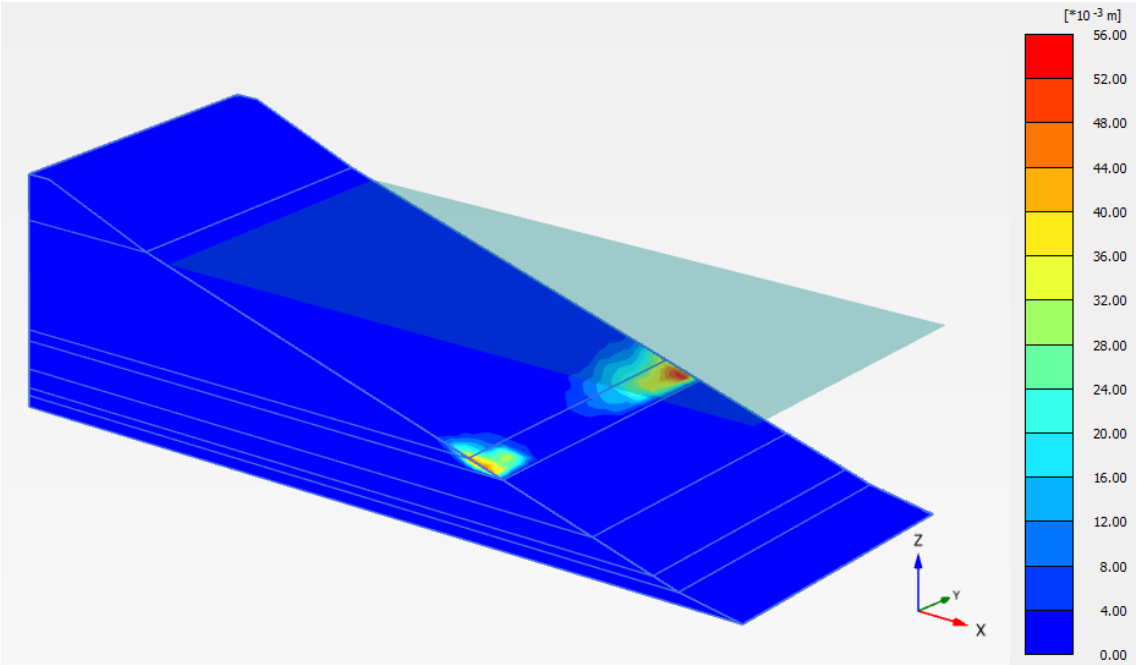

Figure 5.7: Incremental displacement at the end of stability analysis 1

In the figure 5.7, the incremental displacement for the whole geometry, at the end of the Phase 1 is shown. In the right side of the figure the scale of the displacement is shown in terms of colour coding. The incremental displacement are in the range of 2 to 5.42 cm at the end of the 2nd layer of the geometry, which is the beginning of the clay layer at -13.81mNAP. Because of this displacement at -13.81mNAP, there is no visible effect on the crest of the slope. Since it is a meter deep clay layer, displacements are expected here as the pore pressures cannot escape clay due to its permeability and this causes the clay layer to displace.

Next in figure 5.8, the deformations at the end of phase 2 (pore pressure calculation) are at a much lower range as compared to the deformations at the end of the Phase 1. As expected the maximum deformations during and after this phase of calculation is visualised at the vicinity of the well. The maximum incremental displacement at this point is 0.21cm. Along with that, there is some displacement in the the range of $0.06 - 0.08$cm in the sand layer from 0.0mNAP to -13mNAP. At the top of the slope, an incremental displacement of 0.1cm is also visualised at the end of the pore pressure calculations. In

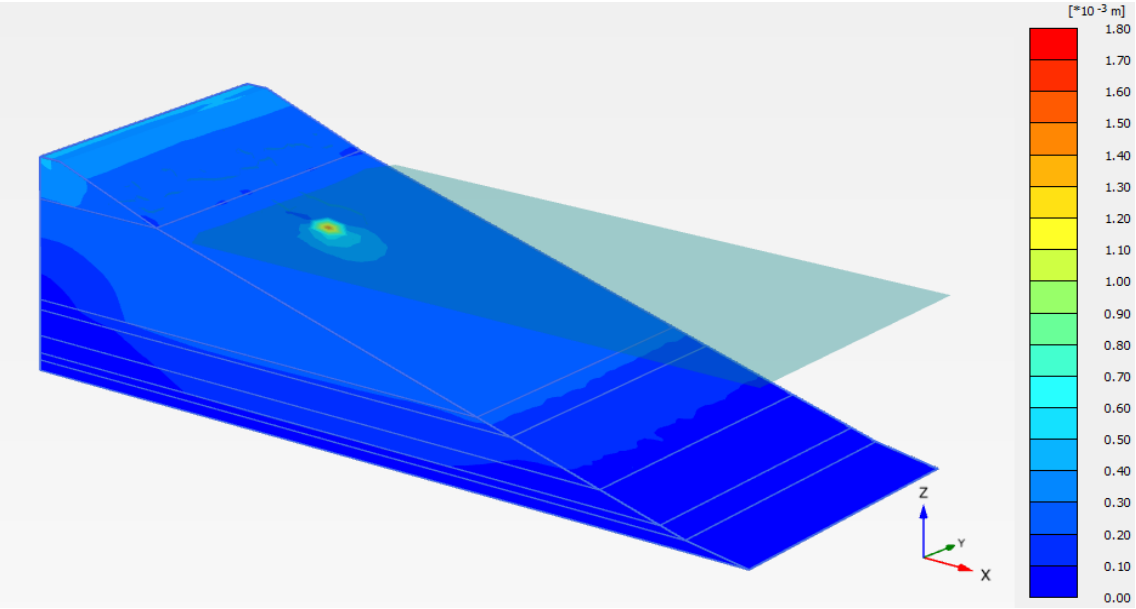

Figure 5.8: Incremental displacement at the end of Phase 2

terms of deformed mesh and maximum deformations, for the phase 2 it was at a higher height than the placement of the well in the sand layer as it can be seen in the figure 5.9. From figure 5.9, the deformed mesh can be seen around the location of the well from $-7mNAP$ to $-10mNAP$. These deformations are caused in the phase 2, pore pressure calculation when couple flow deformation calculation is run.

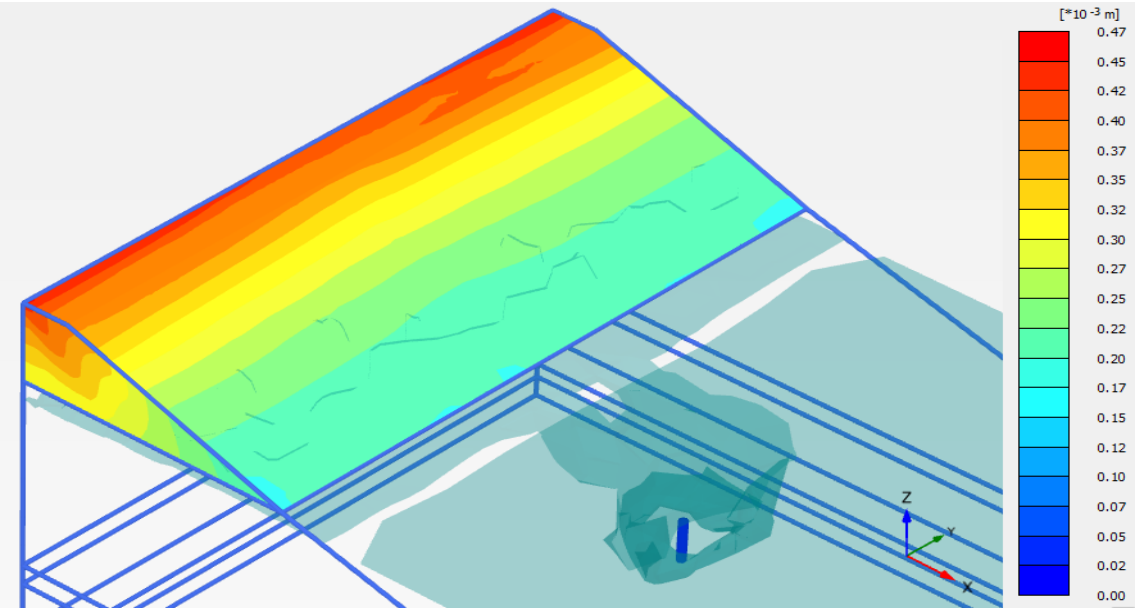

Figure 5.9: Deformed mesh at the end of the Phase 2 calculation

From figure 5.10 a similar trend of incremental displacements can be seen when compared to phase 1 stability analysis. One of the few differences when compared to the phase 1 stability analysis is the maximum displacement near the location of the well and also at the toe of the slope closer to the boundaries of the model. The maximum incremental displacement at the end of the stability analysis is 9.1cm which can be seen near the boundary of the geometry. To see if this effect persists if the boundary of the geometry is extended, a similar model was was developed with similar properties except a larger range between y_{min} and y_{max} of 60 meters. Still the a similar type deformations were noticed.

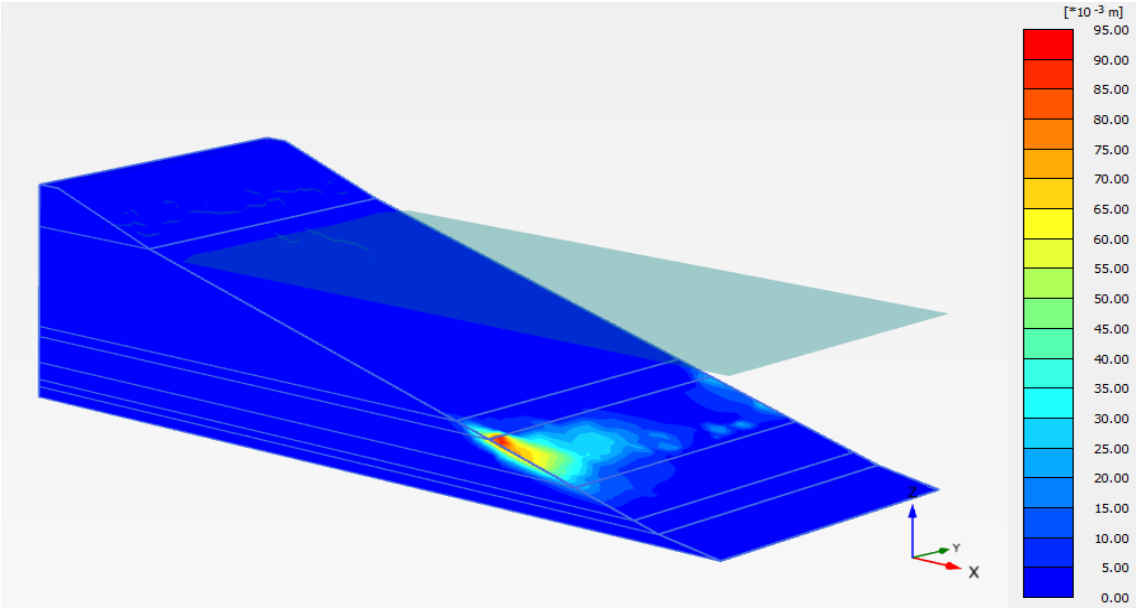

Figure 5.10: Incremental displacement at the end of Phase 3

In figure 5.11, the failure surface after the slope stability analysis 2 can be observed. The deformation shown in blue in the middle of the slope shows the deformations caused due to the well infiltration. The location of the well is (27.0, -7.0) when seen in 2D. The slip circle can be seen forming near the toe of the slope which is completely under water. This unexpected formation of slip circle could be due to the water loads from the phreatic level on the moderately sandy clay layer and sand (very silty/clayey) layer. These observations in figure 5.9 and 5.11 shows the instant deformation in the mesh are localised near the well and also due to low permeability of the clay layer at the depth of 15.21mNAP, maximum displacements are recorded at this depth.

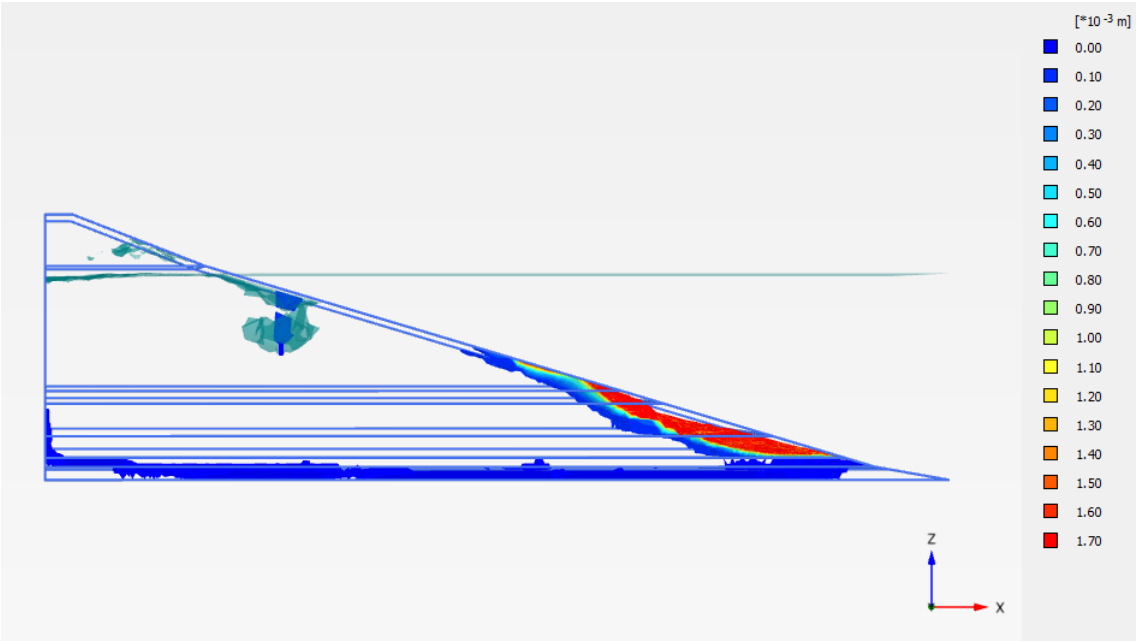

Figure 5.11: Failure Surface after Phase 3

Factor of Safety
Moving on to the main objective of the thesis, determination of the factor of safety in 3D. The factor of safety was calculated in two different stages, first the factor of safety for pre-pile installation on the slope and second, factor of safety after the pile installation effects have been accounted for in the slope. The only pile installation effect accounted for is the generation of excess pore pressures during vibratory pile driving.
As expected and also seen in literature, the factor of safety from both the stability analysis are different, with the factor of safety for pre-pile installation phase being higher than the post-pile installation effects phase.

Table 5.3: Factor of safety of the slope at phase 1 and phase 3

Phase 1 FOS	Phase 3 FOS
1.538	1.084

Table 5.3 shows the factor of safety of slope being higher than 1 there was no failure detected in the model. In order to verify if the model was producing consistent results, changes were made to global coarseness factor and see the difference in the results in terms of factor of safety, shown in table 5.4.

Table 5.4: Different factor of safety with respect to different mesh coarseness factor

Global Scale factor	Phase 1 FOS	Phase 3 FOS
0.7	1.55	1.06
0.6	1.511	1.10
0.5	1.538	1.084
0.4	1.54	1.070
0.3	1.532	1.036

After running the model with different mesh sizes, the difference in the factor of safety seems to be very low and the factor of safety seems to be in a constant range of 1.5 to 1.55 for the phase 1 stability analysis and 1.04 to 1.10 for the phase 3 stability analysis. Multiple simulations were run in order to check if the model was producing consistent results, which were found to be optimum. If a pile were to be modelled and after the pile is driven into the slope followed by the dissipation of excess pore pressures, the factor of safety of the slope would have been higher than the phase 3 factor of safety shown in table 5.4.

5.7. 2D slope stability

In an attempt to learn more about the stability of the slope, the same geometry is analysed in D-series stability software. This analysis explains the work done in the article of de Nijs (2019) and gives a different perspective in terms of factor of safety and failure surface. For geometry of the D-Geo stability, same properties were used to the ines used in Plaxis 3D explained in section 5.3. The total base length of the slope was 100 meters and a total height of 29.35 meters extending from 5.70mNAP to -23.65mNAP. The geometry can be seen in the figure 5.12.

The slip circle definitions used in the model are as follows:

- Grid: an area of 57m*20m was allocated for the center of the slip circle with 400 points in the area, depicted by cross-dots in the figure 5.12
- Tangent line: For the line which will be acting as tangents to the slip circle, 20 lines were used from the depth -1m to -20m which are depicted by green lines in figure 5.12

For the 2D calculation, the Bishop's method of slices (Reinius 1955) is used which is explained in section 3.8 of chapter 3. From this analysis, the minimum factor of safety obtained was used for comparison with the Plaxis 3D analysis.

Looking at the 2D analysis result from the table 5.5 2D factor of safety is more than the 3D factor of safety. The difference between the results of the both 2D and 3D analysis is about 6.7%. But this

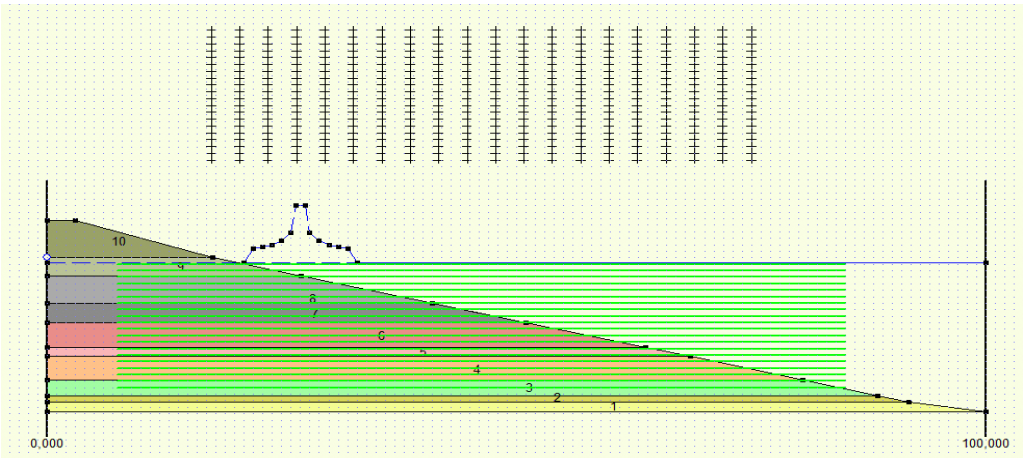

Figure 5.12: Geometry in the D-Geo-Stability

Table 5.5: Factor of safety in 2D and 3D for the pre-pile installation phase

FOS 2D analysis	FOS 3D analysis
1.65	1.538

difference does not mean anything as both of the analysis used are different from each other by types of calculation method and types input method used for excess pore pressures. So, the only focus is on the failure mechanism of both the analysis.

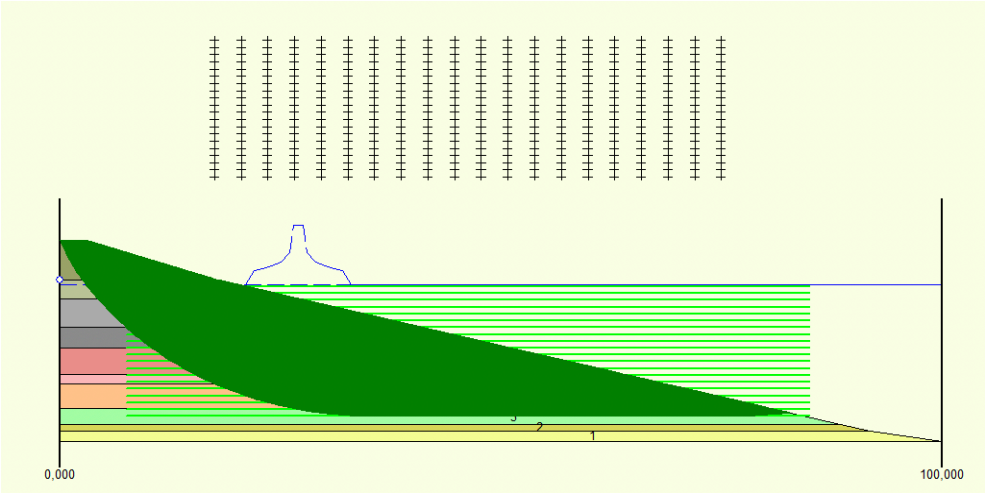

Figure 5.13: D-Geo stability safety overview

In figure 5.12, the green coloured safety overview depicts higher than 1.5 factor of safety. How the safety overview curves down the slope completely depends on depth of the tangent lines used for the definition of the slip circle. Figure 5.14 shows the critical surface formed at the crest of the embankment in the stability analysis. Similarly in the Plaxis 3D calculation, in phase 1 stability analysis minor displacements were observed at the crest of the embankment as mentioned in incremental displacements in section 5.6. But in Plxis 3D major displacements were observed at the clay layer at -13.81mNAP, which was not the case in this 2D analysis.
In order to compare with post pore pressure stability analysis conducted in Plaxis 3D, a similar stability analysis was also conducted in D-Geo stability. In order to add excess pore pressures in D-Geo stability, GMP model excess pore pressure values were used as head value and added in form of a new phreatic line as shown in figure 5.12. The head values used in the new phreatic lines are shown in table 5.6. The location of the pile was assumed to be (27.0m, -7.0m) in D-Geo stability.

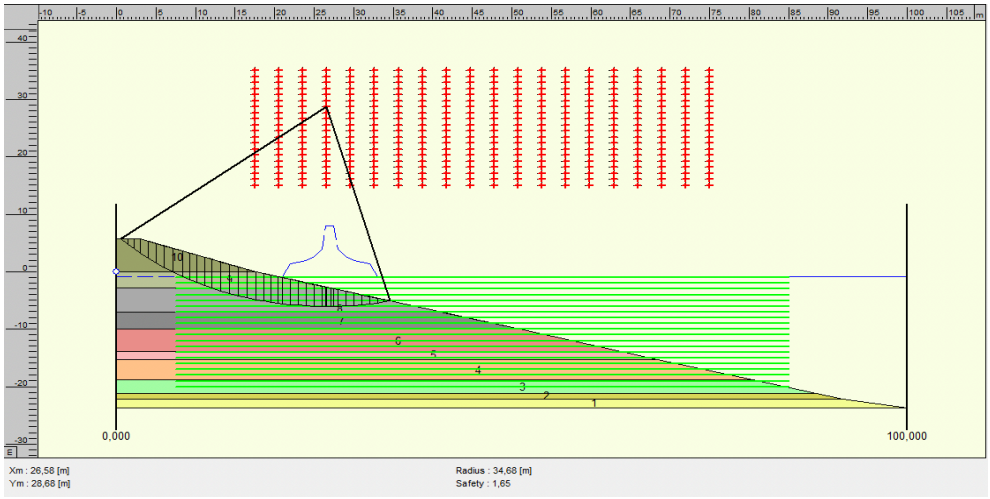

Figure 5.14: Critical surface in the initial stability analysis

Table 5.6: Head values with respect to radial distance from the location of the pile

Radial Distance (m)	Head (m)
0.5	7.0
1.0	4.0
2.0	2.6
3.0	2.0
4.0	1.63
5.0	1.37

The new phreatic line was also set to different layer. In layer 6 (sand), subdivisions were made by making more layers out of it in order to localise the effect of the new head value. This step is explained in the figure 5.15. The new head values were more focused on the critical surface of the previous calculation shown in figure 5.14 to show the effects of the pore pressure on the slope.

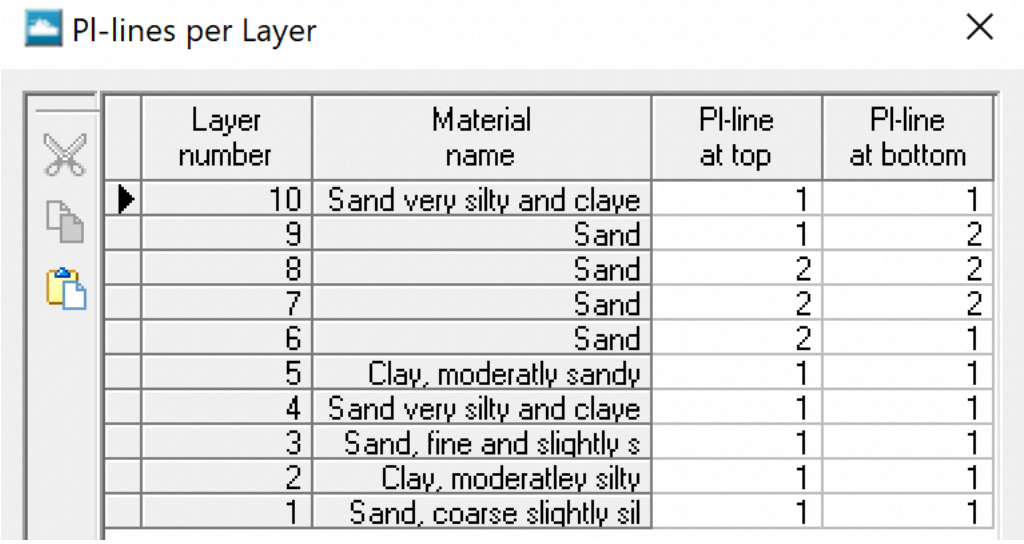

Figure 5.15: Phreatic line per layer

After the stability analysis, the factor of safety obtained from D-Geo stability is summed up in table 5.7. The reduction in the factor of safety shows that the 2D model is working as expected.

Table 5.7: The factor of safety determined by D-Geo stability

FOS, pre excess pore pressure	FOS, post excess pore pressure
1.65	1.48

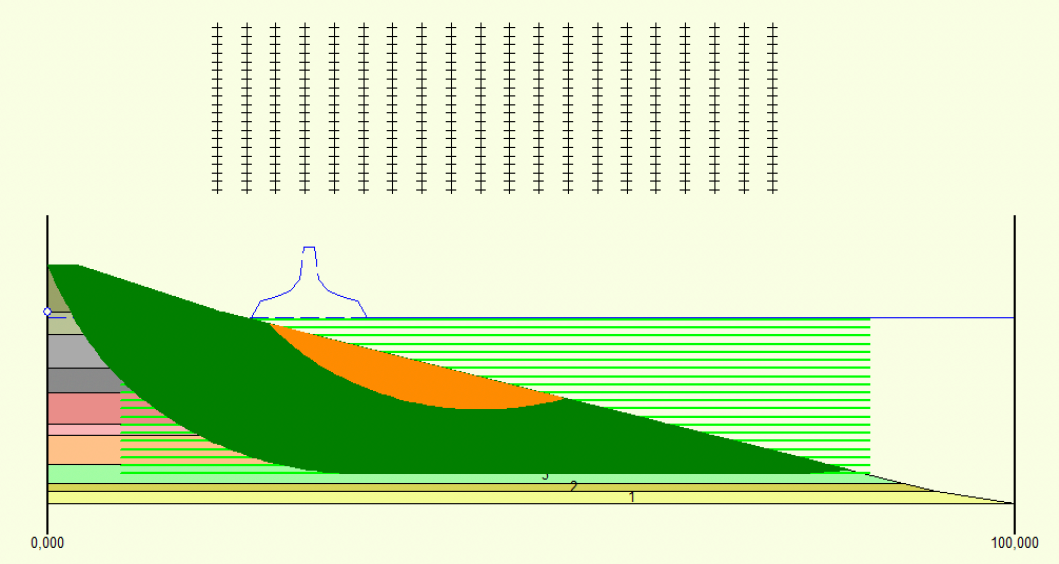

Figure 5.16: Safety overview after addition of pore pressures

Comparing figure 5.14 and figure 5.17, the shift in the critical surface from near the crest of the embankment to middle of the slope can be clearly seen. This is due to the added pore pressures on the initial critical surface. A very similar shift of critical surface was also seen in the Plaxis 3D analysis when the figure 5.11 is taken into consideration. Figure 5.16 shows the safety overview of the slope after the post pore pressures stability analysis. The orange colour depicts the part of the slope which has a lower than 1.5 factor of safety and also the critical surface on the slope. The critical surface of the slope is also very close to the location of the hypothetical pile driven similar to the phase 3 result in the Plaxis 3D simulation with the obvious difference of distance of the critical surface from the location of the pile.

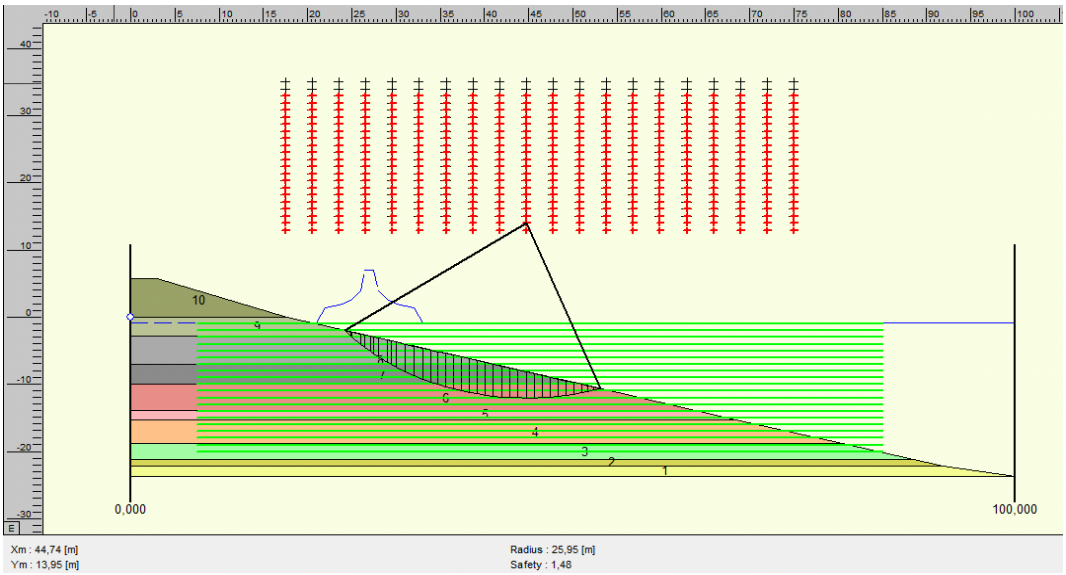

Figure 5.17: Critical surface after the addition of pore pressures

The 2D stability analysis in D-series gives an idea about the failure surface formation due to the added excess pore pressures but it fails to determine the area effected because of plain strain constraint. To be able to tackle this problem Plaxis 3D modelling was adopted. Difference is not only in the types of analysis but also in pore pressure input methods. While D-stability relies on adding excess pore pressures in terms of new phreatic line, in Plaxis 3D the pore pressures have been added through well infiltration method. The addition of a new phreatic line is based on the computed excess pore pressures data, which is the GMP model data in this case and is very similar to the original case study. But in case of Plaxis 3D, well infiltration method could provide an overestimated excess pore pressures into the geometry. This is because the well infiltration method infiltrates the volume continuously for the mentioned time which is different to volume displaced by pile in that exact amount of time. Volume displaced caused by pile driving is gradual along the depth where as well infiltration is a continuous flow along the whole depth.

5.8. Summary

This chapter introduces the simulations performed in the finite element model, Plaxis 3D and the steps taken to determine the factor of safety of the slope in 3D. The slope in the FEM model had a factor of safety of 1.538 and 1.084 before and after the addition of excess pore pressures respectively and was considered safe as there was no major failure. In an attempt to validate Plaxis 3D model a 2D model was developed in D-Geo stability and comparisons were made accordingly. From the comparisons it was clear that the 2D-Geo stability analysis had more differences than similarities so, a Plaxis 2D model was developed and comparisons are made in the next chapter. Along with the determination of the factor of safety, Plaxis 3D was also used to validate the computed excess pore pressures generated by the GMP model which is also explained in the next chapter. This whole chapter also shed some light on the approach that was adapted for fulfilling the objectives of the thesis.

6

Discussion

After performing both the 2D analysis and 3D analysis, it was observed that both of the analysis differ a lot in terms of factor of safety and type of analysis done as the D-stability uses Bishop's method of slices and Plaxis 3D uses the phi-c reduction method. So in order to validate the results and behaviour of the 3D model, Plaxis 2D analysis with the same geometry and pore pressure head comparisons are shown in this chapter.

6.1. Comparison between Plaxis 2D & 3D

6.1.1. Phase 1 stability analysis

2D analysis are often used due to their relative ease of model construction and rapid computation time by neglecting the normal and horizontal side resisting forces along the sides of the sliding mass. This can lead to a conservative estimate of factor of safety. The result of Plaxis 2D phase 1 stability analysis is shown in figure 6.1 down below.

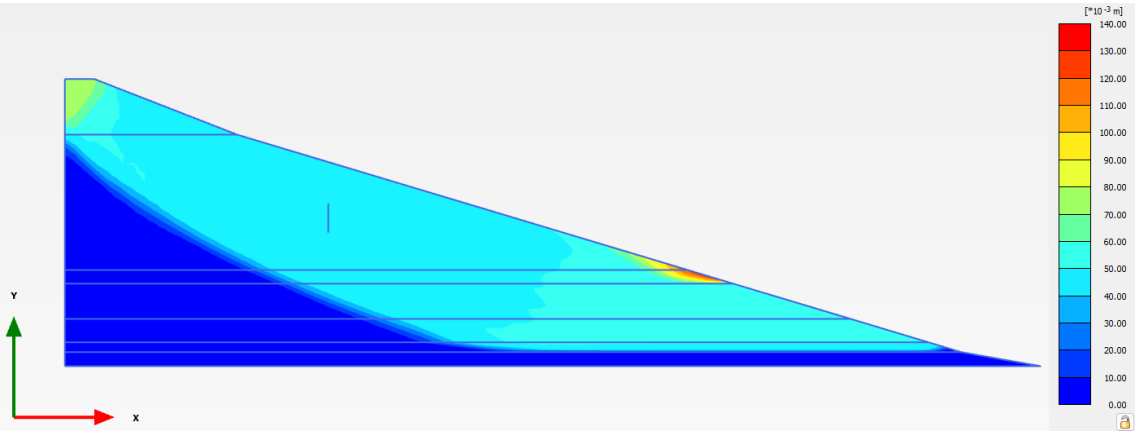

Figure 6.1: 2D stability analysis- Phase 1, FOS= 1.67

From 2D analysis, the obtained factor of safety was 1.67, which is higher compared to 3D factor of safety of 1.538. From figure 6.1, maximum incremental displacement for the 2D analysis was 13.11cm at the depth of -13.81mNAP at the end of the clean sand layer in the geometry. This behaviour is similar to what was observed in the 3D analysis result with displacements in the range of 2 to 5.4cm at the depth of -13.81mNAP to -15.21mNAP. This was an expected behaviour due to the presence of the clay layer from the depth -13.81mNAP to -15.21mNAP. 2D analysis seemed to produce higher displacements when compared to the 3D analysis. In the 2D analysis there seems to a lot of displacements in the range of 4 to 5cm throughout the entire geometry which was not the case in the 3D analysis. This difference in distribution of displacements was expected in a 2D analysis.

6.1.2. Phase 2, pore pressure

Figure 6.2 shows the displacements due to the addition of excess pore pressures. As expected the displacements or the effects of the excess pore pressure is very localised and is only near the vicinity of the well. All of the displacement have seemed to occur in the area beyond the coordinates of the well (27.0, -7.0). The direction of the displacement increments are shown in the figure 6.3. On evaluating the displacement increments, the shape of the failure surface (in formation) is clear.

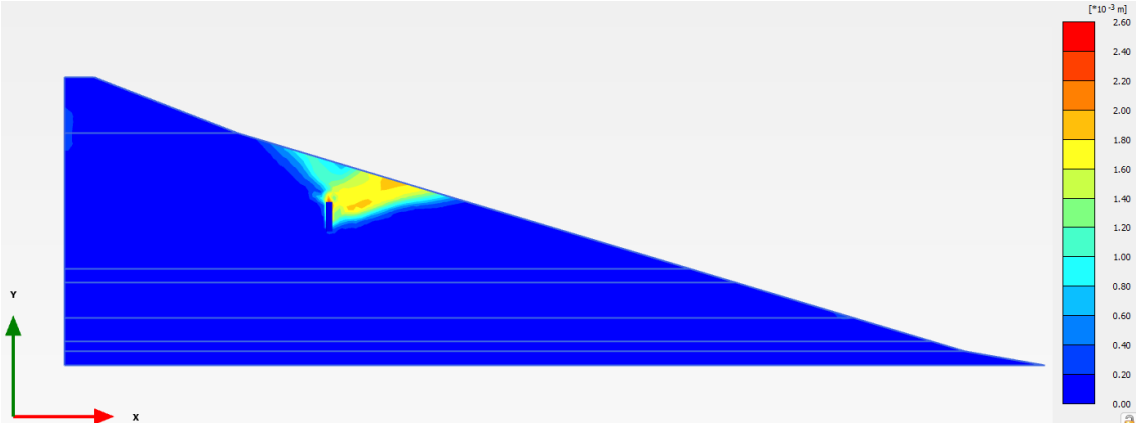

Figure 6.2: Displacements due to the addition of Excess pore pressures, phase 2

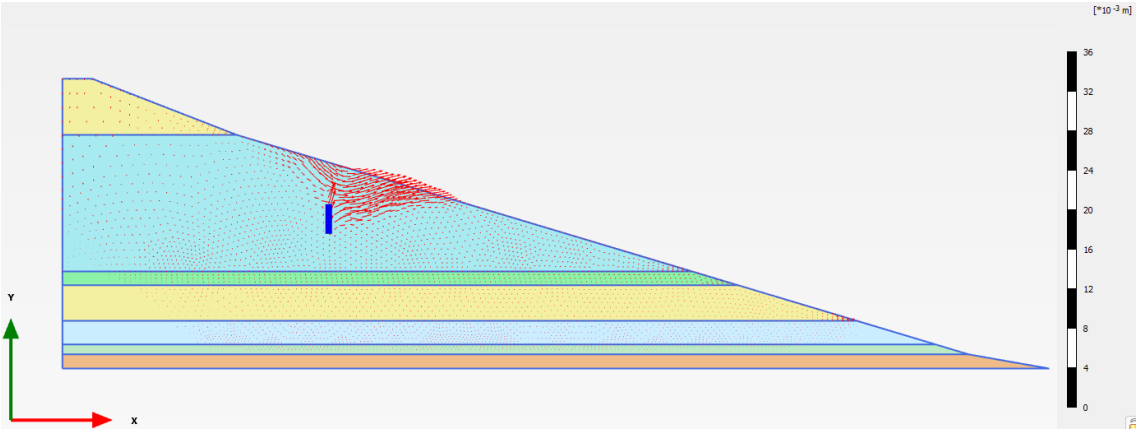

Figure 6.3: Direction of displacement increments

When compared to the direction of displacement increments, while the general shape of the failure surface (in formation) is similar, most of the displacement increments is concentrated near the well in 2D but in 3D most of the increments is concentrated at the crest of the slope with major increments near the well (figure 6.4). Due to this there is a displacement of 0.5mm throughout the width at the crest of the slope (3D). But in general both the analysis in 2D and 3D have displacements in a close by range. The maximum displacement at this phase was observed to be 2.5mm compared to the maximum displacement of 1.75mm from the 3D analysis. The effects of the excess pore pressures observed in the 2D analysis is as expected when compared to the 3D analysis shown in the figure 5.9. From the 3D analysis what was surprising was the high head values at the vicinity of the well, but similar high head values were also seen at the same location in the 2D analysis with the highest attained value of 77m at the location (27.0, -7.750). These higher head values show very low signs of dissipation as the head values keep on increasing without having any substantial reduction for the two minutes of well infiltration. This can be seen in figure 6.5. Considering the formation of excess pore pressures, both 2D and 3D analysis show similar trend of high excess pore pressures around the well and gradually lower from the location of the well but there is more excess pore pressures points towards the back of the geometry in 3D.

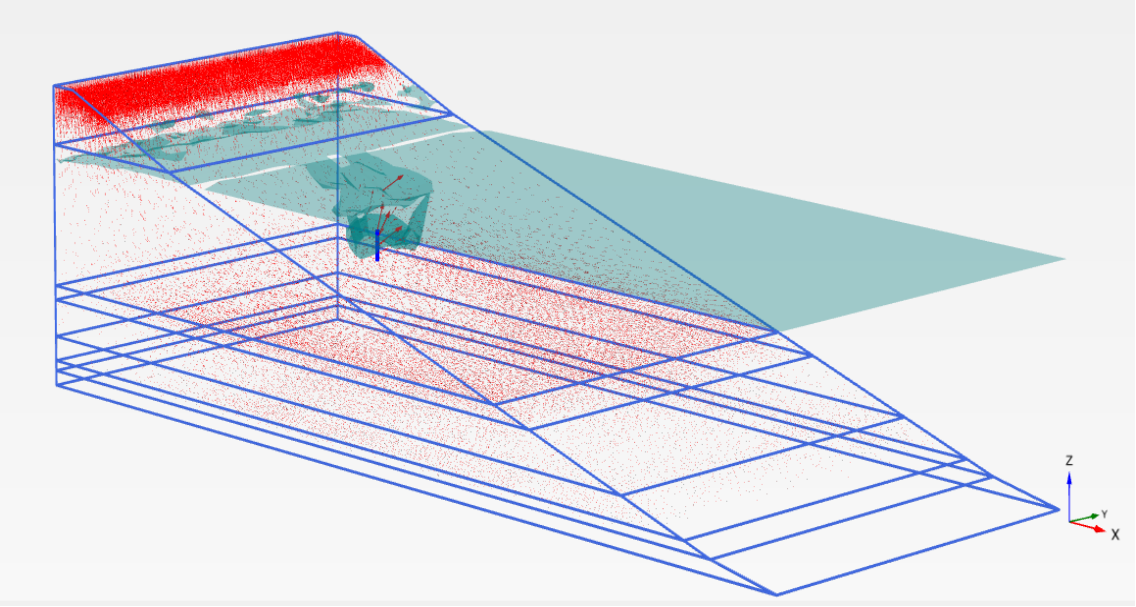

Figure 6.4: Direction of displacement increments-3D

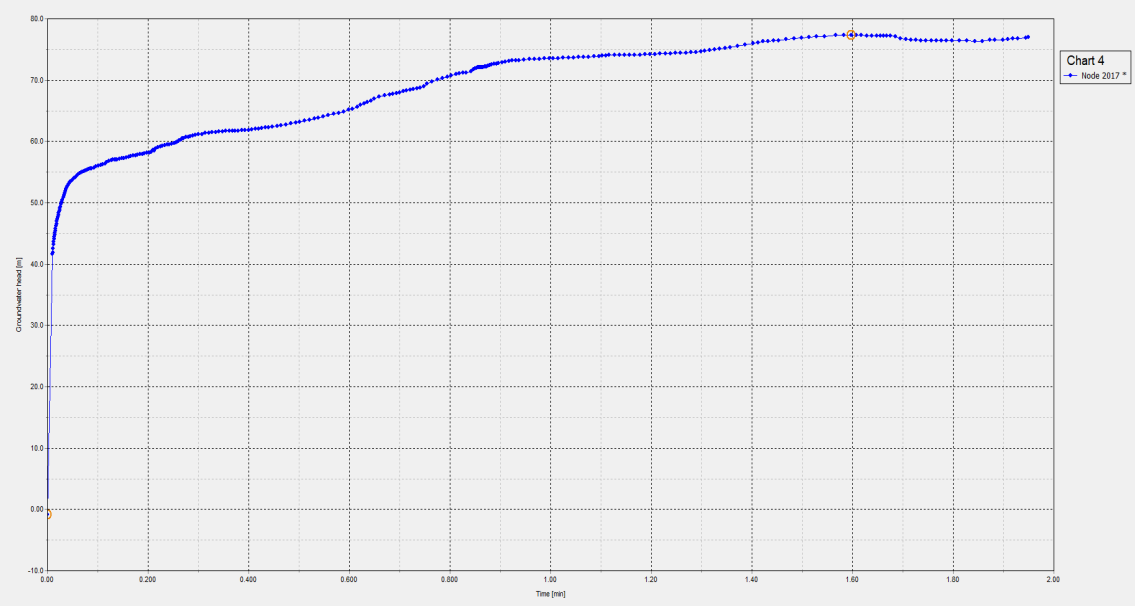

Figure 6.5: Groundwater Head vs time curve for Plaxis 2D

6.1.3. Phase 3 stability analysis

Comparing figure 6.6 and 5.11 the location of displacements observed in this phase was different for 2D analysis. The maximum displacement attained at this phase was as low as 1mm at the location of the well (27.0, -7.0). The failure surface formation and effect of the pore pressures on the slope can be seen in figure 6.7 shown below. This is an unexpected result compared to the phase 3 stability analysis done in Plaxis 3D. In the Plaxis 3D analysis, the excess pore pressure seems to have trapped in the clay layer at -15.21mNAP which caused the displacement of 9.09cm at this depth. The 2D factor of safety was observed to be as low as 0.98. This was quite different from the 3D factor of safety as it was 1.084. The difference in the factor of safety was by 9.5%. Since the 2D analysis is constrained in the direction perpendicular to the analysis plane, which is not the case for the 3D analysis there is a huge difference in the results from all the phases.

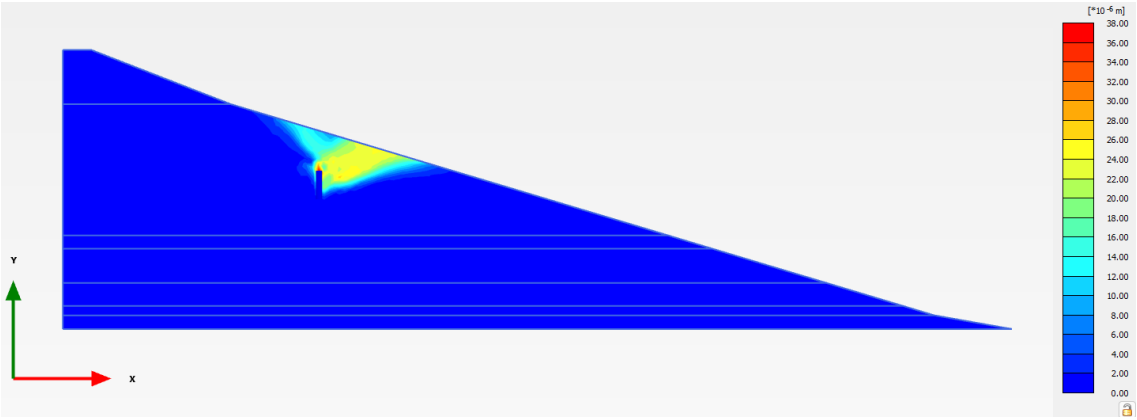

Figure 6.6: 2D stability analysis-Phase 3, FOS=0.98

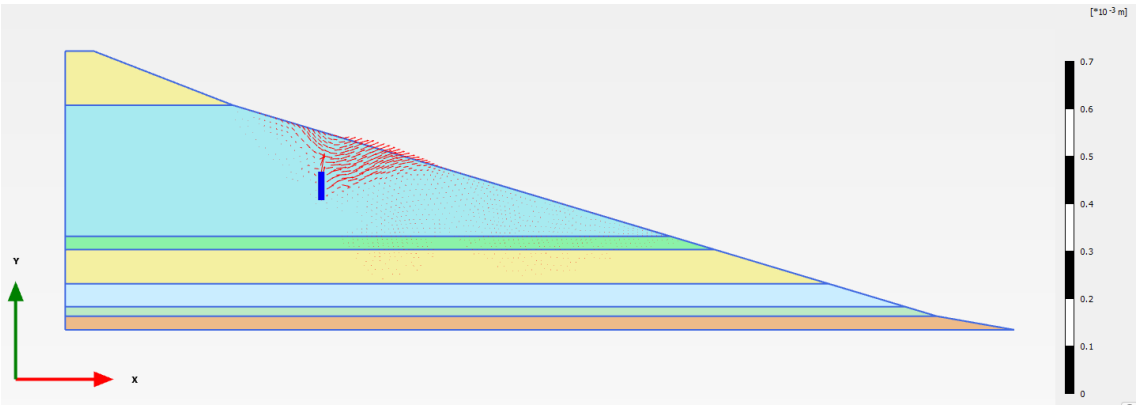

Figure 6.7: Direction of displacement increments-Phase 3 stability analysis

6.2. Effects of excess pore pressures

In an another way to validate the 3D Plaxis model different infiltration values were used. These infiltration values are taken from the table 5.2 in chapter 5, based on the rate of compaction of the soil. Given the use of rate of compaction for the well infiltration volume, higher displacements were expected for phase 2 analysis in the highest compaction rate soil which was 8% out of the three options used. This is because of the 8% compaction rate soil being weaker when compared to the same soil with 2% compaction rate. The effects of adding different pore pressures through the well can be seen in terms of displacements in the soil in phase 2 and the maximum excess pore pressure attained in table 6.1.

Table 6.1: Rate of compaction and its respective effects on displacements and maximum excess pore pressure

Rate of compaction	Volume disp (m^3/m)	Max pore pressures (kPa)	Displacements (mm)
2 %	0.243	957.5	0.53
5 %	0.455	2075	1.20
8 %	0.667	3163	1.75

While the different values of maximum attained excess pore pressure and phase 2 displacements are observed with changing volume displaced, there was very low to no effect reported on the factor of safety of the slopes after the phase 3 stability analysis. In the phase 3 analysis for all the different volume displaced values, the factor of safety stayed in a constant range of 1.080 to 1.084.

Pore Pressure Head

Phase 2 calculation in this whole model is one of the most important analysis as it is supposed to be mimicking on-site conditions during a pile driving. In order to check if the generation of excess pore pressure during the well infiltration phase are somewhat similar to the Calandkanaal case study, the

change of pore pressure head was checked at three distinct locations. In figure 6.8, the increase in pore pressure head is plotted against the total time of infiltration into the model, which is for 2 minutes. The location of the three nodes used around the pile are shown in table 6.2 in the next page.

Table 6.2: Node information used in the figure 6.8

Node name	Location	Radial dist. from the well(d)
41	(27, 20, -7)	0d
3133	(27, 20, -8.50)	0d
59276	(22.32, 19.73, -10.53)	3d

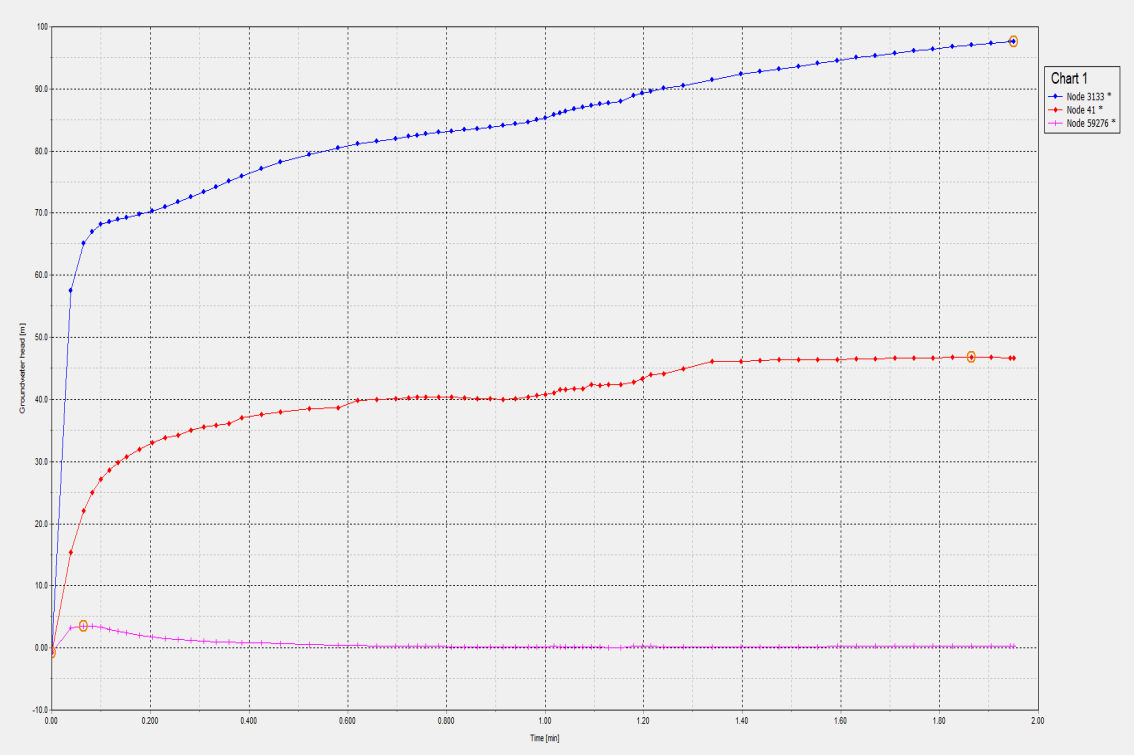

Figure 6.8: Change in pore pressure head in first 2 minutes of pile driving

From the figure 6.8, node 3133 (0d) can be seen attaining the highest head value of 97m at the end of the 2 minutes of the infiltration. Similar trend of pore pressure head can also be seen at the node 41 (0d) with maximum attained head of 46.7m. Higher head values were expected at these two nodes because of their radial distance from the well. In the figure 6.8, a third trend can be seen which is for the node 59276 at a radial distance of 3d from the well, d being the diameter of the pile in the original case study. At this point the maximum attained head value is 3.47m in the beginning of the infiltration, but as the time passes by dissipation can also be seen which leads to a constant head of 0.32m. In an attempt to validate the results from the finite element model, these head values are converted back to r_u values for comparison with the results obtained from the GMP pore pressure model. r_u values

Table 6.3: $r_u$values comparison from FEM and GMP model

Node name	Radial dist. from the source	r_u
Node 59276(FEM)	3d	0.012
Sensor 1 (GMP)	2d	0.005

at these two mentioned nodes, are not expected to be exactly same because of the difference in soil conditions. But since the soil conditions used in the model are of similar type when compared to the site conditions, the r_u values were expected to be in a close range.

6.3. Summary

This chapter discusses the difference and the similarities in the results of both the 2D and 3D Plaxis analysis in a way to validate the analysis done in 3D. While pre pore pressure stability analysis resulted in safe geometry with both the analysis obtaining factor of safety higher than 1.5, the 2D factor of safety was higher than 3D by 8.5%. An unexpected observation was the low factor of safety of 0.98 for the phase 3 analysis in 2D which is lower than the 3D factor of safety by 9.5%. In order to validate the excess pore pressures generated using the GMP pore pressure model, the pore pressures at a distance of 2d (d = diameter of the pile) was compared with and it was observed to be in a close by range to each other. Note that for the GMP pore pressures, dissipation has also been considered as without it it would have been over-estimation of excess pore pressure generation. When considering the figure 6.3, 6.4 and 6.7, there is a major increment of displacement at the top half of the well which tells the location of a major displacement. This could be explained by the high head values that were obtained at the respective locations like seen in figure 6.8.

7

Conclusion

In this work, an attempt is made to understand the stability of a slope during vibratory installation of a pile. The work comprises of understanding field response from the data, model the responses using the analytical and finite element simulation, followed by cross validation in an effort to determine the 3D factor of safety. The GMP pore pressure model (Green & Mitchell 2004) was used to determine the generated excess pore pressures during pile driving activity and its attenuation was determined using Bornitz modelling (Bornitz 1931). To understand the 2D analysis framework used by the Dutch engineering firm (de Nijs 2019) in the calandkanaal project D-Stability analysis was used, while in order to model the whole scenario in 3D, Plaxis 3D was adopted. Finally to validate the 3D model, Plaxis 2D model was used and comparisons were made based on the results provided by both.

How can the existing knowledge on pile driving during vibratory installation be efficiently integrated into a 3D model which can practically estimate the factor of safety of the slope after vibratory installations?

In order to answer the main research question, a couple of sub questions were formed.

What is understood about soil response during vibratory pile driving from the Calandkanaal, Port of Rotterdam?

- Sensors having similar boundary conditions observed different responses during the vibratory driving. Two sensors placed at the same depth (-14mNAP) and equal radial distances (3 meters) from the pile showed difference in particle velocity and frequency during the pile driving. This was because one sensor was recording higher readings than expected based on the prediction per stroke energy (de Nijs 2019). Due to this reason there was also different readings in the computed excess pore pressure for the same location and time interval.

- Observed particle frequency from the accelerometers were in the range of 10-170 Hz, where as the vibratory hammer was driven at its maximum frequency of 38Hz. The frequency of 10-20Hz were because the pile tries to overcome the mobilized friction between soil and the pile shaft resulting a mass of soil layer vibrating at a lower frequency (Kim & Lee 2000). The higher frequency value ranging from 60-170 Hz were observed at very few instances and hence it was considered as noise recorded by the sensors (de Nijs 2019).

- The duration of actual penetration was one-third the duration of total driving duration. While the vibratory hammer was turned on for 35 minutes 25 seconds, the actual time when the pile penetrated into the slope was 10 minutes 33 seconds. At these time intervals when the pile tip was actually moving downward there was rapid generation of excess pore pressures compared to the intervals when the pile tip was not moving. Due to this, there was a step wise trend in the computed excess pore pressure generation with the GMP pore pressure model (Green & Mitchell 2004).

Apart from the observations from the Calandkanaal data set, how could the data set help to understand and simulate similar soil behaviour?

Given the data set was in the form of vibrations amplitude, links were made with strain data (Massarsch 2000) which in return were used to compute the excess pore pressures generated with the use of GMP pore pressure model (Green & Mitchell 2004), (Meijers 2007). For the finite element model, based on the vibration data (accelerations), cone penetration resistance and rate of compaction, displaced volume of water (m^3/min) (de Nijs 2019) was calculated. This certain volume of water was used as a loading parameter in the finite element model to simulate the excess pore pressure generated during the first 2 minutes of pile driving.

What was the range of the area around the pile that was affected by the vibratory pile driving?

Affected or degraded area around pile means liquefied zone around pile due to the generation of excess pore pressure. Liquefied zone means the ratio of excess pore pressure to initial effective stress $r_u = 1$. Using an empirical relation between vibration amplitude and distance (Kim & Lee 2000), pore pressure attenuation was determined considering both generation and dissipation of excess pore pressures, the degraded zone was found to be 0.85m from the skin of the pile which can be seen in figure 4.18.

What are the limitations of the current approach for the determination of the factor of safety in 3D?

While the approach used in this thesis determines the factor of safety of a slope subjected to pile driving in 3D, there are a certain number of limitations in it which requires more attention for future research work:

- For the determination of the PEC (Psuedo energy calibration) factor, the empirical formula used is dependent on relative density of the soil, which again cannot be used for a slope consisting of large clay layers. Relative density is a definition rather than an inherent property of the soil.
- Based on the TRILDENS3 numerical model, damping ratio is determined as a function of strain. For strain less than 10^{-6} damping ratio was determined to be non zero value contradicting to figure 2.6 (Meijers 2007).
- Due to the lack of a pore pressure data from the port of Rotterdam data set there is no way of validating the GMP model (Green & Mitchell 2004) computed excess pore pressures. So these computed excess pore pressure data are approximated values to what could have been actual case study pore pressure values.
- In order to reduce the calculation time for the finite element model, only first 2 minutes of actual pile driving is simulated in terms of pore pressure loading, so it would be interesting to see the effects of simulating the full 10 minutes 33 seconds of pile driving and pore pressure generation on the 3D factor of safety.
- For the 2nd phase of the finite element model, a coupled flow-deformation analysis was used which is a time dependent analysis. To reduce research time on literature review, not much attention was paid to time dependent soil models for this phase. It would be interesting to observe the effects of different soil models for future work.

Appendix-A

This chapter includes the information which was used to determine the soil layer and their respective properties. For soil properties the table 2b from the NEN9997 and for soil layer from different CPTs and borehole logs are presented here. Along with that, excess pore pressures distribution during Plaxis 2D and 3D are also shown here. These figures gives a clear idea about the zone of influence of the pore pressures in the geometry. Here from both the figures it can be clearly the general distribution of the excess pore pressures in phase-2 of the calculation is fairly similar for both 2D and 3D with clear differences in the range of excess pore pressures. In the 2D analysis the range seems to be much higher than the 3D analysis which was unexpected.

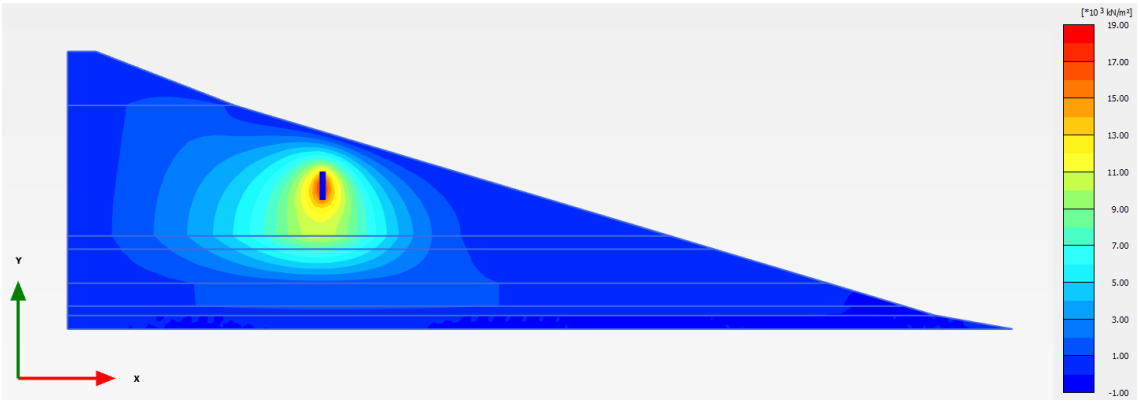

Figure 1: Excess pore pressure distribution in Plaxis 2D

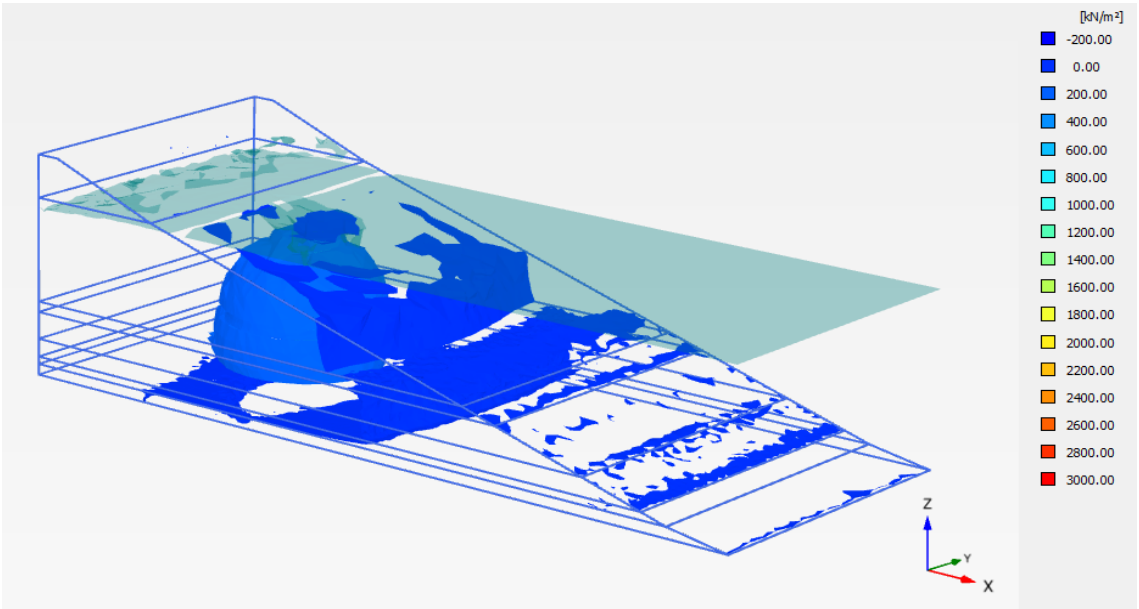

Figure 2: Excess pore pressure distribution in Plaxis 2D

type of soil		characteristic mean value of the soil parameters											
name	**admixture**	**consistency** [1]	**γ** [2] **[kN/m^3]**	**γ_{sat} [kN/m^3]**	**q_c** [3] [6] **[MPa]**	**C'_p** [6]	**C'_s**	**C_c** [6]	**C_a** [5]	**C_{sw}** [6]	**E_{100}** [6] [7] **[MPa]**	**ϕ'** [6] **[°]**	**c' [kPa]**	**f_{undr} / c_u [kPa]**
Gravel	little silty	loose medium dense	17 18 19 or 20	19 20 21 or 22	15 25 30	500 1,000 1,200 or 1,400	– – –	0.008 0.004 0.003 or 0.002	0 0 0	0.003 0.002 0.001 or 0	75 125 150 or 200	32.5 35 37.5 or 40	–	–
	very silty	loose medium dense	18 19 20 or 21	20 21 22 or 22.5	10 15 25	400 600 1,000 or 1,500	– – –	0.009 0.006 0.003 or 0.002	0 0 0	0.003 0.002 0.001 or 0	50 75 125 or 150	30 32.5 35 or 40	–	–
Sand	clean	loose medium dense	17 18 19 or 20	19 20 21 or 22	5 15 25	200 600 1,000 or 1,500	– – –	0.021 0.006 0.003 or 0.002	0 0 0	0.007 0.003 0.001 or 0	25 75 125 or 150	30 32.5 35 or 40	–	–
	little silty/clayey very silty/clayey		18 or 19 18 or 19	20 or 21 20 or 21	12 8	450 or 650 200 or 400	– –	0.008 or 0.005 0.019 or 0.009	0 0	0.003 or 0.001 0.006 or 0.001	25 or 35 20 or 30	27 or 32.5 25 or 30	–	–
Silt [4]	little sandy	soft medium stiff	19 20 21 or 22	19 20 21 or 22	1 2 3	25 45 70 or 100	650 1,300 1,900 or 2,500	0.168 0.084 0.049 or 0.030	0.004 0.002 0.001	0.056 0.028 0.017 or 0.005	2 5 10 or 20	27.5 or 30 27.5 or 32.5 27.5 or 35	0 2 5 or 7.5	50 100 200 or 300
	very sandy		19 or 20	19 or 20	2	45 or 70	1,300 or 2,000	0.092 or 0.055	0.002	0.031 or 0.005	5 or 10	27.5 or 35	0 or 2	50 or 100
Clay	clean	soft medium stiff	14 17 19 or 20	14 17 19 or 20	0.5 1.0 2.0	7 15 25 or 30	80 160 320 or 500	1.357 0.362 0.168 or 0.126	0.013 0.006 0.004	0.452 0.121 0.056 or 0.042	1 2 4 or 10	17.5 17.5 17.5 or 25	0 10 25 or 30	25 50 100 or 200
	little sandy	soft medium stiff	15 18 20 or 21	15 18 20 or 21	0.7 1.5 2.5	10 20 30 or 50	110 240 400 or 600	0.759 0.237 0.126 or 0.069	0.009 0.005 0.003	0.253 0.079 0.042 or 0.014	1.5 3 5 or 10	22.5 22.5 22.5 or 27.5	0 10 25 or 30	40 80 120 or 170
	very sandy		18 or 20	18 or 20	1.0	25 or 140	320 or 1,680	0.190 or 0.027	0.004	0.063 or 0.025	2 or 5	27.5 or 32.5	0 or 2	0 or 10
	organic	soft medium	13 15 or 16	13 15 or 16	0.2 0.5	7.5 10 or 15	30 40 or 60	1.690 0.760 or 0.420	0.015 0.012	0.550 0.250 or 0.140	0.5 1.0 or 2.0	15 15	0 or 2 0 or 2	10 25 or 30
Peat	not preloaded	soft	10 or 12	10 or 12	0.1	5 or 7.5	20 or 30	7.590 or 1.810	0.023	2.530 or 0.600	0.2 or 0.5	15	2 or 5	10 or 20
	medium preloaded	medium	12 or 13	12 or 13	0.2	7.5 or 10	30 or 40	1.810 or 0.900	0.016	0.600 or 0.300	0.5 or 1.0	15	5 or 10	20 or 30
Variation coefficient			0.05		–	0.25						0.10	0.20	

BRO-ID: CPT000000132250
Aangeleverde coördinaten: 71494.520, 440399.970 (urn:ogc:def:crs:EPSG::28992)

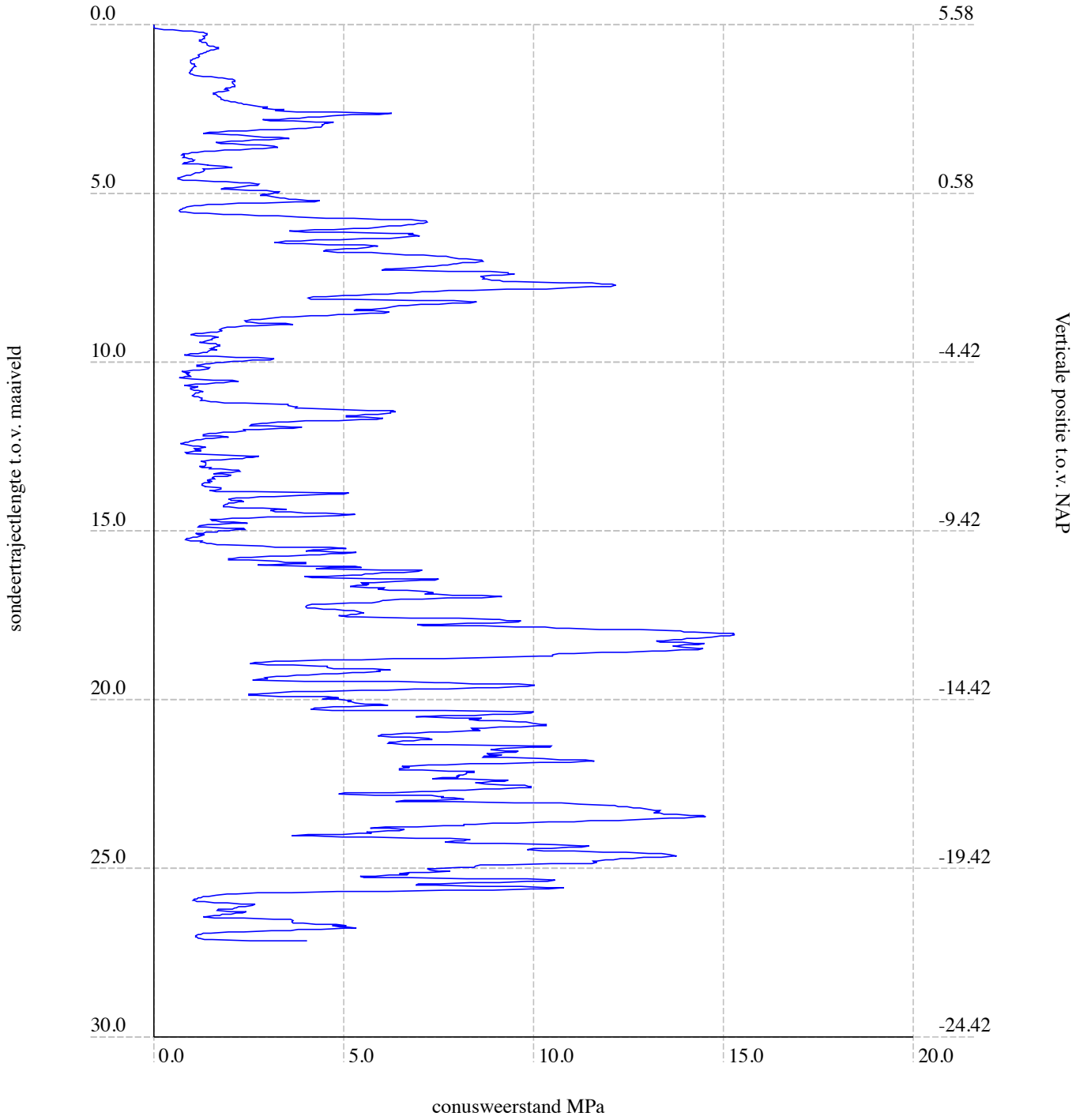

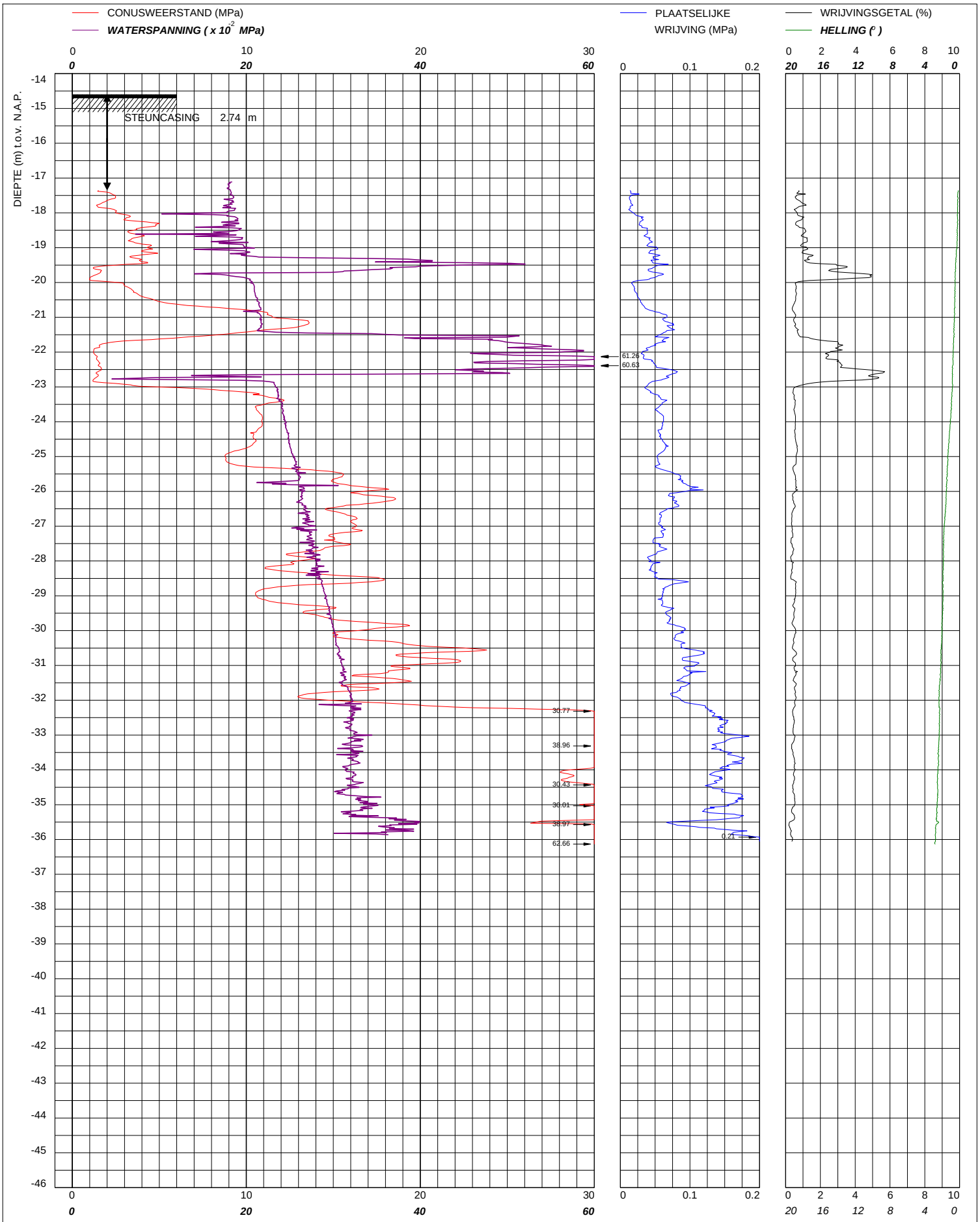

© copyright
Multiconsult
Multiconsult
Contactweg 60
1014 BW AMSTERDAM
Telefoon (020) 410 85 43
Email info@multiconsult.nl

Sondering TE2 volgens NEN-EN-22476-1 klasse 3
Conus: 12351, Ac: 1.500 mm2 Filterpositie U2

Fugro GeoServices B.V.

Calandkanaal te Rotterdam

Water diepte	14.65 m	X	71309	Opdrachtnummer :
Bodem	-14.6 m N.A.P.	Y	440476	003504
Uitvoeringsdatum		15-4-2016		Locatiecode :
Printdatum		15-4-2016		S-40

Boring: B-40

Datum: 20-04-2016
X: 71307,70
Y 440478,80

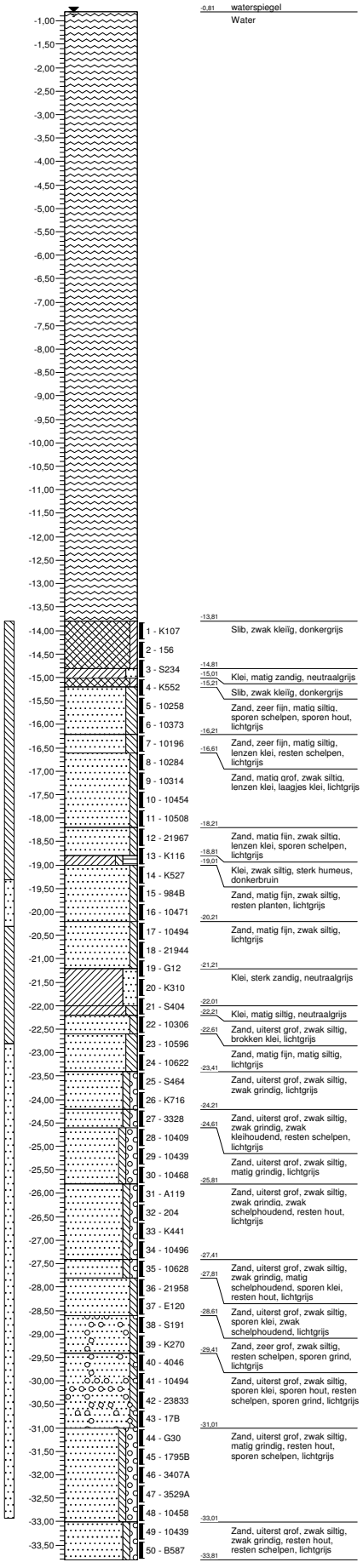

BAM Infraconsult bv
Contactweg 60
1014 BW AMSTERDAM
Telefoon (020) 410 85 43
Email info@baminfraconsult.nl

Projectnaam:	Calandkanaal te Rotterdam	Boormeester:	M. v/d Plas
Opdrachtgever:	Fugro GeoServices B.V.	Projectleider:	K. Geyteman
Projectcode:	003504	Pagina:	1 / 1

Bibliography

A B Arun Kumar (2020), 'Evolution of the pore pressure due to vibratory installation of sheet piles in sand'.

Barkan, D. D. (1962), *Dynamics of bases and foundations*, McGraw-Hill Companies.

Bornitz, G. (1931), *Über die Ausbreitung der von Großkolbenmaschinen erzeugten Bodenschwingungen in die Tiefe by Dr.-Ing. G. Bornitz (auth.) (z-lib.org).pdf*, 1 edn, Springer Verlag Berlin Heidelberg.
URL: *https://nl1lib.org/book/2106609/499cb8*

Brennan, A. & Madabhushi, S. (2011), 'Measurement of coefficient of consolidation during reconsolidation of liquefied sand', *Geotechnical Testing Journal* **34**(2), 139–146.

Byrne, M. (1991), 'A cyclic shear-volume coupling and pore pressure model for sand', *Second international conference on recent advances in geotechnical engineering and soil dynamics* pp. 47–55.

Chian, S. (2015), 'Empirical Excess Pore Pressure Dissipation Model for Liquifiable Sands', pp. 536–537.

de Nijs, I. M. (2019), 'STABILITEIT WATERKERING TIJDENS INTRILLEN BUISPALEN'.

Deckner, F. (2013), Licentiate Thesis, Phd, KTH, Royal Institute of Technology, Stockholm.
URL: *https://www.bth.se/com/aje.nsf/bilagor/Lic Åse Jevinger_1_pdf/$file/Lic Åse Jevinger_1.pdf*

Deresiewicz, H. (1958), Mechanics of granular matter**this study was supported by the office of naval research under contract nonr-266(09) with columbia university., Vol. 5 of *Advances in Applied Mechanics*, Elsevier, pp. 233 – 306.
URL: *http://www.sciencedirect.com/science/article/pii/S0065215608700218*

Engineering, F. (1987), 'A SIMPLIFIED DRAINED ANALYSIS FOR WAVE-INDUCED T-', **26**(3), 57–68.

Florin, V. & Ivanov, P. (1961), 'Liquefaction of Saturated Sandy Soils', *International Society for Soil Mechanics and Geotechnical Engineering* pp. 107–111.

Gitirana, Jr., G., Santos, M. A. & Fredlund, M. D. (2008), 'Three-Dimensional Slope Stability Model Using Finite Element Stress Analysis', **40971**(July 2020), 191–198.

Green, R. A. & Mitchell, J. K. (2004), Energy-based evaluation and remediation of liquefiable soils, PhD thesis, Virginia Polytechnic Institute and State University.

Grizi, A., Athanasopoulos-Zekkos, A. & Woods, R. D. (2018), 'Pile Driving Vibration Attenuation Relationships: Overview and Calibration Using Field Measurements', pp. 435–444.

Hammer, V. & Moment, V. (2013), 'Specification Sheet PVE 40VM Vibro Hammer with Variable Moment Specification Sheet PVE 40VM Vibro Hammer with Variable Moment', pp. 1–2.

Holmberg, R, A. P. W., Bennerhult, D., Forssblad, L., Gereben, L., Hellman, L., Olsson, K., Rundqvist, K., Sjoeberg, C., Sjoekvist & Wallmark, G. (1984), 'VIBRATIONS GENERATED BY TRAFFIC AND BUILDING CONSTRUCTION ACTIVITIES', *VTT Technical Research Centre of Finland* p. 36.

Hwang, J.-H., Liang, N. & Chen, C.-H. (2001), 'Ground Response during Pile Driving', *Journal of Geotechnical and Geoenvironmental Engineering* **127**(11), 939–949.

Ibsen, L. B. (1994), 'The stable state in cyclic triaxial testing on sand', **13**, 63–72.

Kim, D. S. & Lee, J. S. (2000), 'Propagation and attenuation characteristics of various ground vibrations', *Soil Dynamics and Earthquake Engineering* **19**(2), 115–126.

Kim, S.-R., Hwang, J.-I., Ko, H.-Y. & Kim, M.-M. (2009), 'Development of Dissipation Model of Excess Pore Pressure in Liquefied Sandy Ground', *Journal of Geotechnical and Geoenvironmental Engineering* **135**(4), 544–554.

Lamens, P. (2017), 'Pile installation in submerged sandy slopes Assessing liquefaction-induced instability'.

L.Kramer, S. (1996), *Geotechnical Earthquake Engineering*.

LO, K. & STERMAC, A. (1965), 'Induced Pore Pressures during Pile-Driving Operations', *INTERNATIONAL SOCIETY FOR SOIL MECHANICS AND GEOTECHNICAL ENGINEERING* pp. 285–289.

Martin, G., Finn, W. & Seed, H. (1975), 'Fundamentals of liquefaction under cyclic loading', *Journal of Geotechnical and Geoenvironmental Engineering* **101**, 423–438.

Massarsch, K. (2000), 'Settlements and damage caused by construction-induced vibrations', *Proceedings of international workshop wave* (December), 299–315.

Massarsch, K. R. (1993), Static and dynamic soil displacements caused by pile driving.

Massarsch, K. R. (2004), 'Vibrations Caused by Pile Driving', *The Magazine of the Deep Foundations Institute* pp. 2–7.

Massarsch, K Rainer; Fellenius, B. (2010), Ground vibrations induced by impact pile driving . Ground Vibrations Induced by Impact Pile Driving, *in* 'The Sixth International Conference on Case Histories in Geotechnical Engineering', number August, p. 38.

Meijers, P. (2007), Settlement during vibratory sheet piling, PhD thesis, Technische Universiteit Delft.

Pan, Q., Xu, J. & Dias, D. (2017), 'Three-Dimensional Stability of a Slope Subjected to Seepage Forces', *International Journal of Geomechanics* **17**(8), 04017035.

Rahman, M., Booker, J. R. & Seed, H. B. (1977), 'Pore pressure development under offshore gravity structures', *Journal of the Geotechnical Engineering Division* **103**(12), 1419–1436.

Ramli Mohamad, R. D. (1987), 'Settlement of cohesionless soils due to piling vibrations'.
URL: *http://seags.ait.asia/publications/9th-SEAC-Thailand-1987-v2.pdf*

Randolph, M. F. & Wroth, C. P. (1979), 'An analytical solution for the consolidation around a driven pile', *International Journal for Numerical and Analytical Methods in Geomechanics* **3**(3), 217–229.

Rao, P., Rao, P., Wu, J. & Mo, Z. (2020), '3D Limit Analysis of the Transient Stability of Slope during Pile Driving in Nonhomogeneous and Anisotropic Soil', *Advances in Civil Engineering* **2020**.

Rao, P., Zhao, L., Chen, Q. & Nimbalkar, S. (2019), 'Three-Dimensional Slope Stability Analysis Incorporating Coupled Effects of Pile Reinforcement and Reservoir Drawdown', *International Journal of Geomechanics* **19**(4), 06019002.

Rausche, F. (2003), 'Modeling of vibratory pile driving ', *GRL Engineers, Inc* .

Reinius, E. (1955), 'The Stability of the Slopes of Earth Dams', *Géotechnique* **5**(2), 181–189.

Richart, F. E., Hall, J. R. & Woods, R. D. (1970), *Vibrations of soils and foundations / F.E. Richart, Jr., R.D. Woods, J.R. Hall, Jr*, Prentice-Hall.

Robbin, W. (2020), 'Ground response during offshore pile driving in a sandy slope'.

Rodger, A. A. & Little John, G. S. (1980), 'A Study of Vibratory Driving in Granular Soils', *Geotechnique* **30**(3), 269–293.

Scott, R. F. (1986), 'Soil properties from centrifuge liquefaction tests', *Mechanics of Materials* **5**(2), 199–206.

Seed, H. B. (1988), 'Design problems in soil liquefaction >', **113**(8), 827–845.

Seed, H. B., Wong, R. T., Idriss, I. M. & Tokimatsu, K. (1986), 'Moduli and damping factors for dynamic analyses of cohesionless soils', *Journal of Geotechnical Engineering* **112**(11), 1016–1032. **URL:** *https://ascelibrary.org/doi/pdf/10.1061/(ASCE)0733-9410(1986)112:11(1016)*

Seed.H, B. (1979), 'Soil Liquefaction and Cyclic Mobility Evaluation for Level Ground during Earthquakes', **105**, 201–255.

Silver, M. L. & Seed, H. (1971), 'Volume changes in sands during cyclic loading', *Journal of the Soil Mechanics and Foundations Division* **97**, 1171–1182.

Spencer, E. (1967), '"Embankments Assuming Parallel Inter-Slice Forces"', *Géotechnique* **17**(1), 11–26.

Terzaghi, K. (1943), 'Theoretical Soil Mechanics', *Theoretical Soil Mechanics* .

Viking, K. & Bodare, A. (1999), *Laboratory studies of dynamic shaft resistance of a vibro-driven model pile in granular soil by varying the relative density*, Vol. 2, p. 863–869.

V.N.S., M. (2002), *Geotechnical Engineering : Principles and Practices of Soil Mechanics and Foundation Engineering.*, number Vol. 10 *in* 'Civil and Environmental Engineering', CRC Press.

Wales, N. S., Green, R. a. & Mitchell, J. K. (2000), 'An Energy-Based Excess Pore Pressure Generation Model for Cohesionless Soils', *Proceeding of the John Booker Memorial Symposium* (February), 1–9.

Warrington, D. (1989), 'Vibratory and Impact-Vibration pile driving equipment'.

Whenham, V. & Holeyman, A. (2012), 'Load Transfers During Vibratory Driving', (October 2012).

Yoshimi.Y, T. & N, O. (1994), 'In situ liquefaction resistance of clean sands over a wide density range', **44**, 479–494.

Youd, T. (1977), Packing changes and liquefaction susceptibility, Vol. 103, No. GT8 of *Journal of the Geotechnical Engineering Division, Proceedings of the American Society of Civil Engineers*, pp. 918–922.